UNIVERSITY OF SAN LUIS POTOSI

PHYSICS INSTITUTE

P H D T H E S I S

to obtain the title of

PhD in Science (Physics)

Defended by

Alfredo Martín Castañeda Hernández

Search for TeV-scale Gravity Signatures in Final states with Leptons and Jets with the ATLAS detector at $\sqrt{s}$ =7 TeV

Thesis Advisor: Antonio Morelos Pineda

defended on June 19, 2012

Committee:

Antonio Morelos Pineda	-	IF-UASLP
Ruben Flores Mendieta	-	IF-UASLP
Mariana Kirchbach	-	IF-UASLP
Ricardo Guirado Lopez	-	IF-UASLP
Heriberto Castilla Valdez	-	CINVESTAV

Acknowledgements

I would like to thank a number of people who are an important part of the successful elaboration of this study, first of all to my two Advisors: Prof. Sau Lan Wu and Prof. Antonio Morelos Pineda. Thanks to Prof. Wu for giving me the opportunity to work in her group and also the invaluable experience to be part of an international collaboration, to Dr. Morelos for his support and advices during the more than four years this project took. Also thanks to the SUSY and Exotics working groups in ATLAS for the extensive discussions and advices always needed in order to produce good quality results and of course to the whole ATLAS collaboration for building such an incredible machine. I would like to express my gratitude to Tapas Sarangi who was a postdoc for the University of Wisconsin at that time from whom I have learned a lot in particle physics analysis and also for being such a nice person. Finally I would like to thank my family for being always with me and showing support in all the possible ways. I would like to dedicate this Thesis to my love Cinndy who was always with me sharing a lot of experiences over the past four years. I take the opportunity to thank CONACyT, IF-UASLP and the University of Wisconsin for providing the funding and conditions needed during my PhD.

Search for TeV-scale Gravity Signatures in Final states with Leptons and Jets with the ATLAS detector at $\sqrt{s}$ =7 TeV

Abstract: The analysis described in this thesis is a search for strong gravity effects in proton-proton collisions at the LHC, with a center of mass energy of 7 TeV and 1.04 fb^{-1} of integrated luminosity, it is motivated by the Hierarchy problem which questions the immense order of magnitude difference between the Electroweak ($\sim 10^3$ GeV) and the Planck ($\sim 10^{19}$ GeV) scales. Possible solutions to this problem have emerged in recent years with models proposing scenarios of extra-dimensions, in such scenarios the Planck scale is of the order of the electroweak interactions ($\sim$TeV) and this allows the production of non-perturbative gravitational states such as Black Holes with an energy of order of magnitude accesible at the LHC. From the different final states produced after the Black Hole evaporation, the Lepton plus Jets final state was chosen because it reduces considerably the background coming from QCD processes and keeps a reasonable efficiency for Black Hole signal events.
Chapter 1 motivates the search, introducing the ADD model which proposes an scenario of **(4+n)** dimensions where **n** is the number of extra-dimensions, a brief description of cosmological Black Holes is given, and the production of Black Holes at the LHC is discussed
Chapter 2 describes the experimental setup, starting with the LHC in general, followed by a description of the principal components of the ATLAS detector, the Trigger system is described in **Chapter 3**, the algorithms for reconstruction of the observed particles (e, μ and hadronic jets) are described in **Chapter 4**, the Monte Carlo samples used to describe signal and backgrounds along the setup for generation are discussed in **Chapter 5**, the systematics considered are listed on **Chapter 6**, the event selection criteria is presented in **Chapter 7**, **Chapter 8** gives an extensive discussion about the methods to estimate the Standard Model backgrounds in the signal region, **Chapter 9** presents the background studies in the search of SUSY signals in a di-lepton final state and compares the background methods used with those from the Black Hole analysis, finally in **Chapter 10** the final results with the corresponding interpretations are given, following the agreement of the observed events with the expected background coming from the Standard Model, limits are set on the fiducial cross section of final states with a prompt lepton in association with jets and in benchmark models of Black Hole and String Ball production.

Contents

1 Introduction **1**
- 1.1 Standard Model . . . 1
  - 1.1.1 Quarks . . . 2
  - 1.1.2 Leptons . . . 2
  - 1.1.3 Forces and Interactions . . . 3
  - 1.1.4 Unification . . . 4
- 1.2 Beyond the Standard Model . . . 5
- 1.3 The Hierarchy problem and a proposed solution in extra-dimensions . . . 6
- 1.4 Black Holes: Stellar and microscopic . . . 7
  - 1.4.1 Stellar Black Holes . . . 8
  - 1.4.2 Microscopic Black Holes: production at the LHC . . . 10

2 LHC and the ATLAS detector **17**
- 2.1 The Large Hadron Collider (LHC) . . . 17
- 2.2 The ATLAS detector . . . 19
  - 2.2.1 Inner Detector . . . 19
  - 2.2.2 Calorimetry . . . 21
  - 2.2.3 Muon spectrometer . . . 21

3 Trigger and Data Acquisition **23**
- 3.1 Level 1 (LVL1) . . . 24
- 3.2 Level 2 (LVL2) . . . 24
- 3.3 Level 3: Event Filter (EF) . . . 24
- 3.4 Data collected . . . 25

4 Particle Identification and Reconstruction **27**
- 4.1 Electron Reconstruction and Identification . . . 27
  - 4.1.1 Reconstruction algorithms . . . 27
  - 4.1.2 Electron Energy Calibration . . . 28
- 4.2 Muon Reconstruction and Identification . . . 29
  - 4.2.1 Muon reconstruction algorithms . . . 31
  - 4.2.2 Muon momentum resolution . . . 32
  - 4.2.3 Muon Momentum resolution at high-p_T . . . 35
- 4.3 Reconstruction and Identification of Jets . . . 35
  - 4.3.1 Jet reconstruction algorithms . . . 35
  - 4.3.2 Jet Energy Scale . . . 35
- 4.4 Missing Transverse Energy . . . 38

5 Monte Carlo simulation **41**
5.1 Background Samples . . . 41
5.1.1 QCD Samples . . . 41
5.1.2 W/Z+Jets Samples . . . 41
5.1.3 $t\bar{t}$ Samples . . . 42
5.1.4 Single Top Samples . . . 42
5.1.5 Di-Boson Samples . . . 42
5.2 Signal Samples . . . 43
5.2.1 CHARYBDIS Samples . . . 43
5.2.2 BLACKMAX Samples . . . 44

6 Systematics **45**
6.1 Jet Energy Scale/Resolution . . . 45
6.1.1 Jet Energy Scale (JES) Uncertainty . . . 45
6.1.2 Jet Energy Resolution (JER) . . . 48
6.2 Lepton Energy Scale/Resolution . . . 48
6.3 Monte Carlo Generator . . . 48
6.4 Initial and Final State Radiation . . . 48
6.5 Total Uncertainty . . . 49

7 Particle and Event Selection **51**
7.1 Object (Particle) selection . . . 51
7.1.1 Electron selection . . . 51
7.1.2 Muon selection . . . 52
7.1.3 Jet selection . . . 52
7.1.4 Overlap removal . . . 52
7.2 Event Selection . . . 52
7.3 $\sum p_T$ variable . . . 54
7.4 Control and Signal region . . . 54
7.5 Observed and expected events for $\int Ldt = 1.04 fb^{-1}$ . . . 55

8 Background Estimation **63**
8.1 QCD (multi-jets) background . . . 63
8.2 $Z + jets$ background . . . 65
8.3 Combined $W + jets$ and $t\bar{t}$ background . . . 78

9 Background Estimation in SUSY di-lepton searches **89**
9.1 Two lepton event production in SUSY cascade decay . . . 89
9.2 Background Topology . . . 90
9.3 Background estimation in the OS channel . . . 90
9.3.1 $t\bar{t}$ background . . . 90
9.3.2 $Z + jets$ background . . . 91

9.3.3 Dibosons and single top . . . 91
9.4 Background estimation in the SS channel . . . 91
9.5 Systematics . . . 92

10 Results and Interpretations **95**
10.1 Event yield and distributions . . . 95
10.2 Model Independent limits . . . 96
10.3 Limits for benchmark models . . . 98

11 conclusions **105**

A Monte Carlo Datasets **107**
A.1 Background Monte Carlo Datasets . . . 107
A.2 Signal Monte Carlo Datasets . . . 113

B The Atlas framework Athena **115**
B.1 Integration of external generators in Athena . . . 116

C Distributions After Pre-selection **119**

D Loose Jet cleaning **125**

E QCD Estimation in the Muon Channel (ABCD Method) **127**

F Statistical significance and the *p-value* **129**

G The CLs Method for limit setting **133**

H ISR/FSR $t\bar{t}$ Variation and Effect on Combined W + *jets*/$t\bar{t}$ Estimation **137**

I Individual PDF Uncertainties for W+jets/$t\bar{t}$ Estimate **141**

J Black Hole candidate event **143**

K Distributions with $\sum p_T > 700$ GeV After Normalization from Control Regions **145**

L Comparison between Lepton plus Jets and Same-sign di-muon Black Hole analysis **149**

M Glossary **153**

Bibliography **155**

List of Figures

1.1 Particles constituents of the Standard Model (six leptons, six quarks and the gauge bosons) along with some of their properties like mass, charge and spin. 1
1.2 Comparison of a White Dwarf, a Neutron Star and the Event Horizon of a Black Hole with the size of our sun. 8
1.3 Graphical representation of two partons colliding with an impact parameter b less than the higher dimensional Schwarzchild radius. 11
1.4 a) Parton-level production cross section, b) differential cross section $d\sigma/dM_B$ at the LHC, c) Hawking temperature, and d) average decay multiplicity for a Schwarzchild Black Hole. The number of extra spacial dimensions n=4 is used for a)-c). The dependence of the cross section and Hawking temperature on n is weak and would be hardly noticeable on the logarithmic scale. The M_P in the plots correspond to the higher dimensional Planck scale $M_{Pl(4+n)}$ mentioned in this section 13
1.5 Number of MBHs produced at the LHC in the electron or photon decay channels, with 100 fb^{-1} of integrated luminosity, as a function of the BH mass. The shaded regions correspond to the variation in the number of events for n between 2 and 7. The dashed line shows total SM background (from inclusive Z(ee) and direct photon production). The dotted line corresponds to the Z(ee)+X background alone. The M_P in the plot correspond to the higher dimensional Planck scale $M_{Pl(4+n)}$ mentioned in this section. 14

2.1 Schematic view of the Large Hadron Collider (LHC) experiment, showing the four most important particle detection points around the tunnel. 17
2.2 Internal view of the LHC tunnel 19
2.3 Schematic view of the ATLAS detector and its sub-detector components 20
2.4 Inner detector components 20
2.5 Electromagnetic and Hadronic calorimeters and their components 21
2.6 Moun spectrometer and its components 22

3.1 Overview of the ATLAS trigger system 23

3.2 Integrated luminosity recorded during the first half of 2011, corresponding to $\int Ldt \sim 1fb^{-1}$. 25

4.1 Di-electron invariant mass for $Z \rightarrow ee$ Monte Carlo sample. . . 30
4.2 Distribution of α_{fit} for data 30
4.3 Resolution curve form the fitted parameter values of the MS in collision data and simulation as a function of the muon p_T, for the different $|\eta|$ regions of the detector. The solid blue line shows determinations based on data and is continued as dashed line or the extrapolation to p_T ranges not accessible. The shaded band represents the sum in quadrature of the statistical and systematic uncertainties. For the case of the barrel, a comparison with the curve obtained from the fitted parameters from cosmic ray data is overlaided for comparison. 33
4.4 Resolution curve on the curvature, $\sigma(1/p_T)$, from the fitted parameter values of the ID in collision data and simulation as a function of the muon p_T for different $|\eta|$ regions. The solid blue line shows measurements on data and is continued as dashed line for the extrapolation to p_T ranges not accessible in this analysis. The shaded band represents the sum in quadrature of the statistical and systematic uncertainties. 34
4.5 Zoom of a x-y view of the ATLAS detector showing one of the high-p_T jets of the event show in one event. The energy deposition in the calorimeters cells are displayed as light rectangles. The size of the rectangles is proportional to the energy deposits. The dark histograms attached to the LAr (Tile) Calorimeters illustrates the amount of deposited energy. The line in the ID display the reconstructed tracks originating from the interaction vertex. 36

6.1 Fractional jet energy scale systematic uncertainty as a function of p_T^{jet} for jets in the pseudo-rapidity region $0.3 \leq|\eta| \leq 0.8$ in the calorimeter barrel (a), $2.1 \leq|\eta| \leq 2.8$ in the calorimeter endcap (b), and in the forward pseudo-rapidity region $3.6 \leq|\eta| \leq 4.5$. The total uncertainty is shown as the solid light shaded area. The individual sources are also shown together with the uncertainties from the fitting procedure if applicable. 47

7.1 Transverse momentum and pseudo-rapidity of leading lepton after pre-selection. The yellow error band shows the full (statistical and systematic) error. The Monte Carlo samples are normalized by their cross-section to 1.04 fb^{-1}. 60

7.2 $\sum p_T$ after pre-selection. The yellow error band shows the full (statistical and systematic) error.The Monte Carlo samples are normalized by their cross-section to 1.04 fb^{-1}. 61

8.1 $\sum p_T$ dependencies of $\varepsilon_{\text{real}}$ and $\varepsilon_{\text{fake}}$ 69

8.2 The invariant mass $M_{\ell\ell}$ distribution for data and Monte Carlo simulation for the Z+jets CR. 70

8.3 The $\sum p_T$ distributions for data and Monte Carlo simulation for the Z+jets CR. The green histogram displays the MC $\sum p_T$ distribution after having applied the SF correction. 71

8.4 The $\sum p_T$ distributions for MC simulated W+jets (red) and $t\bar{t}$ (blue) events in the control region. 81

8.5 The $\sum p_T$ distributions for data (black points) and MC simulation (red histograms) of W+jets and $t\bar{t}$ background. For the data distribution, the small Z+jets and QCD processes have been subtracted, using the predicted shapes and normalization from the MC simulation. 82

9.1 The E_T^{miss} distributions of OS dilepton events, the error band on the SM background represent the total uncertainty. 93

9.2 The E_T^{miss} distributions of SS dilepton events, the error band on the SM background represent the total uncertainty. 94

10.1 Final $\sum p_T$ distributions for the signal region. Background processes are shown according to their data-derived estimates, as described in the text. The yellow band indicates the uncertainty on the expectation from finite statistics, jet and lepton energy scales and resolutions. Two representative signal distributions are overlaid for comparison purposes. The signal labelled "Black Hole" is a non-rotating black hole sample with $n = 6$, $M_D = 0.8$ TeV and $M_{TH} = 4$ TeV. The signal labelled "Stringball" is a rotating string ball sample with $n = 6$, $M_D = 1.26$ TeV, $M_S = 1$ TeV and $M_{TH} = 3$ TeV. The last bin in the signal sample histograms is the integral of all events with $\sum p_T \geq 3300$ GeV. 99

10.2 Final distributions for p_T of the object (jet or lepton) with the largest value of p_T for the signal region. Background processes are shown according to their data-derived estimates, as described in the text. The yellow band indicates the uncertainty on the expectation from finite statistics, jet and lepton energy scales and resolutions. Two representative signal distributions are overlaid for comparison purposes. The signal labelled "Black Hole" is a non-rotating black hole sample with $n = 6$, $M_D = 0.8$ TeV and $M_{TH} = 4$ TeV. The signal labelled "Stringball" is a rotating string ball sample with $n = 6$, $M_D = 1.26$ TeV, $M_S = 1$ TeV and $M_{TH} = 3$ TeV. The last bin in the signal sample histograms is the integral of all events with $p_T \geq 1400$ GeV. 100

10.3 95% C.L. limits on the fiducial cross sections $\sigma(pp \to \ell X)$ for the production of final states with at least 3 objects above a 100 GeV p_T cut including at least one isolated lepton, and $\sum p_T$ above threshold. The observed and expected limits according to the CL_s prescription are shown, as well as the 1σ and 2σ bounds on the expected limit. 101

10.4 Limits on the fiducial cross sections $\sigma(pp \to \ell X)$ for the production of final states with at least 3 objects above a 100 GeV p_T cut including at least one isolated lepton, and $\sum p_T$ above threshold, for all final states with at least one electron or muon. The observed and expected 95% C.L. limits according to the CL_s prescription are shown, as well as the 1σ and 2σ bounds on the expected limit. 102

10.5 95% C.L. limit in the M_{TH}-M_D plane, both channels combined, for a rotating black hole model with six extra dimensions. The solid (dashed) line shows the observed (expected) limits, with the green and yellow bands the expected 1σ and 2σ variations of the expected limits. The dotted blue lines show lines of constant $k = M_{TH}/M_D$. In this plots M_D refers to the Planck scale in extra-dimensions $M_{Pl(4+n)}$ and M_{TH} to the mass threshold of the Black Hole. 103

10.6 95% C.L. limit in the M_{TH}-M_D plane, both channels combined for rotating and non-rotating string balls with six extra dimensions. The solid (dashed) line shows the observed (expected) limits, with the green and yellow bands the expected 1σ and 2σ variations of the expected limits. The dotted blue lines show lines of constant $k = M_{TH}/M_D$. All samples were produced with the `Charybdis` generator. 104

B.1 Object diagram of the GAUDI Architecture 115
B.2 Default workflow for generators in Athena 117

C.1 Transverse momentum and pseudo-rapidity of sub-leading lepton after pre-selection. The Monte Carlo samples are normalized by their cross-section to 1.04 fb^{-1}. 120
C.2 Transverse momentum of the three most leading objects after pre-selection. The Monte Carlo samples are normalized by their cross-section to 1.04 fb^{-1}. 121
C.3 Missing transverse energy in events after pre-selection. The yellow error band shows the full (statistical and systematic) error. The Monte Carlo samples are normalized by their cross-section to 1.04 fb^{-1}. 122
C.4 Invariant mass of events after pre-selection. The yellow error band shows the full (statistical and systematic) error. The Monte Carlo samples are normalized by their cross-section to 1.04 fb^{-1}. 123

D.1 Definition of loose, medium or tight jet selections 126

F.1 Graphical representation of H_0, H_1, $f_0(x)$, $f_1(X)$ and the critical region ω. 130

G.1 Distribution of the test variable q under the $s+b$ and b hypothesis, in the plot $f(q|1)$ and $f(q|0)$ correspond to $f(q|s+b)$ and $f(q|b)$ respectively, P_b and P_{s+b} correspond to the *p-values* for the background and signal plus background models respectively. 133
G.2 Distributions of the test variable q under the $s+b$ and b hypothesis in an example where one has very little sensitivity to the signal model. 135

J.1 One of the highest-p_T event in our selection it is located in the signal region and it is a genuine black hole candidate event, it contains one isolated high-p_T muon and 4 hard jets (p_T >100 GeV), all the objects make a $\sum p_T$ ∼1.6 TeV, in the figure the jets are represented by the cones of different colors, the muon is the yellow line and the E_T^{miss} representation is the purple line 144

K.1 Transverse momentum of three most leading objects after preselection. The Monte Carlo samples are normalized by their cross-section to 1.04 fb^{-1}. 146

K.2 Lepton η, E_T^{miss} and m_T distributions for events in signal region, defined by a $\sum p_T > 700$ GeV requirement. 147

L.1 The track multiplicity distribution for same-sign di-muon events. The region with Ntrk>9 is selected as the signal region. The background histograms are stacked. The signal expectation for a non-rotating Black Hole model with parameters $M_D = 800$ GeV, M_{TH}=4 TeV, and six extra dimensions is overlaid for illustrative purposes. The bottom panels shows the ratio of data to the expected background (points) and the total systematic uncertainty on the background (shaded area). . . . 150

L.2 95% C.L. limit in the M_{TH}-M_D plane, for a rotating Black Hole model with six extra dimensions. The solid (dashed) line shows the observed (expected) limits, with the green and yellow bands the expected 1σ and 2σ variations of the expected limits. The dotted blue lines show lines of constant $k = M_{TH}/M_D$. The plot on the top refers to the Lepton plus Jets analysis and the plot on the bottom to the Same-sign di-muon one, clearly the exclusion power is bigger for the Lepton plus Jets one 151

M.1 As angle increases from zero, pseudo-rapidity decreases from infinity. In particle physics an angle of zero is usually along the beam axis. 154

List of Tables

7.1 Cut flow in collision data for the electron and muon channels. The total integrated luminosity is 1.04 fb^{-1} 56

7.2 Cut flow for individual Monte Carlo samples, through preselection, for electron and muon channels. The numbers are normalized to 1.04 fb^{-1}. 57

7.3 Cut flow for individual Monte Carlo samples, through preselection, for electron and muon channels. The two benchmark signal Black Hole and string ball samples are generated with fundamental scales and mass threshold scales of $M_D = 0.8$ TeV, $M_{TH} = 4$ TeV, and $M_S = 1$ TeV, $M_{TH} = 3$ TeV, respectively. The numbers are normalized to 1.04 fb^{-1}. 58

7.4 Events in the signal region for electron channel. Signal and background numbers are from Monte Carlo simulations, normalized by cross-section to 1.04 fb^{-1}. The quoted uncertainties are statistical only. 58

7.5 Events in the signal region for muon channel. Background numbers are from Monte Carlo simulations, normalized by cross-section to 1.04 fb^{-1}. The quoted uncertainties are statistical only. 59

8.1 Background composition in the Z+$jets$ (real lepton) dominated control region. 64

8.2 Background composition in the QCD-Multi-jet (fake lepton) dominated control region. 65

8.3 Comparison of expected number of expected QCD Multi-jet events, for the electron channel, using Alpgen and Pythia MC samples and the output of the data-driven method, as a function of $\sum p_T$ cut. The MC samples are normalized according to luminosity. 65

8.4 Variation from the nominal value of the Z+jets scale factor for different choices of $\sum p_T$ bin, for the muon channel. The nominal SF is from the 300 $<\sum p_T <$ 700 GeV bin. 67

8.5 Variation from the nominal value of the Z+jets scale factor for different choices of $\sum p_T$ bin, for the electron channel. The nominal SF is from the 300 $<\sum p_T <$ 700 GeV bin. 67

8.6 Nominal Z+jets scale factor (SF), for the muon channel, and systematic uncertainties derived from varying the jet energy scale (JES), jet energy resolution (JER), muon momentum resolution scale factors (MMR) and control region (CR) $\sum p_T$ definition. 67
8.7 Nominal Z+jets scale factor (SF), for the electron channel, and systematic uncertainties derived from varying the jet energy scale (JES), jet energy resolution (JER), electron energy resolution (EER), electron energy scale (EES) and control region (CR) $\sum p_T$ definition. 68
8.8 Number of predicted Z+jets events, for the muon channel, in the SR using Alpgen (nominal) and Sherpa. In each case, a SF is derived from the CR to scale the raw number of observed events in the SR. The last column shows the difference between the Sherpa and Alpgen predictions. 72
8.9 Number of predicted Z+jets events, for the electron channel, in the SR using Alpgen (nominal) and Sherpa. In each case, a SF is derived from the CR to scale the raw number of observed events in the SR. The last column shows the difference between the Sherpa and Alpgen predictions. 73
8.10 Fractional change in expected Z+jets background in the SR after CR normalization, for several PDF choices: `CTEQ6.6` compared to nominal `CTEQ6L1` `CTEQ6.6` with upper error set uncertainties, and `CTEQ6.6` with lower error set uncertainties (relative to `CTEQ6.6` central value). These are for the muon channel. 74
8.11 Fractional change in expected Z+jets background in the SR after CR normalization, for several PDF choices: `CTEQ6.6` relative to nominal `CTEQ6L1` `CTEQ6.6` with upper error set uncertainties, and `CTEQ6.6` with lower error set uncertainties (relative to `CTEQ6.6` central value). These are for the electron channel. 74
8.12 Relative uncertainty on number of Z+jets events in signal region due to JES, JER, EER, EES for electron channel. 75
8.13 Relative uncertainty on number of Z+jets events in signal region due to JES, JER, MMR for muon channel. 76
8.14 Relative uncertainty on Z+jets estimation for electron channel, by varying JES,JER,EES,EER (maximum between up and down considered for Total) both in both control and signal region, additional uncertainty considered from MC generator (Alpgen vs Sherpa), PDF re-weighting and control region definition 76

8.15 Relative uncertainty on Z+jets estimation for muon channel, by varying JES,JER,MMR (maximum between up and down considered for Total) both in both control and signal region, additional uncertainty considered from MC generator (Alpgen vs Sherpa), PDF re-weighting and control region definition . . 77

8.16 Estimated Z+jets background in signal region as a function of $\sum p_T$, in the electron channel, normalized according to the scale factor derived from the control region. The first quoted error is the statistical uncertainty, the second is the systematic. 77

8.17 Estimated Z+jets background in the signal region as a function of $\sum p_T$, in the muon channel, normalized according to the scale factor derived from the control region. The first quoted error is the statistical uncertainty, the second is the systematic. 77

8.18 Event composition in the W+jets/$t\bar{t}$ control region for the electron channel. The error shown is statistical only; the size of the systematic errors on the prediction are detailed in Table 8.21. 78

8.19 Predicted events in the W+jets/$t\bar{t}$ control region for the muon channel (there are zero predicted QCD events). The error shown is statistical only; the size of the systematic errors on the prediction are detailed in Table 8.20. 79

8.20 Nominal W+jets + $t\bar{t}$ scale factor (SF), for the muon channel, and systematic uncertainties derived from varying the jet energy scale (JES), jet energy resolution (JER), and muon momentum resolution scale factors (MMR). 79

8.21 Nominal W+jets + $t\bar{t}$ scale factor (SF), for the electron channel, and systematic uncertainties derived from varying the jet energy scale (JES), jet energy resolution (JER), electron energy resolution (EER) and electron energy scale (EES). 80

8.22 The number of predicted W+jets and $t\bar{t}$ events, for the muon channel, in the SR using Alpgen (nominal) and Sherpa. In each case, a SF is derived from the CR to scale the raw number of observed events in the SR. The last column shows the difference between the Sherpa and Alpgen predictions. For $\sum p_T$ $>$ 1200 GeV there are no events observed in the SR for Sherpa so we assume a 19% difference from Alpgen, taken from the $\sum p_T > 1000$ GeV bin. 83

8.23 The number of predicted W+jets and $t\bar{t}$ events, for the electron channel, in the SR using Alpgen (nominal) and Sherpa. In each case, a SF is derived from the CR to scale the raw number of observed events in the SR. The last column shows the difference between the Sherpa and Alpgen predictions. For $\sum p_T > 1500$ GeV there are no events observed in the SR for Sherpa so we assume a 27% difference from Alpgen, taken from the $\sum p_T > 1200$ GeV bin. 84

8.24 Relative uncertainty on the combined W+jets/$t\bar{t}$ events in signal region, due to variations on JES,JER,EES, and EER in the electron channel. 85

8.25 Relative uncertainty on the combined W+jets/$t\bar{t}$ events in signal region, due to variations on JES,JER and MMR in the muon channel. 85

8.26 Residual uncertainty on combined W+jets/ttbar estimation, after normalization from control region in the electron channel. 86

8.27 Residual uncertainty on combined W+jets/ttbar estimation, after normalization from control region in the muon channel . 86

8.28 Summary of systematic background uncertainties for W+jets/$t\bar{t}$ due to JES,JER,EER,EES (maximum between up and down), MC generators, ISR/FSR and PDF re-weighting electron channel 87

8.29 Summary of systematic background uncertainties for W+jets/$t\bar{t}$ due to JES,JER,MMR (maximum between up and down), MC generators, ISR/FSR and PDF re-weighting muon channel 87

8.30 Estimated combined W+jets and $t\bar{t}$ background in the signal region as a function of $\sum p_T$, in the muon channel, normalized according to the scale factor derived from the control region. The first quoted error is the statistical uncertainty, the second is the systematic. (Extrapolation uncertainties are not included on the pure MC estimate). 87

8.31 Estimated combined W+jets and $t\bar{t}$ background in signal region as a function of $\sum p_T$, in the electron channel, normalized according to the scale factor derived from the control region. The first quoted error is the statistical uncertainty, the second is the systematic. (Extrapolation uncertainties are not included on the pure MC estimate). 88

10.1 Background estimation summary as a function of $\sum p_T$ in the electron channel, using the methods described in chapter 8. The first quoted errors are statistical, the second systematic. All other backgrounds considered (WW, ZZ and WZ) are estimated to have negligible contributions. 95
10.2 Background estimation summary as a function of $\sum p_T$ in the muon channel, using the methods described in chapter 8. The first quoted errors are statistical, the second systematic. All other backgrounds considered (WW, ZZ, WZ and QCD multi-jet processes) are estimated to have negligible contributions. . 96
10.3 Expected and observed 95% C.L. upper limits on the fiducial cross sections $\sigma(pp \to \ell X)$ for the production of final states with at least 3 objects above a 100 GeV p_T cut including at least one isolated lepton, and $\sum p_T$ above threshold, for muon and electron channels separately, and for their combination (where $l = e$ or μ).The CL_s method is used to obtain the limits. . . . 97

A.1 QCD alpgen samples. Tag e600_s933_s946_r2215_r2260_p543.108
A.2 QCD alpgen $b\bar{b}$ samples. Tag e600_s933_s946_r2215_r2260_p543. 109
A.3 QCD pythia samples. Tag e574_s934_s946_r2213_r2260_p543.110
A.4 W alpgen samples. Tag e760_s933_s946_r2215_r2260_p543. 110
A.5 Z alpgen samples. Tag e737_s933_s946_r2215_r2260_p543. A k-factor of 1.25 is already included in the cross-section for consistency with the NNLO values. 111
A.6 W + bb + jets alpgen samples. Tag e600_s933_s946_r2302_r2300_p575. 111
A.7 Diboson Herwig samples. Tag e598_s933_s946_r2302_r2300_p575. 111
A.8 Top quark MC@NLO samples. Tag e598_s933_s946_r2215_r2260_p543. 112
A.9 Signal samples. BlackMax (PytBMx), Charbydis (PytChar2, CH2), $\langle 4 \rangle$-body is Poisson distributed multiplicity with mean of four, and $n\#, \# = 2, 4, 6$. In these samples gravitons can only occur in pairs in the production phase. 113

E.1 Background composition in regions A,B,C and D 128
E.2 QCD estimated events in signal region 128

H.1 Number of $t\bar{t}$ events in W+jets/$t\bar{t}$ control region normalized to 1 fb^{-1} 138

H.2 Number of $t\bar{t}$ events in signal region $\sum p_T > 700$ GeV normalized to 1 fb^{-1} 138
H.3 Uncertainty on W+jets/$t\bar{t}$ background estimation due to ISR/FSR variations and different MC samples used for $t\bar{t}$ using $\sum p_T > 700$ GeV (electron channel) 138
H.4 Uncertainty on W+jets/$t\bar{t}$ background estimation due to ISR/FSR variations and different MC samples used for $t\bar{t}$ using $\sum p_T > 700$ GeV (muon channel) 138

I.1 Fractional change in expected W+jets background in the SR after CR normalization, for several PDF choices: `CTEQ6.6` relative to nominal `CTEQ6L1` `CTEQ6.6` with upper error set uncertainties, and `CTEQ6.6` with lower error set uncertainties (relative to `CTEQ6.6` central value). These are for the muon channel. 141
I.2 Fractional change in expected $t\bar{t}$ background in the SR after CR normalization, for `CTEQ6.6` with upper error set uncertainties, and `CTEQ6.6` with lower error set uncertainties (relative to `CTEQ6.6` central value). These are for the muon channel. . . . 142
I.3 Fractional change in expected W+jets background in the SR after CR normalization, for several PDF choices: `CTEQ6.6` relative to nominal `CTEQ6L1`, `CTEQ6.6` with upper error set uncertainties, and `CTEQ6.6` with lower error set uncertainties (relative to `CTEQ6.6` central value). These are for the electron channel. 142
I.4 Fractional change in expected $t\bar{t}$ background in the SR after CR normalization, for `CTEQ6.6` with upper error set uncertainties, and `CTEQ6.6` with lower error set uncertainties (relative to `CTEQ6.6` central value). These are for the muon channel. . . . 142

Chapter 1

Introduction

1.1 Standard Model

It is believed that the behaviour of all known subatomic particles can be described within a single theoretical framework called the Standard Model [1], by incorporating quarks and leptons and their interactions through the strong, weak and electromagnetic forces. The force not described by the Standard Model is gravity. The Standard Model is the fruit of many years of international effort through experiments, theoretical ideas and discussions. It can be summarized in the following sentence: "*All the known matter in the universe today is made of quarks and leptons, held together by fundamental forces which are represented by the exchange of particles known as the gauge bosons*". Particles that are the constituents of the Standard Model theory and their properties are presented in a graphical way in Fig. 1.1.

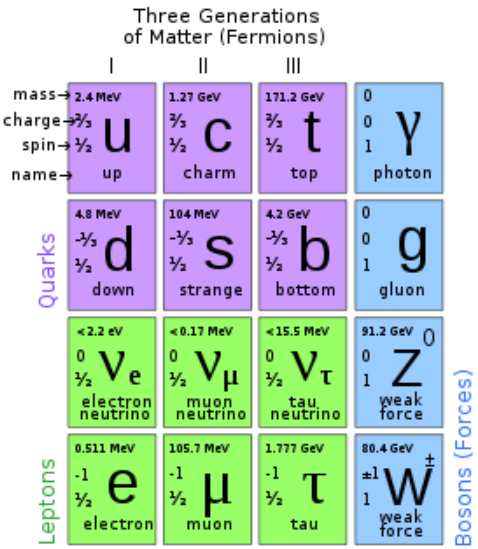

Figure 1.1: Particles constituents of the Standard Model (six leptons, six quarks and the gauge bosons) along with some of their properties like mass, charge and spin.

1.1.1 Quarks

The quark scheme [2] was suggested by the symmetries in the way the many mesons and baryons seemed to be arranged in families. Theorists Gell-Mann and Zweig independently proposed in 1964 that just three fundamental "constituents" (and their anti-particles) combined in different ways according to the rules of mathematical symmetries could explain the whole zoo of particles. Gell-Mann called these constituents quarks, and the three types were named up, down and strange quarks. Evidence for quark-like constituents of protons and neutrons became clear in the late 1960s and 1970s. In 1974, a new particle was unexpectedly discovered at SLAC (Stanford Linear Accelerator Center). It was given the dual name J/ψ, because of its simultaneous discovery by two groups of experimenters. The J/ψ was later shown to be a bound state of a completely new quark-antiquark pair, which nevertheless had been predicted on the basis of a subtle phenomenon. The new fourth quark was named charm. The four-quark scheme was extended to its present state of six quarks by the addition of a new pair, in a prediction by theorists Kobayashi and Maskawa (collectively known as CKM). So now we have the six quarks: up, down, strange, charm, bottom and top quarks and they each have their partner anti-quarks. The quarks are usually labeled by their first letters: *u, d, s, c, b* and *t*. In various combinations they make up all the mesons and baryons that have been seen.

In 1977 a new heavy meson called the Upsilon was discovered at Fermilab and later shown to be the bound state of the bottom (b) and anti-bottom ($\bar{b}$) quark pair. The B meson, containing an anti-b quark and a u or d quark was discovered by the CLEO experiment at Cornell in 1983. Finally, in 1998 the six-quark prediction was fulfilled when conclusive evidence of the existence of the super heavy top quark was obtained at Fermilab.

1.1.2 Leptons

The leptons behave differently from the mesons and baryons. First, they are much less massive. The mass of the electron is almost 2,000 times smaller than the mass of the proton, and the muon appears to be just a heavier version of the electron, its mass being nine times smaller than that of the proton. The neutrino has almost no mass at all, and up until recently, its mass was thought to be truly zero. Hence the name "leptons" or light particles. Second, the electron and muon interact with matter mainly through their electric charges; the neutrino being neutral, hardly at all. They all have a weak interaction with the matter in nuclei and, in high energy collisions, they do not produce new mesons and baryons that protons and neutrons do

when colliding with nuclei. In 1962, the first experiment using a high-energy neutrino beam showed that the electron has its own electron-neutrino (ν_e), and the muon its own distinct muon-neutrino (ν_μ). This was the very first evidence that there could be families or generations of pairs of fundamental particles. This notion was dramatically extended in 1974, when shortly after the discovery of the J/ψ, a new heavy lepton was discovered, called the tau (τ), almost twice as massive as the proton, but behaving like the other leptons, sharing the weak interaction property. This was the first evidence that three pairs or families of leptons existed: the electron and electron-neutrino, the muon and muon-neutrino and the tau and tau-neutrino. Quarks and leptons have an intrinsic angular momentum called spin, equal to a half-integer (1/2) of the basic unit and are labeled as fermions. Particles that have zero or integer spin are called bosons.

1.1.3 Forces and Interactions

The fundamental forces or interactions among the quarks and leptons are: Gravity, Weak, Electromagnetism, and the Strong Force. The intrinsic strengths of the forces can be compared relative to the strong force considered here to have unit strength. In these terms, the electromagnetic force has an intrinsic strength of (1/137). The weak force is a billion times weaker than the strong force. The weakest of them all is the gravitational force. This may seem strange, since it is strong enough to hold the massive Earth and planets in orbit around the sun, but we know that the gravitational force between two bodies a distance r apart is proportional to the product of the two masses (M and m) and inversely proportional to the distance r squared:

$$F_G = \frac{GMm}{r^2} \tag{1.1}$$

The meaning of intrinsic strength is given by the magnitude of the universal force constant G, independent of the masses or distances involved. In similar terms, the electromagnetic force between two particles is proportional to the product of the two charges (Q and q) and inversely to the distance r squared:

$$F_{em} = \frac{\alpha Qq}{r^2} \tag{1.2}$$

Here the universal constant alpha (α) gives the intrinsic strength. We can compare the relative strengths of the electromagnetic repulsion and the gravitational attraction between two protons of unit charge using the above equations. Independent of the distance, the ratio turns out to be $F_{em}/F_G = 10^{36}$. Thus the two protons will repel each other and fly apart, easily overcoming

the tiny gravitational attraction. Forces can be represented in the theory as arising from the exchange of specific particles called gauge bosons. All the bosons have zero or integer spins. The carriers of the strong force are called gluons, the "glue" that holds quarks together in protons and neutrons. The carriers of the weak force are called weak bosons: the $W^{\pm}$ and the Z^0 . The carriers of the gravitational field are called gravitons and are unique in having a spin of 2.

1.1.4 Unification

For decades physicists have been dreaming about the unification of the four forces into one universal force that existed at least in the primordial stage of the Universe. It is not quite satisfactory to have four different theories to account for these four forces. The electromagnetic interaction of particles is explained by a well established modern theory of Quantum Electrodynamics (QED). The weak interaction had its own theory but these two have now been combined as the Electroweak Theory in the Standard Model. The strong interaction between quarks and gluons has another theory called Quantum Chromodynamics (QCD), where the equivalent of electric charge is named "color". And Einstein's General Theory of Relativity explains how the gravity we know is a manifestation of the basic geometry of space-time. The intrinsic strengths of the four different interactions could depend on the "temperature" of energy level of the interaction. Although these strengths are quite different at present temperatures (e.g., at 300K or equivalent energy of about 1/40 eV), the weak interaction depends strongly on the energy, and in collisions at near 1000 GeV, it gets just as strong as the electromagnetic interaction. The Electroweak theory of the Standard Model explains all this. The basic equations are symmetric in the way the two interactions occur and in fact the masses of all the quanta are zero. However, as the temperatures drops, the symmetry is broken and the quanta split up into four different gauge bosons of different masses: the $W^{\pm}$ (80 GeV), the Z^0 (91 GeV) and the photon with zero mass. At "room temperature" , the massive W and Z do not play an important part. But at very high energies of 300 GeV or more, the difference between the zero mass photon and the heavier W and Z bosons is erased, and they all act equally strongly. In 1983 the W boson and in 1984 the Z boson were observed at the CERN laboratory in Geneva, in high energy collisions of protons with anti-protons. They had the predicted masses. There is however one piece of evidence yet to be found. We mentioned above that the basic symmetry of the Electroweak theory is broken as the temperature drops and the forces separate in strength as the bosons gain mass. The culprit that causes this is actually a new field called the Higgs field. It is possible to

visualize how this works. Recall that mass is a manifestation of inertia or resistance to acceleration. If a Higgs field suddenly permeates all of space as the Universe cools, it can act as a drag on every particle moving in space, the drag depending on how well each interacts with the Higgs field. This drag shows up as inertia and thus a measurable mass of the particles that were originally mass-less. But now we have to look for the boson that carries this field the Higgs boson. This is now the one feature of the Standard Model still needed to clinch the picture. From recent results the Higgs boson shows slightly preference to have a mass in the range of 115-127 GeV, still to be confirmed with the coming data.

1.2 Beyond the Standard Model

Theories, called "Grand Unification Theories" or GUTs, have been proposed to unify the Electroweak force with the strong force. But so far no concrete evidence has been found for them. Beyond that, the holy grail of unification has long been the unification of gravity with all the other forces. Einstein himself labored in vain to fit gravity into a scheme where it could be compatible with quantum theory. The theory of Supersymmetry (SUSY) requires a whole new set of particles beyond the Standard Model complement: a heavy partner for each quark, lepton and gauge boson of the old set, together all of them making up one great super-family of particles. The three forces strong, electromagnetic and weak all have exactly equal strengths in this theory at a very high energy. And of course, it gives experimentalists a whole new game of looking for new particles. It is just possible that one of these new super particles is a primordial relic of the Big Bang and makes up the Dark Matter in the Universe, a further incentive to discover these super-partners. Meanwhile theoretical studies range far and wide in a search for the Theory Of Everything (TOE). Most familiar is String Theory, which pictures particles as infinitesimal little vibrating loops of strings in 10 dimensions. Further refinements lead to Membrane Theory, with the entire Universe regarded as existing on multidimensional sheets or membranes, with particles as loops anchored on "our" sheet and gravitons ranging into the continuum between sheets. We await predictions that can be tested.

1.3 The Hierarchy problem and a proposed solution in extra-dimensions

It seems that there are at least two fundamental energy scales in nature, the Electroweak scale $m_{EW} \sim 10^3$ GeV, and the Planck scale $M_{Pl} \sim 10^{19}$ GeV[1], where the strength of gravity is believed to become as strong as the Electroweak interactions. There has been many efforts in order to find an explanation for the immense order of magnitude difference between these two fundamental scales, which motivates the development of theories beyond the Standard Model.

A shocking fact about this Hierarchy problem is that while the Electroweak interactions have been measured at distances $\sim m_{EW}^{-1}$, the gravitational forces are still far away to been measured at distances $\sim M_{Pl}^{-1}$, in fact recent experiments [3] have reported results only at the micron scale, with the conclusion that no deviation from Newtonian gravity has been observed at such scale yet. Therefore our belief in M_{Pl} as a fundamental scale in nature has been justified by the assumption that gravity remains unmodified over the order of magnitudes from the micron to the Planck scale, over the last decades such long extrapolation has been questioned and it has motivated the search for new alternatives to the standard picture of physics beyond the Standard Model

Proposals that address this so-called Hierarchy problem within the context of extra-dimension scenarios have appeared in the last years [4]. In these scenarios the Standard Model of particle physics is confined to a three dimensional brane in a higher dimensional space, one of the most famous models using extra-dimensions is the ADD model (due to the initial of its authors: Arkani-Hamed, Dimopoulos and Dvali). This model assumes that there are **n** extra compact spacial dimensions of radius $\sim$ R. The Planck scale $M_{Pl(4+n)}$ of this (4+n) dimensional theory is taken to be $\sim m_{EW}$.

If two test masses m_1, m_2 are placed within a distance $r \ll R$, They will feel a gravitational potential given by the Gauss's law in (4+n) dimensions as in equation 1.3.

$$V(r) \sim \frac{m_1 m_2}{M_{Pl(4+n)}^{n+2}} \frac{1}{r^{n+1}}, (r \ll R) \tag{1.3}$$

[1]Planck units are physical units of measurement defined exclusively in terms of five universal physical constants, the speed of light in vacuum c, the Gravitational constant G, the reduced Planck constant $\hbar$, the Coulomb constant $(4\pi\varepsilon_0)^{-1}$ and the Boltzman constant k_B, the Planck energy scale 1.22×10^{19} GeV corresponds by the mass-energy equivalence to the Planck mass 2.17645×10^{-8} kg which is given by $m_P = \sqrt{\frac{\hbar c}{G}}$, the Planck length is given by $l_p = \sqrt{\frac{\hbar G}{c^3}}$ and it has a value of 1.616199×10^{-35} m.

On the other hand, if the masses are placed at distances $r \gg R$, their gravitational flux lines can not continue to penetrate in the extra dimensions, and the usual $1/r$ potential is obtained as in equation 1.4,

$$V(r) \sim \frac{m_1 m_2}{M_{Pl(4+n)}^{n+2} R^n} \frac{1}{r}, (r \gg R) \tag{1.4}$$

Comparing equation 1.4 with the 4-dimensional potential the following relation holds

$$M_{Pl}^2 \sim M_{Pl(4+n)}^{2+n} R^n \tag{1.5}$$

Putting $M_{Pl(4+n)} \sim m_{EW}$ and demanding that R be chosen to reproduce the observed M_{Pl} yields

$$R \sim 10^{\frac{30}{n}-17} cm \times \left(\frac{1TeV}{m_{EW}}\right)^{1+\frac{2}{n}} \tag{1.6}$$

For n=1, $R \sim 10^{13}$cm, which implies deviations from Newtonian gravity over solar system distances, so this case is empirically excluded. For $n \geq 2$ experiments are looking for Newtonian gravity deviations in those ranges.

While gravity has not been measured at distances below the micron scale, the SM gauge forces have certainly been accurately measured at weak scale distances. Therefore, the SM particles cannot freely propagate in the extra **n** dimensions, but must be localized to a 4 dimensional sub-manifold. The only fields propagating in the (4+n) dimensional bulk are the (4+n) dimensional graviton, with coupling suppressed by the (4+n) dimensional Planck mass $\sim m_{EW}$.

There are important experimental consequences of this framework. First, as already mentioned gravity becomes comparable in strength to the gauge interactions at energies $m_{EW} \sim$ TeV[g][2], another consequence is that the Large Hadron Collider (LHC) and Next Linear Collider (NLC) would then not only probe the mechanism of Electroweak symmetry breaking, they could also probe the quantum theory of gravity.

1.4 Black Holes: Stellar and microscopic

A common Black Hole definition can be summarized in the following sentence: *A Black Hole is a region of space from which nothing, not even the light, can escape. The theory of general relativity predicts that a sufficiently compact mass will deform space-time to form a Black Hole.*

[2]The terms with "g" refer to non-usual concepts and the definition can be found in the appendix M

1.4.1 Stellar Black Holes

The stellar Black Holes are formed from the gravitational collapse of a star with more than 3 solar masses. The formation of a star begins when gases are pulled out by gravity, then hydrogen atoms combine with other hydrogen atoms to release incredible amount of nuclear energy in a process known as fusion, the star threathens to explote and rip apart, but gravity, the same force that created the star, now threatens to crush it. As a result there is a balance or equilibrium between gravity and heat pressure. Nevertheless radiation pressure from the fusion reactions, unlike gravity, is lost with time. Over billions of year, the star fuses hydrogen into helium and on so on until iron, when the fusion process requires more than it releases the balance is broken and gravity wins over the heat pressure.

When a star has exhausted its fuel supply, gravitational forces crush the star to end in one of the three possible outcomes:

- The star shrinks and stabilizes into a white dwarf
- The star crunches into a neutron star
- The star collapses to a Black Hole

To have an idea of the dimensions of the three possible endings we can compare with the size of our sun as presented in Fig. 1.2

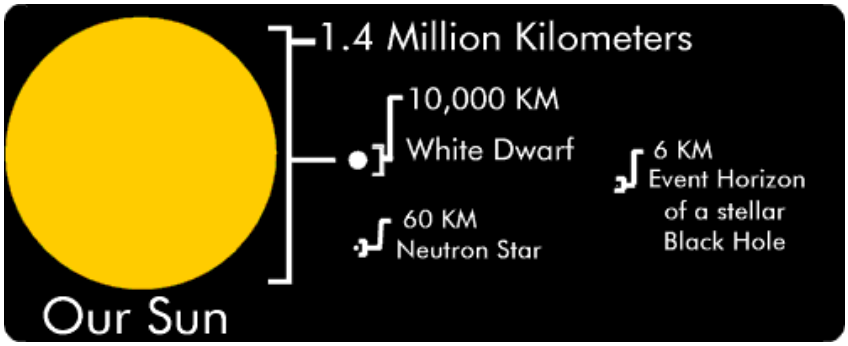

Figure 1.2: Comparison of a White Dwarf, a Neutron Star and the Event Horizon of a Black Hole with the size of our sun.

1.4.1.1 Properties of Stellar Black Holes

Black Hole surface is defined by an "event horizon" [5], which plays the role of a virtual surface. The event horizon is a one-way membrane through which

matter and energy can fall in from the outside, but nothing, not event light, can escape from within.

The simplest Black Hole have mass but neither electric charge nor angular momentum. These Black Holes are often referred to as Schwarzchild Black Holes after Karl Schwarzchild who discovered this solution of Einstein's equation in 1916. Solutions describing more general Black Holes also exist. Charged black holes are described by the Reissner-Nordstrom metric, while the Kerr metric describes a rotating Black Hole. While the mass of a Black Hole can take any positive value, the charge and angular momentum are constrained by the mass. In Planck units, the total electric charge Q and the total angular momentum J are expected to satisfy

$$Q^2 + \left(\frac{J}{M}\right)^2 \leq M^2 \tag{1.7}$$

Black Holes are commonly classified according to their mass, independent of angular momentum J or electric charge Q. The size of a Black Hole, as determined by the radius of the event horizon, or Schwarzchild radius[g][3], is roughly proportional to the mass M through

$$R_S = \frac{2GM}{c^2} \sim 2.95 \frac{M}{M_{sun}} km \tag{1.8}$$

where R_s is the Schwarzchild radius and M_{sun} is the mass of our sun. This relation is exact only for Black Holes with zero charge and angular momentum, for more general Black Holes it can differ up to a factor of 2.

1.4.1.2 Hawking radiation

A stellar Black Hole is expected to swallow all the matter and energy in the surrounding region into it, as a result of the intense gravitational fields. However, in 1972 the Israeli physicist Jacob Bekenstein suggested that Black Holes should have a well-defined entropy, and with this initiated the development of Black Hole thermodynamics, including the emission of energy.

In 1974, Stephen Hawking worked out the exact theoretical model for how a Black Hole could emit black body radiation. In a simplified version of the explanation, Hawking predicted that energy fluctuations from the vacuum causes the generation of particle-antiparticle pairs near the event horizon of the Black Hole. One of the particles falls into the Black Hole while the other escapes, before they have an opportunity to annihilate each other. The net

[3]The terms with "g" refer to non-usual concepts and the definition can be found in the appendix M

result is that, to someone viewing the Black Hole, it would appear that a particle had been emitted.

Since the particle that is emitted has a positive energy, the particle that gets absorbed by the Black Hole has a negative energy relative to the outside universe. This results in the Black Hole losing energy, and thus mass.

1.4.2 Microscopic Black Holes: production at the LHC

Searches for TeV-scale gravity signatures like Black Hole production are part of the many searches beyond the Standard Model. One of the exciting consequences of TeV-scale quantum gravity is the possibility of production of Microscopic Black Holes (MBHs) and String Balls [6] (highly excited string states)[4] at the LHC and beyond. MBHs could be produced if the fundamental Planck scale in (4+n) dimensions ($M_{Pl(4+n)}$) is of the order of ∼TeV (as postulated in the ADD model, section 1.3). Within the context of this model, experimental lower limits on the value of $M_{Pl(4+n)}$ have been obtained from experiments at LEP [7] and the Tevatron [8] experiments, as well as at ATLAS [9] and CMS [10] by searching the production of the heavy Kaluza-Klein gravitons associated with the extra dimensions. The most stringent limits [9] come from the LHC analyses that search for non-interacting gravitons recoiling against a single jet (monojet and large missing transverse energy signature), and range from $M_{Pl(4+n)} > 2.0$ TeV, for n=6, to $M_{Pl(4+n)} > 3.2$ TeV, for n=2. Due to the greatly enhanced strength of gravitational interactions at short distance, or high energies, the formation of non-perturbative gravitational states such as Black holes or String balls at the LHC is another signature of extra dimensional models.

We consider in this analysis Black Holes of mass M_{BH} of the order of the fundamental Planck scale $M_{Pl(4+n)}$, experimentally limited by the proton-proton center of mass energy.

1.4.2.1 Production of Black Holes

The Schwarzdhild radius R_S of an (4+n)-dimensional Black Hole is given by equation 1.9 assuming that extra dimensions are large ($\gg R_s$) [11]

$$R_S = \frac{1}{\sqrt{\pi} M_{Pl(4+n)}} \left[\frac{M_{BH}}{M_{Pl(4+n)}} \left(\frac{8\Gamma(\frac{n+3}{2})}{n+2} \right) \right]^{\frac{1}{n+1}} \tag{1.9}$$

Consider two partons with the center of mass energy $\sqrt{s} = M_{BH}$ moving in opposite directions. Semi-classical reasoning suggests that if the impact

[4] For the rest of this thesis when refereeing to Microscopic Black Holes also include String balls unless explicitly noted.

parameter is less than the (higher dimensional) Schwarzchild radius (as seen in Fig. 1.3), a Black Hole with mass M_{BH} forms. Therefore the total cross section can be estimated from geometrical arguments and is of the order

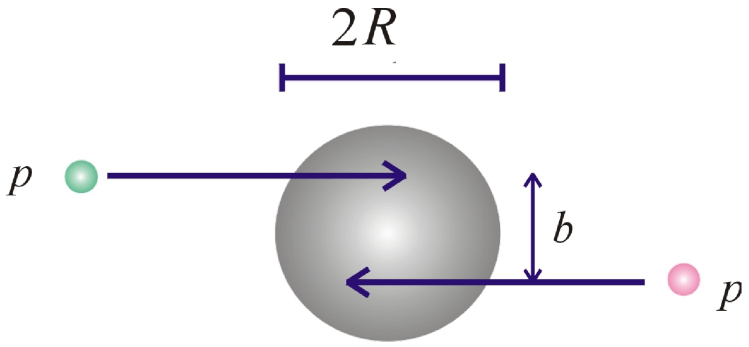

Figure 1.3: Graphical representation of two partons colliding with an impact parameter b less than the higher dimensional Schwarzchild radius.

$$\sigma(M_{BH}) \sim \pi R_S^2 = \frac{1}{M_{Pl(4+n)}^2}\left[\frac{M_{BH}}{M_{Pl(4+n)}}\left(\frac{8\Gamma(\frac{n+3}{2})}{n+2}\right)\right]^{\frac{2}{n+1}} \tag{1.10}$$

If the partons center of mass energy $\sqrt{s}$ reaches the higher dimensional Planck scale $M_{Pl(4+n)} \sim TeV$ then the cross section is of order $TeV^{-2} \sim 400$ pb. At the LHC, Black holes are expected to be produced copiously, to calculate the total production cross section, we need to take into account that only a fraction of the total center of mass energy in a pp collision is achieved in a parton-parton scattering. The full particle level cross section is computed using the parton luminosity[g][5] approach

$$\frac{d\sigma(pp \to BH + X)}{dM_{BH}} = \frac{dL}{dM_{BH}}\hat{\sigma}(ab \to BH)|_{\hat{s}=M_{BH}^2} \tag{1.11}$$

Where the parton luminosity dL/dM_{BH} is defined as the sum over all the initial parton types:

$$\frac{dL}{dM_{BH}} = \frac{2M_{BH}}{s}\sum_{a,b}\int_{M_{BH}^2/s}^{1}\frac{dx_a}{x_a}f_a(x_a)f_b\left(\frac{M_{BH}^2}{sx_a}\right) \tag{1.12}$$

and $f_i(x_i)$ are the parton distribution functions (PDFs)

[5]The terms with "g" refer to non-usual concepts and the definition can be found in the appendix M

1.4.2.2 Decay of Black Holes

The decay of the Black Holes is governed by its Hawking temperature T_H, which is proportional to the inverse radius, and is given by 1.13 [11].

$$T_H = M_{Pl(4+n)} \left(\frac{M_{Pl(4+n)}}{M_{BH}} \frac{n+2}{8\Gamma\left(\frac{n+3}{2}\right)} \right)^{\frac{1}{n+1}} \frac{n+1}{4\sqrt{\pi}} \tag{1.13}$$

As the parton collision energy increases, the resulting Black Hole gets heavier and its decay products get colder. Note that the wavelength $\lambda = \frac{2\pi}{T_H}$ corresponding to the Hawking temperature is larger than the size of the Black Hole. Therefore, the BH is, to first approximation, a point-radiator and therefore emits s-waves. This indicates that it decays equally to a particle on the brane and in the bulk, since it is only sensitive to the radial coordinate and does not make use of the extra angular modes available in the bulk. Since there are many more particles on our brane than in the bulk, this has the crucial consequence that the Black Hole decays visibly to Standard Model (SM) particles.

The average multiplicity of particles produced in the process of BH evaporation is given by $< N >= \left\langle \frac{M_{BH}}{E} \right\rangle$ where E is the energy spectrum of the decay products. In order to find $< N >$, we note that the BH evaporation is a black body radiation process, with the energy flux per unit time given by Planck's formula $df/dx \sim \frac{x^3}{e^x \pm c}$ where $x \equiv E/T_H$, and c is a constant which depends on the quantum statistics of the decay products (c= -1 for bosons, +1 for fermions, and 0 for Boltzmann statistics).

The spectrum of the Black Hole decay products in the mass-less particle approximation is given by: $\frac{dN}{dE} \sim \frac{1}{E}\frac{df}{dE} \sim \frac{x^2}{\exp x \pm c}$ In order to calculate the average multiplicity of the particles produced in BH decay, we use the average of the distributions in the inverse particle energy:

$$\left\langle \frac{1}{E} \right\rangle = \frac{1}{T_H} \frac{\int_0^\infty dx \frac{1}{x} \frac{x^2}{e^x \pm c}}{\int_0^\infty dx \frac{x^2}{e^x \pm c}} = \frac{a}{T_H} \tag{1.14}$$

where a is a dimensionless constant that depends on the type of the produced particles and numerically equals 0.68 for bosons, 0.46 for fermions, and 1/2 in Boltzmann statistics. Since a mixture of fermions and bosons is produced in the BH decay, we can approximate the average by using Boltzmann statistics, which gives the following formula for the average multiplicity $< N > \sim \frac{M_{BH}}{2T_H}$, using equation for Hawking's temperature, we obtain

$$< N >= \frac{2\sqrt{\pi}}{n+1} \left(\frac{M_{BH}}{M_{Pl(4+n)}} \right)^{\frac{n+2}{n+1}} \left(\frac{8\Gamma\left(\frac{n+3}{2}\right)}{n+2} \right)^{\frac{1}{n+1}} \tag{1.15}$$

Equation (1.15) is reliable when the mass of the BH is much larger than the Hawking temperature, i.e. $<N> \gg 1$, otherwise, Planck spectrum is truncated at $E \sim M_{BH}/2$ by the decay kinematics. The average number of particles produced in the process of BH evaporation is shown in Fig. 1.4 d) as a function of $M_{BH}/M_{Pl(4+n)}$ for several values of n [11].

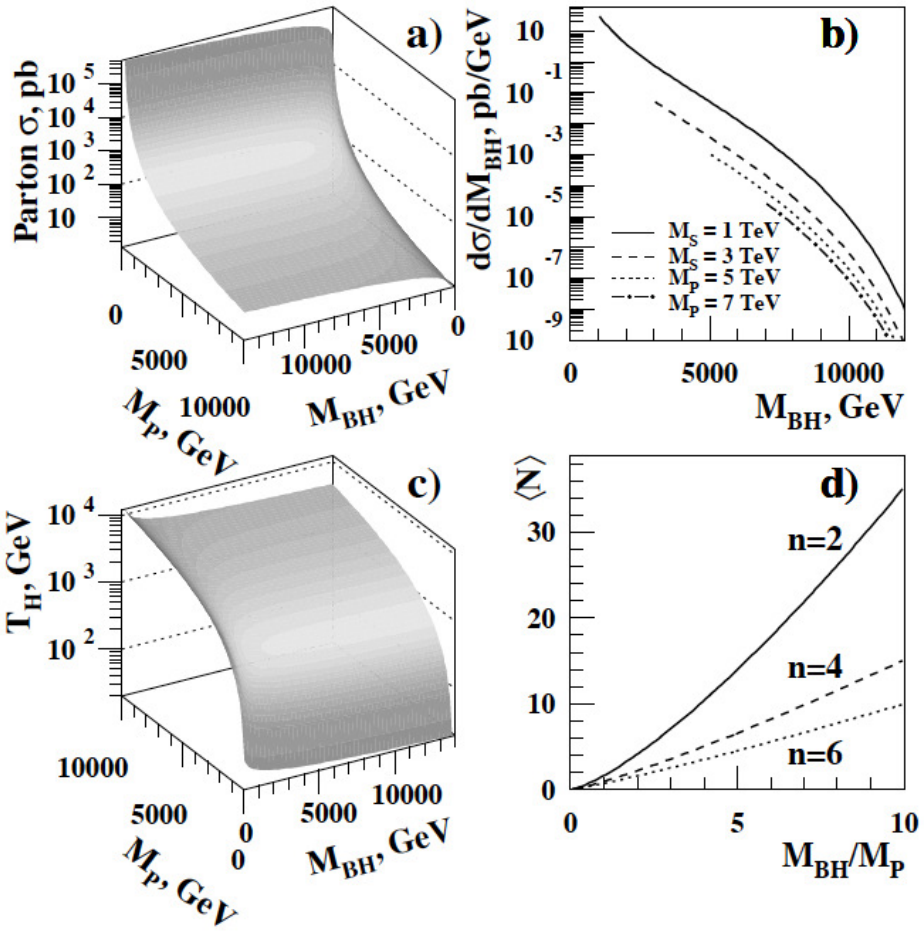

Figure 1.4: a) Parton-level production cross section, b) differential cross section $d\sigma/dM_B$ at the LHC, c) Hawking temperature, and d) average decay multiplicity for a Schwarzchild Black Hole. The number of extra spacial dimensions n=4 is used for a)-c). The dependence of the cross section and Hawking temperature on n is weak and would be hardly noticeable on the logarithmic scale. The M_P in the plots correspond to the higher dimensional Planck scale $M_{Pl(4+n)}$ mentioned in this section

The Blackhole/String-Ball cross sections (discussed in section 1.4.2.1) and the object multiplicity discussed in this section are used as an input for the

different Black Hole Monte Carlo generators described in section 5.2.

1.4.2.3 Leptons in MBHs decay

In the Standard Model there are six leptons, in MBHs decays we expect $\sim 10\%$ of the particles to be hard primary leptons carrying hundreds of GeV of energy. This is a very clean signal, with negligible background, as the production of SM leptons occurs at a much smaller rate than the BH production as noticed in Fig. 1.5. These events are also easy to trigger on, since they contain at least one prompt lepton with the energy above 100 GeV, as well as energetic jets[g6]. Since there are three neutrinos, we expect only $\sim 5\%$ average missing transverse energy[g] per event[g], which allow us to precisely estimate the MBH mass from the visible decay product [11].

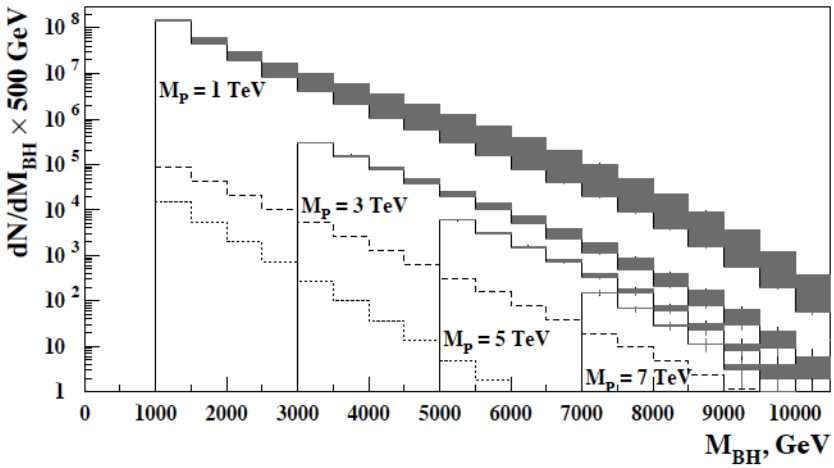

Figure 1.5: Number of MBHs produced at the LHC in the electron or photon decay channels, with 100 fb^{-1} of integrated luminosity, as a function of the BH mass. The shaded regions correspond to the variation in the number of events for n between 2 and 7. The dashed line shows total SM background (from inclusive Z(ee) and direct photon production). The dotted line corresponds to the Z(ee)+X background alone. The M_P in the plot correspond to the higher dimensional Planck scale $M_{Pl(4+n)}$ mentioned in this section.

[6]The terms with "g" refer to non-usual concepts and the definition can be found in the appendix M

1.4.2.4 Previous MBHs experimental searches

Searches for MBHs have previously been performed in ATLAS and CMS experiments by investigating final states with multiple high-pT objects [12]- [13], high-pT jets only [14] and in di-muon events [15].

The analysis in this thesis searches for an excess of multi-object events produced at high transverse momentum (high-p_T), defined as the sum of p_T of the reconstructed objects considered (hadronic jets, electrons and muons). Only events containing at least one isolated electron or muon are selected. While jets should dominate the decays of MBHs, the rate for lepton production is anticipated to be sizable, as noted above, and the requirement of a high-pT lepton significantly reduces the dominant multi-jet background, of which our knowledge of the production at LHC energies is limited, whilst maintaining a high efficiency for Black Hole events. This search considers final states with three or more selected objects (leptons or jets), and consequently is not sensitive to two-body final states [16].

Chapter 2

LHC and the ATLAS detector

2.1 The Large Hadron Collider (LHC)

The Large Hadron Collider (LHC) [17] is a proton-proton collider designed to reach 14 TeV center of mass collision energy and a luminosity of $10^{34} cm^{-2} s^{-1}$. It is located at the 27 km long LEP [19] tunnel. The aim of the LHC is to reveal the physics beyond the Standard Model such as the Higgs particle and the study of rare events. It is currently working at half of its designed center of mass collision energy, from 2010 until 2011 colliding protons with a center of mass collision energy of 7 TeV, preparing to move in 2012 to 8 TeV and finally an upgrade around the year 2015 to reach the 14 TeV. An schematic view of the tunnel and the four most important detectors is presented in Fig. 2.1.

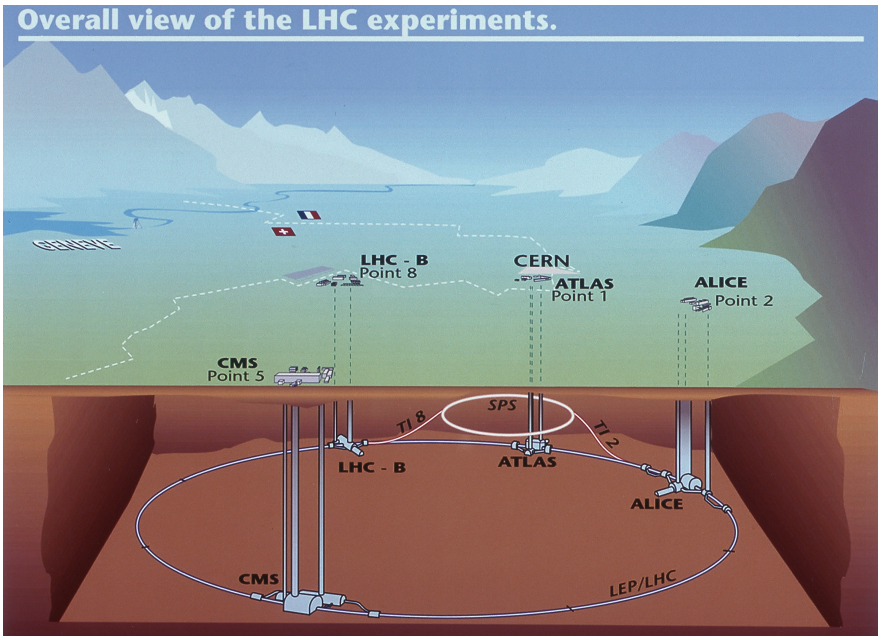

Figure 2.1: Schematic view of the Large Hadron Collider (LHC) experiment, showing the four most important particle detection points around the tunnel.

The number of events per second generated by the LHC collisions is given

by equation 2.1

$$N_{events} = L\sigma_{events} \tag{2.1}$$

Where σ_{event} is the cross section for the event under study and L is the machine luminosity, the machine luminosity depends only on the beam parameters and can be written for a Gaussian beam distribution as in equation 2.2 [18]:

$$L = \frac{N_b^2 n_b f_{rev} \gamma_r}{4\pi\varepsilon_n \beta^*} F \tag{2.2}$$

where N_b is the number of particles per bunch, n_b the number of bunches per beam, f_{rev} the revolution frequency, γ_r the relativistic gamma factor, ε_n, the normalized transverse emittance[1], β^* the beta function[2] at the collision point and F the geometric luminosity reduction factor due to crossing angle at the interaction point (IP)

$$F = I/\sqrt{1 + \left(\frac{\theta_c \sigma_Z}{2\sigma^*}\right)^2} \tag{2.3}$$

where θ_c is the full crossing angle at the IP, σ_z the RMS bunch length and σ^* the transverse RMS beam size at the IP. The above expression assumes equal beam parameters for both circulating beams. The detection of rare events in the LHC collisions requires of both high beam energies and high beam intensities.

The LHC has two high luminosity experiments, ATLAS (A Toroidal LHC apparatus) and CMS (Compact Muon Solenoid), both of them aiming at a peak luminosity of $L = 10^{34} cm^{-2} s^{-1}$ in the LHC in proton operation. In addition to these high luminosity experiments. LHCb for b-physics aiming at a peak luminosity of $L = 10^{32} cm^{-2} s^{-1}$ and TOTEM for the detection of protons from elastic scattering at small angles aiming at a peak luminosity of $L = 2 \times 10^{29} cm^{-2} s^{-1}$ with 156 bunches. In addition to the proton beams the LHC operates with ion beams. The LHC has a dedicated ion experiment ALICE aiming at a peak luminosity of $L = 10^{27} cm^{-2} s^{-1}$ for nominal $Pb - Pb$ ion operation.

The high beam intensity required for a luminosity of $L = 10^{34} cm^2 s^{-1}$ excludes the use of anti-proton beams, and hence excludes the particle-anti-particle collider configuration of a common vacuum and magnet system for

[1] Emittance can be defined as the smallest opening you can squeeze the beam through, and can also be considered as a measurement of the parallelism of a beam, the emittance of the LHC is about 4 micrometers, a low emittance value means a higher luminosity

[2] β is roughly the width of the beam divided by the emittance. If β is low, the beam is narrower "squeezed". If β is high, the beam is wide and straight

both circulating beams, as used for example in the Tevatron, to collide two counter-rotating proton beams requires opposite magnetic dipole fields in both rings. The LHC is therefore designed as a proton-proton collider with separate magnetic fields and vacuum chambers, both of them enclosed inside the same cryostat, as can be seen in Fig. 2.2

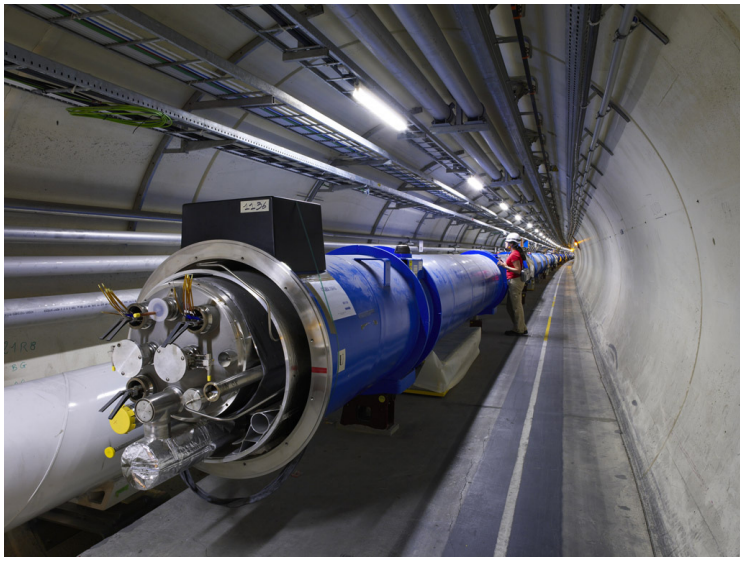

Figure 2.2: Internal view of the LHC tunnel

2.2 The ATLAS detector

ATLAS [20] is a particle physics experiment at the Large Hadron Collider (LHC) at CERN. An schematic view of the ATLAS detector is presented in Fig. 2.3. In the following sections a brief description of each sub-detector is given.

2.2.1 Inner Detector

The ATLAS inner detector (Fig. 2.4) combines high-resolution detectors at the inner radii with continuous tracking elements at the outer radii, all contained in the central solenoid, which provides a nominal magnetic field of 2 Teslas. The highest granularity is achieved around the vertex region using semiconductor pixel detectors followed by a silicon micro-strip detector. Typically for each track[g][3] the pixel detector contributes three and the strips fours

[3]The terms with "g" refer to non-usual concepts and the definition can be found in the appendix M

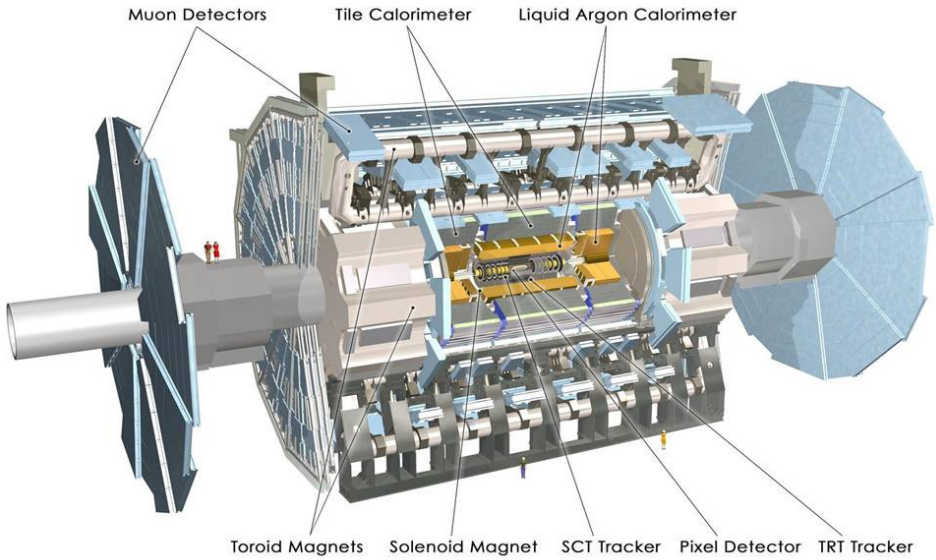

Figure 2.3: Schematic view of the ATLAS detector and its sub-detector components

space points. At larger radii typically 37 tracking points are provided by the straw tube tracker. The relative precision of measurement is well matched, so that no single measurement dominates the momentum resolution. The outer radius of the inner detector is 1.15m, and the total length 7 m. In the barrel region the high precision detectors are arranged in concentric cylinders around the beam axis, while the end-cap detectors are mounted on disks perpendicular to the beam axis. The barrel TRT straws are parallel to the beam direction. All end-cap tracking elements are located in planes perpendicular to the beam direction

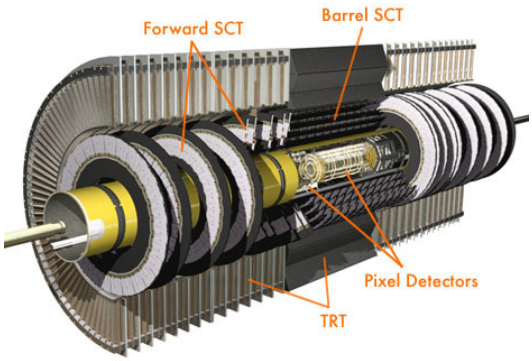

Figure 2.4: Inner detector components

2.2.2 Calorimetry

Highly granular liquid-argon (LAr) electromagnetic sampling calorimetry, with excellent performance in terms of energy and position resolutions, cover the pseudo-rapidity[g] range $|\eta| < 3.2$, (see Fig. 2.5). In the end-caps, the LAr technology is also used for the hadronic calorimeters, which share the cryostats with the EM end-caps. The same cryostats also house the special LAr forward calorimeters which extend the pseudo-rapidity coverage to $|\eta| < 4.9$. The bulk of the hadronic calorimetry is provided by a novel scintillator-tile calorimetry, which is separated into a large barrel and two smaller extended barrel cylinders, one on each side of the barrel. The overall calorimeter system provides the very good jet and E_T^{miss} performance of the detector.

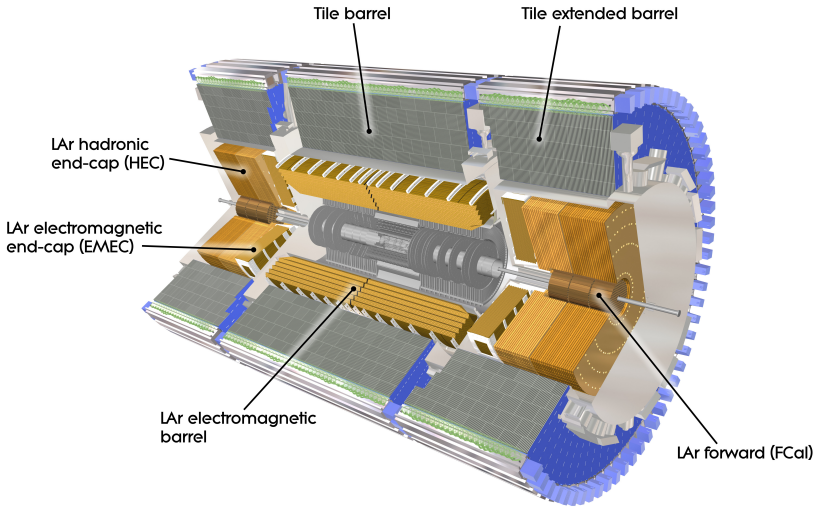

Figure 2.5: Electromagnetic and Hadronic calorimeters and their components

2.2.3 Muon spectrometer

The calorimeter is surrounded by the muon spectrometer (Fig. 2.6). The air-core toroid system, with a long barrel and two inserted end-cap magnets, generates a large magnetic field volume with strong bending power with a light and open structure. Multiple-scattering effects are thereby minimized, and excellent muon momentum resolution is achieved with three stations of high precision tracking chambers. The muon instrumentation also includes a key component trigger chambers with very fast time response

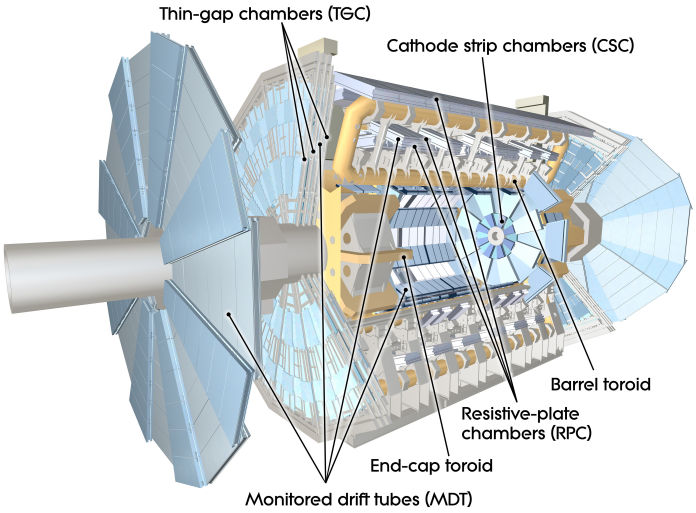

Figure 2.6: Moun spectrometer and its components

Chapter 3

Trigger and Data Acquisition

From the huge amount of proton-proton collision events generated at the LHC, the detector ATLAS records just a part of it, due to the limited storing space and the selection of only interesting events, such selection is done through the ATLAS trigger and DAQ system [21] which is based on three levels of event selection (graphical representation in Fig. 3.1). Each trigger refines the decision made at the previous level and, when necessary, apply additional selection criteria. Starting from an initial bunch-crossing rate of 40MHz (interaction rate of ∼1GHz) , the rate of selected events must be reduced to ∼ 100 Hz for permanent storage.

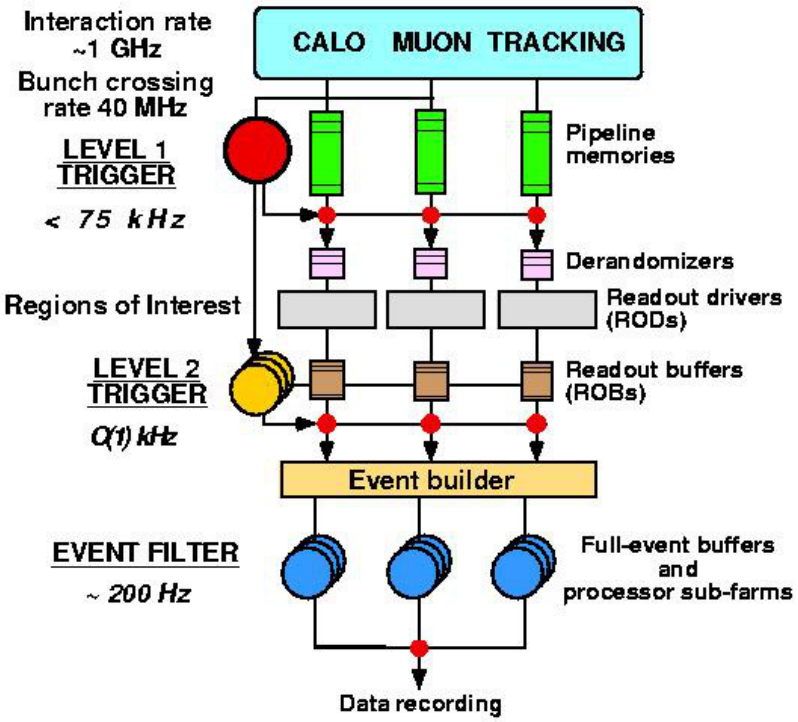

Figure 3.1: Overview of the ATLAS trigger system

3.1 Level 1 (LVL1)

The level 1 trigger (LVL1) makes an initial selection based on reduced-granularity information from a subset of detectors. High transverse-momentum muons are identified using only the trigger chambers (RPCs in the barrel, and TGCs in the end-caps). The calorimeter selections are based on reduced granularity information from all the calorimeters (EM and hadronic; barrel, end-cap and forward). Objects searched by the calorimeter trigger are high-p_T electrons and photons, jets, and τ-leptons decaying into hadrons, as well as large missing and total transverse energies. In the case of electron/photon and hadron/τ triggers, energy isolation cuts^{g}[1] can be applied. The maximum rate at which the ATLAS front-end systems can accept LVL1 triggers is limited to 75 kHz (up-gradable to 100 kHz).

3.2 Level 2 (LVL2)

The LVL2 trigger makes use of a "Region of Interest" (RoI) information provided by the LVL1 trigger. This include information on the position (η and ϕ^{g}) and p_T of candidate objects (high-p_T muons, electrons/γ,hadrons/τ,jets), and energy sums (E_T^{miss} vector and E_T value). The RoI data are sent by LVL1 and LVL2, for all the events selected by the LVL1 trigger. It is expected that LVL2 reduce the rate to $\sim$ 1 kHz. In contrast to the 75 kHz limit for LVL1

3.3 Level 3: Event Filter (EF)

After LVL2, the last stage of the selection is performed by the Event Filter (EF). It employs off-line algorithms and methods, adapted to the online environment, and use of most up to date calibration and alignment information and the magnetic field map. The EF will make the final selection of physics events which will be written to mass storage for subsequent full off-line analysis. The output rate from LVL2 should then be reduced by and order of magnitude, giving 100Hz, corresponding to and output data rate of $\sim$ 100 MB/s if the full event data are to be recorded. It is envisaged that the first task of the EF will be to confirm the results of the LVL2 decision and subsequently use the results of the LVL2 to seed its own analyses. The rejection power of the EF comes from:

[1] The terms with "g" refer to non-usual concepts and the definition can be found in the appendix M

1. Using refined algorithms and, when necessary, tighter p_T thresholds compared to those used in the LVL2

2. The availability of all data relevant to the specific event in calculations and selection criteria.

3. The use of complex algorithms and criteria which, due to processing time limits, cannot be performed at LVL2, an example being vertex and track fitting using bremsstrahlung recovery for electrons.

3.4 Data collected

The data used in this analysis were recorded between March and July in 2011, with the LHC operating at a center-of-mass energy of 7 TeV. The integrated luminosity is 1.04 fb^{-1} (Fig. 3.2), with an uncertainty of 3.7% [22]. Events are required to pass either a single electron or a single muon trigger, for the electron and muon channels respectively. The electron (muon) trigger threshold lies at E_T = 20 GeV (p_T=18 GeV). The trigger efficiencies reach the plateau region for lepton transverse momenta values substantially below the minimum analysis threshold of 40 GeV with typical trigger efficiencies for leptons selected for offline analysis of: 96% for electrons [23], 75% for muons with $|\eta|$ <1.05 and 88% for muon with 1.05< $|\eta|$ <2.0 [24]. The triggers used for this analysis are also mentioned later in section 7.2.

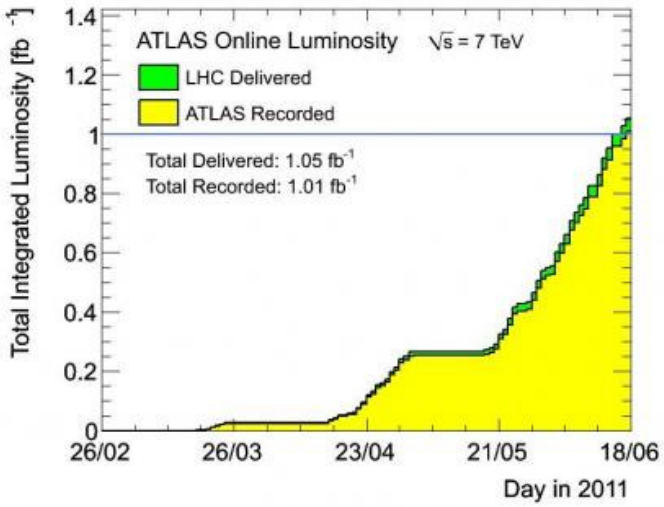

Figure 3.2: Integrated luminosity recorded during the first half of 2011, corresponding to $\int Ldt \sim 1 fb^{-1}$.

Chapter 4

Particle Identification and Reconstruction

Particles originated from the point of collision fly and leave electronic signals on the different sub-detectors (depending on the nature of each particle), such signals are later converted into physics quantities, this process is called reconstruction and the algorithms used for such purpose are reviewed in this chapter. Those algorithms make use of information from every sub-detector to reconstruct the different kind of particles (i.e. electrons, muons and jets) which are the main objects used for this search. Particle energy and position measurements are among the most important tasks of the reconstruction algorithms and its performance is crucial for the successful elaboration of any high energy particle analysis.

4.1 Electron Reconstruction and Identification

Physics channels of prime interest at the LHC are expected to produce electrons with p_T between a few GeV to 5 TeV. Good electron identification is therefore needed over a broad energy range. In the moderate p_T region (20-50 GeV), a jet-rejection factor exceeding 10^5 is needed to extract a relatively pure inclusive signal from genuine electrons above the residual background from jets faking electrons. The required rejection factor decreases rapidly with increasing p_T to $\sim 10^3$ for jets in the TeV region.

4.1.1 Reconstruction algorithms

At present, two electron reconstruction algorithms have been implemented in ATLAS offline reconstruction package (known as Athena, and described in App. B), both integrated into one single package and a common event data model.

- The standard one, which is seeded from the electromagnetic (EM) calorimeter, starts from clusters reconstructed in the calorimeter and then builds the identification variables based on information from the inner detectors (electron candidate tracks) and the EM calorimeters

- A second algorithm, which is seeded from the inner detector tracks, is optimized for electrons with energies as low as a few GeV, and selects good-quality tracks matching a relatively isolated deposition of energy in the EM calorimeters. The identification variables are then calculated in the same way as for the standard algorithm.

The standard algorithm is the one used to obtain the results presented in this thesis.

4.1.2 Electron Energy Calibration

The electron energy calibration [25] can be divide into three steps:

1. The Liquid Argon (LAr) calorimeter calibration converts the raw signal extracted from each cell in ADC counts into a deposited energy

2. Monte Carlo based calibration applied corrections at the cluster level for energy looses (dead material, leakage, etc....) using the calibration hits method and correction for energy modulation in η and ϕ (only for central electrons).

3. The in-situ calibration: calibration using physics events recorded by ATLAS detector determines the absolute energy scale and inter-calibrates the different region of the calorimeters.

Before the first collisions, the electromagnetic calorimeter energy scale has been derived from test beam results with an uncertainty of 3% in the central region, for the forward calorimeter the uncertainty on the energy scale is 5%, in this chapter will be discussed only the in-situ calibration done with the 2010 proton-proton collision events.

Electron energy can be calibrated thanks to the precise knowledge of the Z^0 mass from the LEP experiment (M_Z =91.1876±0.0021). The calibration strategy is two-fold: firstly we set the absolute energy scale and then equalize the energy response as a function of the electron position. The second goal is crucial in order to improve the electron energy resolution and decrease its constant term thanks to a better response uniformity.

With 2010 dataset, due to the limited statistics, the calibration can not be done both as a function of η^{clus} and ϕ^{clus}. The calibration is only perform as a function of η^{clus} since the non-uniformities as a function of ϕ^{clus} are expected to be much smaller thanks to the symmetry of the ATLAS detector. The total number of regions are 58. There are 50 regions for the central electrons ($|\eta| < 2.47$) and 8 for the forward electrons ($|\eta| > 2.5$).

Fitting procedure: The mass of the reconstructed $Z \to e^+e^-$ candidate is computed as:

$$M_Z = \sqrt{2E_1E_2(1 - cos(\theta_{12}))} \tag{4.1}$$

Where E_1 and E_2 are the energies of the two electrons measured by the calorimeter and θ_{12} is the angle between the electrons measured by the tracker. Here the energies are obtained after Monte-Carlo based energy scale corrections. Residual miss-calibration, in particular due to calorimeter inhomogenities, are parametrized in the following way for a given zone:

$$E^{meas} = E^{true}(1 + \alpha_i) \tag{4.2}$$

Where E^{meas} is the measured electron energy, E^{true} is the true electron energy and α_i represents the departure from a perfect calibration. Neglecting the second-order terms and supposing that the angle between the two electrons is perfectly known, the effect on the di-electron invariant mass is

$$M_{ij}^{meas} \backsimeq M_{ij}^{true}\left(1 + \frac{\alpha_i + \alpha_j}{2}\right) \tag{4.3}$$

where $0 < i, j < N_{regions}$, $N_{regions}$ is the number of regions considered for the calibration and N_{events} is the total number of selected events. An example of such procedure can be found in Fig. 4.1.

The fitting procedure was then applied to the full 2010 dataset reconstructed with ATLAS software release 16. The result of the fit can be found in Fig. 4.2. Since some energy scale corrections were already applied, the average η is close to 0 for the barrel ($|\eta| < 1.37$) and for the end-cap ($1.52<|\eta| < 2.47$) but residual non-uniformities are still observed. In the barrel (end-cap), the non-uniformities are of the order of $\pm 1\%$ (2%). For $|\eta| > 2.4$, deviations from 0 are much larger (from $\pm 5\%$). All these variations are not yet understood and are probably due to a combination of several effects like incorrect electronic calibration, incorrect high voltage correction in particular in the end-cap, extra-material in front of the calorimeter and presampler energy scale.

4.2 Muon Reconstruction and Identification

The ATLAS detector has been designed to provide clean and efficient muon identification and precise momentum measurement over a wide range of momentum and solid angle. The primary detector system built to achieve this is the muon spectrometer. The spectrometer covers the pseudo-rapidity range

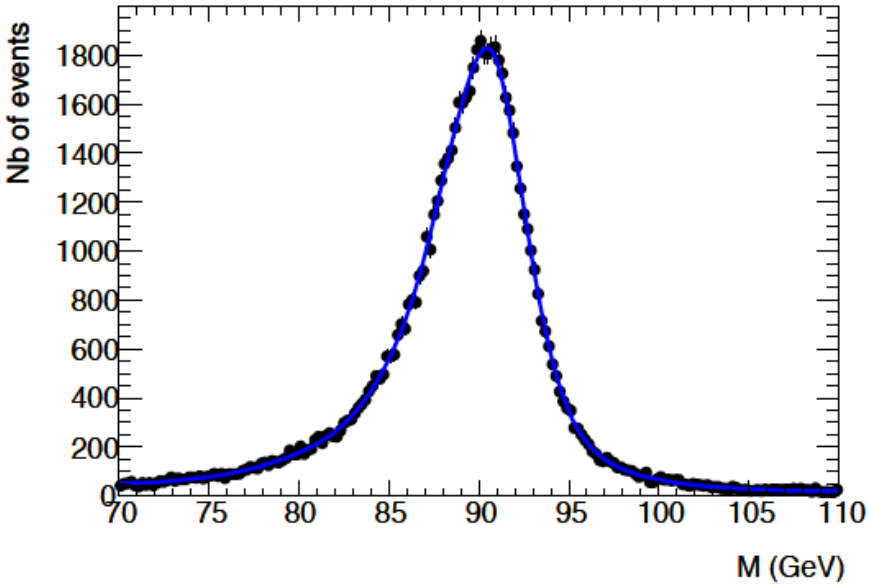

Figure 4.1: Di-electron invariant mass for $Z \rightarrow ee$ Monte Carlo sample.

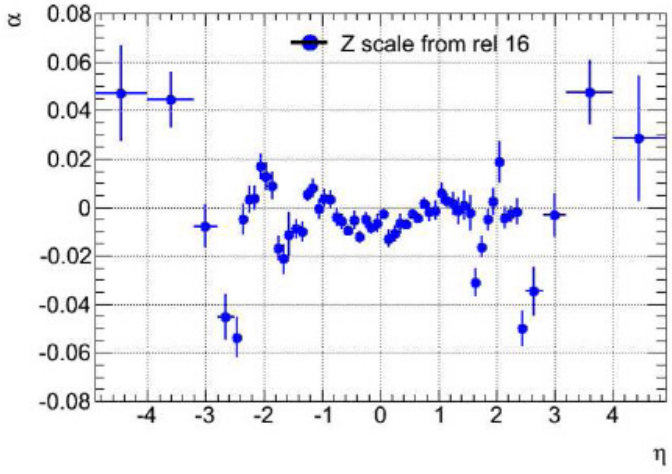

Figure 4.2: Distribution of α_{fit} for data

$|\eta|$ <2.7 and it allows identification of muons with momenta of about 3 GeV and precise determination of p_T up to about 1 TeV

4.2.1 Muon reconstruction algorithms

ATLAS employs a variety of strategies for identifying and reconstructing muons, The direct approach is to reconstruct standalone muons by finding tracks in the muon spectrometer and then extrapolating these to the beam line. Combined muons are ground by matching standalone muons to nearby inner detector track and then combining the measurements from the two systems. Tagged muons are ground by extrapolating inner detector tracks to the spectrometer detectors and searching for nearby hits. Calorimeter tagging algorithms are also being developed to tag inner detector tracks using the presence of a minimum ionizing signal in calorimeter cells.

- Standalone muons: First build track segments in each of the three muon stations and then link the segments to form tracks, The staco-family algorithm that finds the spectrometer tracks and extrapolates them to the beam line is called *Muonboy*. The extrapolation must account for both multiple scattering and energy loss in the calorimeter. Standalone algorithms have the advantage of slightly greater $|\eta|$ coverage-out to 2.7 compared to 2.5 for the inner detector, but there are holes in the coverage at $|\eta|$ near 0.0 and 1.2. Very low momentum muons (around few GeV) may be difficult to reconstruct because they don't penetrate to the outermost stations.

- Inner detector: Space points are identified in the pixel and micro-strip detectors, these points are linked to form track seeds in the inner four layers, and tracks are found by extending these seeds to add measurements from the outer layers. This strategy is expected to give very high detection efficiency over the full detector acceptance, $|\eta|$ <2.5.

- Combined muons: Both of the muon combination algorithms, *Staco* and *Muid*, pair muon-spectrometer tracks with inner detector tracks to identify combined muons. The match chi-square, defined as the difference between other and inner track vectors weighted by their combined co-variance matrix:

$$\chi^2_{match} = (T_{MS} - T_{ID})^T (C_{ID} + C_{MS})^{-1} (T_{MS} - T_{ID}) \qquad (4.4)$$

  Provides and important measure of the quality of this match and is used to decide which pairs are retained. Here T denotes a vector of

(five) track parameters expressed at the point of closest approach to the beam line and C is its co-variant matrix, The subscript ID refers to the inner detector and MS to the muon spectrometer (after extrapolation accounting for energy loss and multiple scattering in the calorimeter).

The combined muon algorithm is the one used in the analysis.

4.2.2 Muon momentum resolution

The momentum resolution [26] is extracted from the width of the di-muon mass distribution in $Z^0 \rightarrow \mu^+\mu^-$ decays and the comparison of two independent measurements of muons from $Z^0 \rightarrow \mu^+\mu^-$ and $W \rightarrow \mu^{\pm}\nu_{mu}$ decays provided by the two ATLAS tracking systems, the Inner Detector and Muon Spectrometer.

The Muon spectrometer is optimized to provide a momentum measurement with a relative resolution designed to be better than 3% over a wide p_T range and 10% at p_T=1 TeV.

The relative resolution on the measurement $\sigma(p)/p$ is dictated by different effects related to the amount of material that the muon traverses, the spatial resolution track points and the degree of internal alignment of the two subsystems. For a given value of $|\eta|$ the resolution can be parametrized as a function of p_T in the following way

$$\frac{\sigma(p)}{p} = \frac{p_0^{MS}}{p_T} \otimes p_1^{MS} \otimes p_2^{MS}.p_T \tag{4.5}$$

where the p_0^{MS}, p_1^{MS} and p_2^{MS} are coefficients related to the energy loss in the calorimeters material, multiple scattering and intrinsic resolution terms. For the ID a similar parametrization can be found. In this case the curvature measurement depends on the track length of the muon in the active material, which is reduced to the edge of the TRT fiducial volume. This translate into a uniform response in the central part and a rapidly worsening resolution beyond this region. The following approximate parametrization of the resolution is used:

$$\frac{\sigma(p)}{p} = \frac{p_1^{ID}}{p_T} \otimes p_2^{ID} p_T \tag{4.6}$$

The parametrized resolution as a function of p_T for the four $|\eta|$ regions, obtained using the values of the parameters form the combined fits, are shown separately in Fig. 4.3 and 4.4 for the MS and ID, respectively.

Correction formula for combined muons: The combined muon momentum measurement is determined by the relative weights of the ID and MS momentum measurements in the track fit. Due to the large amount of the calorimeter

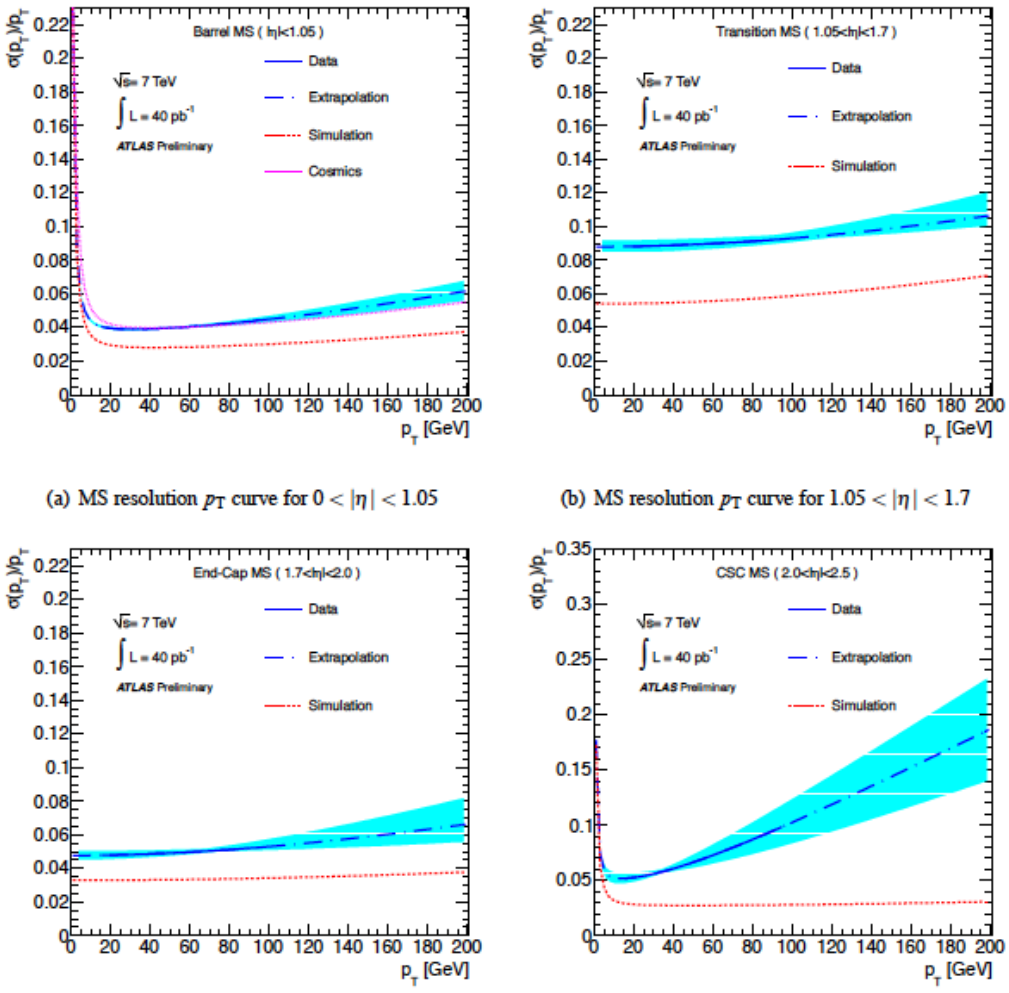

(a) MS resolution p_T curve for $0 < |\eta| < 1.05$

(b) MS resolution p_T curve for $1.05 < |\eta| < 1.7$

Figure 4.3: Resolution curve form the fitted parameter values of the MS in collision data and simulation as a function of the muon p_T, for the different $|\eta|$ regions of the detector. The solid blue line shows determinations based on data and is continued as dashed line or the extrapolation to p_T ranges not accessible. The shaded band represents the sum in quadrature of the statistical and systematic uncertainties. For the case of the barrel, a comparison with the curve obtained from the fitted parameters from cosmic ray data is overlaided for comparison.

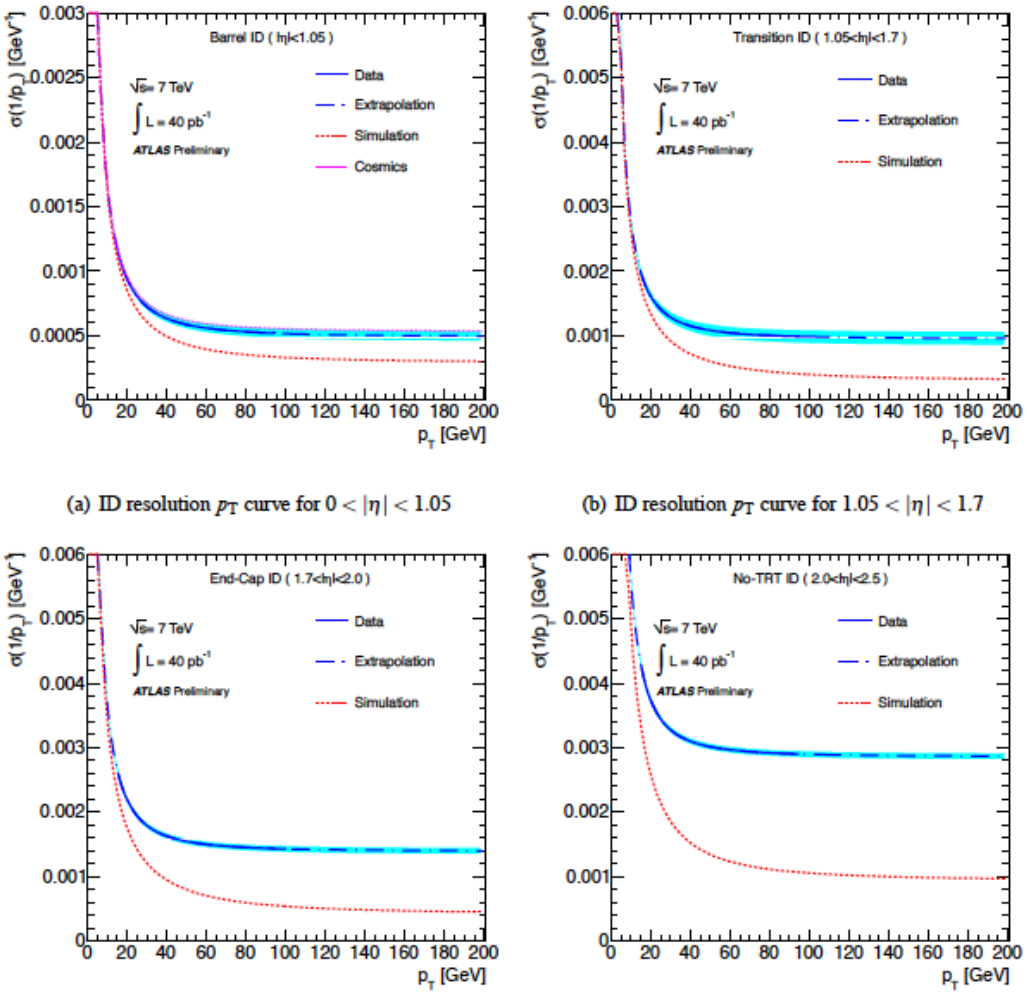

(a) ID resolution p_T curve for $0 < |\eta| < 1.05$

(b) ID resolution p_T curve for $1.05 < |\eta| < 1.7$

Figure 4.4: Resolution curve on the curvature, $\sigma(1/p_T)$, from the fitted parameter values of the ID in collision data and simulation as a function of the muon p_T for different $|\eta|$ regions. The solid blue line shows measurements on data and is continued as dashed line for the extrapolation to p_T ranges not accessible in this analysis. The shaded band represents the sum in quadrature of the statistical and systematic uncertainties.

material between ID and MS, the two measurements can be treated as uncorrelated. Therefore, starting from the corrected ID and MS p_T measurements in Monte Carlo, we can correct the combine muon p_T(CB) in the simulation and obtain a new measurement, $p_T^{'}$(CB). The new Monte Carlo measurement is the linear combination of the MS and ID contributions, weighted by the MS and ID resolutions.

$$p_T^{'}(CB) = p_T(CB)\left[1 + \frac{\frac{\Delta(MS)}{\sigma^2(MS)} + \frac{\Delta(ID)}{\sigma^2(ID)}}{\frac{1}{\sigma^2(MS)} + \frac{1}{\sigma^2(ID)}}\right] \tag{4.7}$$

4.2.3 Muon Momentum resolution at high-p_T

Muons coming from Black Hole decay are expected to have very high-p_T values. To ensure precise measurement of the momentum, muons are required to have hits in all three muon layers and are restricted to those η-ranges where the muon spectrometer alignment is best understood [27]: approximately η<1.0 and 1.3<$|\eta|$<2.0. The average momentum resolution is currently about 15% at p_T =1 TeV. About 80% of the muons in these η-ranges are reconstructed, with most of the loss coming from regions with limited detector coverage.

4.3 Reconstruction and Identification of Jets

High quality and highly jet reconstruction is an important tool for almost all physics analyses to be performed with the ATLAS experiment. Typically, an absolute systematic uncertainty of better than 1% is desirable for precision physics like the measurement of the top quark mass, and the reconstruction of some SUSY final states. The principal detector for jet reconstruction is the ATLAS calorimeter, with its basic components as described in 2.2.2. It provides near hermetic coverage in the pseudo-rapidity range $|\eta|$ <4.9.

4.3.1 Jet reconstruction algorithms

In data and Monte Carlo simulations among the different jet reconstruction algorithms the one that gives better performance and that was chosen as the main one for most of the physics analysis in ATLAS is the *antikt* algorithm [28].

4.3.2 Jet Energy Scale

Hadronic jets used for ATLAS physics analysis are reconstructed by a jet algorithm starting from the energy deposition of electromagnetic and hadronic

showers in the calorimeters. An example of a jet recorded by the ATLAS detector and displayed in the plane transverse to the beam line is shown in Fig. 4.5

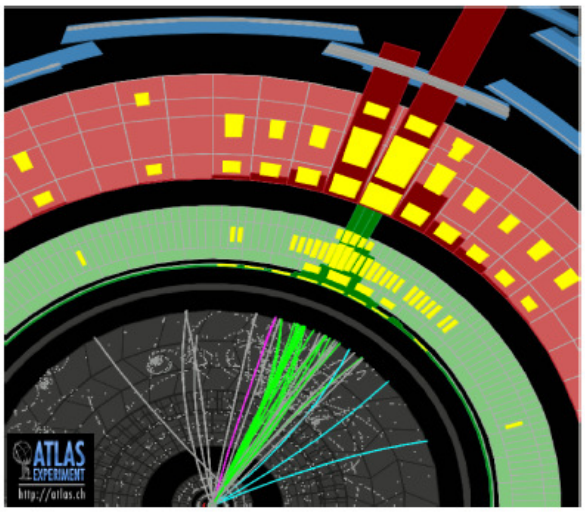

Figure 4.5: Zoom of a x-y view of the ATLAS detector showing one of the high-p_T jets of the event show in one event. The energy deposition in the calorimeters cells are displayed as light rectangles. The size of the rectangles is proportional to the energy deposits. The dark histograms attached to the LAr (Tile) Calorimeters illustrates the amount of deposited energy. The line in the ID display the reconstructed tracks originating from the interaction vertex.

The jet Lorentz four-momentum is reconstructed from the corrected energy and angles with respect to the primary event vertex. The jet energy calibration [29] relates the jet energy measured with the ATLAS calorimeter to the true energy of the corresponding jet of stable particles entering the ATLAS detector. The jet calibration corrects for the following detector effects that affect the jet energy measurements.

1. **Calorimeter non-compensation**: partial measurement of the energy deposited by hadrons.

2. **Dead material**: energy looses in inactive regions of the detector.

3. **Leakage**: energy of particles reaching outside the calorimeters.

4. **Out of calorimeter jet cone**: energy of deposits of particles inside the jet formed from stable particles entering the detector that are not included in the reconstructed jet.

5. **Noise threshold and particle reconstruction efficiency**: signal losses in the calorimeter clustering and jet reconstruction.

Jets reconstructed in the calorimeter system are formed from calorimeter energy depositions reconstructed at the electromagnetic energy scale (EM) or from energy depositions that are corrected for the lower detector response to hadrons. The EM scale correctly reconstructs the energy deposited by particles in an electromagnetic shower in the calorimeter. This energy scale is established using test-beam measurements for electrons in the barrel and the end-cap Calorimeters. The absolute calorimeter response to energy deposited via electromagnetic processes was validated in the hadronic calorimeter using muons, both from test-beams and produced in situ by cosmic rays. The energy scale of the electromagnetic calorimeters is corrected using the invariant mass of Z bosons produced in proton-proton collisions (Z$\rightarrow$ e^+e^- events). The correction for the lower response to hadrons is solely based on the topology of the energy depositions observed in the calorimeter. In the simplest case the measured jet energy is corrected, on average, using Monte Carlo simulations, as follows:

The variable Ejet is the calorimeter energy measured at the EM jet electromagnetic scale, Ecalib is the calibrated jet energy and Fcalib is the calibration function that depends on the measured jet energy and is evaluated in small jet pseudo-rapidity regions. The variable O(NPV) denotes the correction for additional energy from multiple proton-proton interactions depending on the number primary vertices. The simplest calibration scheme (called EM+JES) applies the JES corrections to jets reconstructed at the electromagnetic scale. This calibration scheme allows a simple evaluation of the systematic uncertainty from single hadron response measurements and systematic Monte Carlo variations. This can be achieved with small data sets and is therefore suitable for early physics analyses. Other calibration schemes use additional cluster-by-cluster and/or jet-by-jet information to reduce some of the sources of fluctuations in the jet energy response, thereby improving the jet energy resolution. For these calibration schemes the same jet calibration procedure is applied as for the EM+JES calibration scheme, but the energy corrections are numerically smaller. The global calorimeter cell weighting (GCW) calibration exploits the observation that electromagnetic showers in the calorimeter leave more compact energy depositions than hadronic showers with the same energy. Energy corrections are derived for each calorimeter cell within a jet, with

the constraint that the jet energy resolution is minimized. The cell corrections account for all energy losses of a jet in the ATLAS detector. Since these corrections are only applicable to jets and not to energy depositions in general, they are called "global" corrections. The local cluster weighting (LCW) calibration method first clusters together topologically connected calorimeter cells and classifies these clusters as either electromagnetic or hadronic. Based on this classification energy corrections are derived from single pion Monte Carlo simulations. Dedicated corrections are derived for the effects of non-compensation, signal losses due to noise threshold effects, and energy lost in non-instrumented regions. They are applied to calorimeter clusters and are defined without reference to a jet definition. They are therefore called "local" corrections. Jets are then built from these calibrated clusters using the $anti - kt$ jet algorithm. The final jet energy calibration can be applied to EM scale jets, with the resulting calibrated jets referred to as EM+JES, or to GCW and LCW calibrated jets, with resulting jets referred to as GCW+JES and LCW+JES jets. A further jet calibration scheme, called Global Sequential (GS) calibration, starts from jets calibrated with the EM+JES calibration and exploits the topology of the energy deposits in the calorimeter to characterize fluctuations in the jet particle content of the hadronic shower development. Correcting for such fluctuations can improve the jet energy resolution. The corrections are applied such that the mean jet energy is left unchanged. The correction uses several jet properties and each correction is applied sequentially. In particular, the longitudinal and transverse structure of the hadronic shower in the calorimeter is exploited. The simple EM+JES jet calibration scheme does not provide the best performance, but allows in the central detector region the most direct evaluation of the systematic uncertainties from the calorimeter response to single isolated hadron measured in situ and in test-beams and from systematic variations of the Monte Carlo simulation. For the GS the systematic uncertainty is obtained by studying the response after applying the GS calibration with respect to the EM+JES calibration. For the GCW+JES and LCW+JES calibration schemes the JES uncertainty is determined from in situ techniques. For all calibration schemes the JES uncertainty in the forward detector regions is derived from the uncertainty in the central region using the transverse momentum balance in events where only two jets are produced.

4.4 Missing Transverse Energy

Neutrino interaction with matter is very small its presence is inferred by the missing energy [30] (E_T^{miss}) computation. Events with large E_T^{miss} are ex-

pected to be the key signature for new physics such as super-symmetry and extra dimensions. A good E_T^{miss} measurement in terms of linearity and resolution is also important for the reconstruction of the top-quark mass from $t\bar{t}$ events with one top quark decaying semileptonically. The calorimeter plays a crucial role in the E_T^{miss} measurement and an important first step of the E_T^{miss} is the suppression of noise in the calorimeter. Two E_T^{miss} reconstruction algorithms are used in ATLAS (Cell-base and Object-based).

E_T^{miss} is not treated as an object in this analysis, the decay of black hole could include neutrinos but the proportion compared with leptons and jets is quite small, although E_T^{miss} is used to separate the different kind of background (i.e. low E_T^{miss} value cut is used to select a pure sample of QCD multi-jet events as described in section 8.1.).

Chapter 5

Monte Carlo simulation

Monte Carlo (MC) simulated event samples are used to develop and validate the analysis procedure, to help to estimate the Standard Model backgrounds and to investigate the signal models.

The simulated background and signal samples are listed along with their process cross-section and reconstruction tag in Appendix A

5.1 Background Samples

5.1.1 QCD Samples

Two sets of QCD (multi-jets) simulated samples are used in estimating the QCD background. One set of samples is generated using alpgen 2.13 [33] interfaced to herwig 6.510 [35] and jimmy 4.1 [36]. `CTEQ6L1` PDFs are used for alpgen. Exclusive samples with two to five partons, and inclusive samples with six or more partons are used. In each sample with a given number of partons, the sample is divided to slices according to the leading parton p_{T}. Dedicated alpgen samples for $\mathrm{b\bar{b}}$ are also used. These have the same structure as the nominal samples, in that they are divided into different slices with leading b-jet p_{T}.

Another set of QCD samples are generated with pythia 6.4.24 [31], and divided into nine unfiltered samples with different jet-p_{T} cutoffs. pythia uses the `MRST2007` PDFs

5.1.2 W/Z+Jets Samples

The W+jets and Z+jets samples are generated using alpgen interfaced to herwig and jimmy. Exclusive samples with zero to four additional partons and an inclusive sample with five or more additional partons are used. The cross-sections are computed using the alpgen cross-sections scaled so that the sum of the exclusive sample cross-sections equal the inclusive cross-section, while retaining the exclusive relative yields predicted by alpgen. The inclusive NNLO cross-section times branching fraction to a single lepton species are $\sigma(W \to \ell\nu) = 10.46 \pm 4$ nb and $\sigma(Z \to \ell\ell) = 1.0969 \pm 4$ nb. There are also

$W+bb$ and $Z+bb$ alpgen samples that are added to the nominal alpgen W+jets and Z+jets samples as a cross-check; the cross-sections for these samples are taken from alpgen. The addition of the extra $Z + bb$ and $W + bb$ samples to the nominal sample overestimates the amount of heavy flavour associated with W/Z+jets production. Unfortunately, the sample without this heavy flavour underestimates this component. Therefore, we separately measure the background with and without the additional heavy flavour, and use the difference as a systematic uncertainty.

For systematic studies, we also make use of samples generated with sherpa [34] documented by the top quark analysis group in ATLAS.

5.1.3 $t\bar{t}$ Samples

A possible $t\bar{t}$ background was simulated using a suite of Monte Carlo generators with MC@NLO 3.41 [32] to generate matrix elements, jimmy to describe the multiple parton interactions, and herwig to describe the remaining underlying event and parton showers. `CTEQ6.6` PDFs are used. The top mass is set to 172.5 GeV. In this sample, 11.3% of the events have negative weight, and this is taken into account when calculating the luminosity of the samples.

5.1.4 Single Top Samples

Single top samples corresponding to three production modes, s-channel, t-channel and Wt-channel, have been generated separately; the first two of which are separated again into the three different lepton decay modes. The MC@NLO cross-sections are used and all k-factors are set to unity. The samples are generated with MC@NLO with herwig and jimmy using `CTEQ6.6` PDFs.

5.1.5 Di-Boson Samples

The di-boson samples are generated with herwig. The samples have been filtered to contain one lepton with $p_{\mathrm{T}} > 10$ GeV and $|\eta| < 2.8$. The k-factors are taken as the ratio of the MC@NLO cross-section with `MSRW2008` PDF to the alpgen plus herwig cross-section.

5.2 Signal Samples

5.2.1 CHARYBDIS Samples

Charybdis2 1.0.2 [37] is used to generate the String Ball and Black hole Monte Carlo signal events. The shower evolution and hadronization are simulated with pythia. `CTEQ6.6` is used for the PDFs.

Charybdis can model final remnant decays in two different ways. When the Black Hole mass falls below the Planck scale, a two-body phase space decay (low multiplicity remnant) occurs, or the number of final-state particles is chosen from a Poisson distributed with mean of four (high multiplicity remnant).

Most of the Charybdis parameters are set to their default values. The following model parameters have been changed from the defaults.

- YRCSEC = FALSE: In all cases, do not use Yoshino-Rychkov factors in the cross-section.
- BHSPIN = TRUE/FALSE: Rotating Black Holes or String Balls, or not.
- MJLOST = TRUE/FALSE. Turn on or off initial-state graviton radiation.
- NBODY = 2 or 4: Two or four body decay of remnant.
- NBODYVAR = TRUE/FALSE: Variable (Poisson distributed) N-body decay, or fixed N-body decay of remnant.

A set of parameter-scan samples are produced, where for each model the following are varied:

- TOTDIM: Total number of dimensions.
- MINMSS: Minimum production mass, M_{TH}.
- MPLNCK: Planck scale, M_D.
- DGMS: String scale, M_S, if String Balls (DGSB = TRUE).

The String-Ball samples all have the number of extra dimensions set to six and the string coupling set to 0.4.

Two baseline signal samples are used to guide the analysis. Neither sample produces gravitons in the event. One sample is ID 113009: non-rotating Black Holes that decay by conserving baryon number; number of extra dimensions is six; M_D set to 0.8 TeV; and M_{TH} set to 4 TeV. The other sample is ID

113039: rotating string balls that do not conserve lepton number in decay; number of extra dimensions is six; string and Planck scales set to 1 TeV and 1.26 TeV, respectively; string coupling set to 0.4; and M_{TH} set to 3 TeV.

5.2.2 BlackMax Samples

Blackmax 2.01 [38] is also used to generate alternative black hole signal events. The shower evolution and hadronization are simulated with pythia 6.421. `CTEQ6.6` is used for the PDFs. Most of the BlackMax parameters are set to their default values. The following model parameters have been changed from the defaults.

- number_of_conservations = 0 or 3: Lepton number is conserved, or not.
- turn_on_graviton = 0: No gravitons in simulation.
- size_of_brane(1/Mpl) = 0.0: No brane thickness.
- extra-dimension_size(1/Mpl) = 0.0: Infinite size of extra dimensions.
- Choose_a_case = tensionless_nonrotating/rotating_nonsplit: Rotating Black Holes, or not.

When performing the parameter scans, the following parameters were varied or changed.

- number_of_extra_dimensions: Number of extra dimensions.
- Minimum_mass(GeV): Minimum production mass, M_{TH}.
- M_pl(GeV): Planck scale, M_D.

Chapter 6

Systematics

Every analysis is affected by different systematics according to the particles and properties that are measured, in our case the most important systematics are related to the accurate measurement of the energy of leptons and Jets, another important source is the Monte Carlo description of the data and the uncertainty due to the limited statistic in MC, in the following sections those uncertainties are discussed.

6.1 Jet Energy Scale/Resolution

6.1.1 Jet Energy Scale (JES) Uncertainty

The total jet energy scale uncertainty is derived by considering all the individual components. In the central region ($|\eta| < 0.8$), the estimate proceeds as follows.

- For each p_T^{jet} and $|\eta|$ bin, the uncertainty due to the calibration procedure is calculated. For each bin, the maximum deviation from unity between the energy and p_T response is taken as the final non-closure uncertainty.
- The calorimeter response uncertainty is estimated as a function of $|\eta|$ and p_T from the propagation of single particle uncertainty to the jets.
- Sources of uncertainties estimated using MC samples with a systematic variation are accounted as follow: (a) the response in test sample R_{var} and the response in the nominal sample R_{nom} is considered as a starting point for the estimate of the JES uncertainty. The deviation of this ratio from unity is defined as:

$$\Delta_{JES}(p_T^{jet}, |\eta|) = \left| 1 - \frac{R_{var}(p_T^{jet}, |\eta|)}{R_{nom}(p_T^{jet}, |\eta|)} \right| \tag{6.1}$$

  This deviation is calculated from both the energy and p_T response, leading to $\Delta^{E}_{JES}(p_T^{jet}, |\eta|)$ for the deviation in energy response, and to $\Delta^{p_T}_{JES}(p_T^{jet}, |\eta|)$ for the deviation in the transverse momentum response.

(b) The larger Δ_{JES} in each bin derived form the jet energy or transverse momentum response is considered as the contribution to the final JES systematic uncertainty due to the specific effect:

$$\Delta_{JES}(p_T^{jet}, |\eta|) = max(\Delta^{E}_{JES}(p_T^{jet}, |\eta|), \Delta^{p_T}_{JES}(p_T^{jet}, |\eta|)) \tag{6.2}$$

- The estimate of the uncertainty contribution due to additional material in the inner detector and overall additional dead material are estimated as well. These uncertainties are then scaled by the average fraction of particles forming the jet that have $p < 20$ GeV (for the inner detector distorted geometry) and by the average fraction of particles outside the kinematic range of the single hadron response in-situ measurements (for the overall distorted geometry) For each (p_T^{jet},$|\eta|$)-bin, the uncertainty contribution from the calorimeter, the jet calibration non-closure, and systematic Monte Carlo simulation variations are added in quadrature.

  For pseudo-rapidities beyond $|\eta| > 0.8$, the η-intercalibration contribution is estimated for each pseudo-rapidity bin in the endcap region The pseudo-rapidity intercalibration contribution is added in quadrature to the total JES uncertainty determined in the $0.3 \leq |\eta| \leq 0.8$ region to estimate the JES uncertainty from jets with $|\eta| > 0.8$, with the exception of the non-closure term that is taken from the specific η-region. For low p_T^{jet}, this choice leads to partially double counting the contribution from dead material uncertainty, but it is considered as a conservative estimate in a region where it is difficult to estimate accuracy of the material description. The contribution to the uncertainty due to additional proton-proton interactions (pileup[1]) is added separately depending on the number of primary vertices in the event.

  Fig. 6.1 shows the final fractional jet energy scale systematic uncertainty and its individual contributions as a function of p_T^{jet} for the three selected $|\eta|$ regions, The fractional JES uncertainty in the central region amounts to 2% to 4% for p_T^{jet} <60 GeV, and it is between 2% and 2.5% for $60 \leq p_T^{jet} \leq 800$ GeV. For jets with $p_T^{jet} > 800$ GeV, the uncertainty ranges from 2.5% to 4%. The uncertainty amounts to up to 7% and 3% respectively, for the $p_T^{jet} < 60$ GeV and p_T^{jet} >60 GeV in the endcap region, a 13% uncertainty is assigned for p_T^{jet}=20 GeV. The increase in the uncertainty is dominated by the modeling of the soft physics in the forward region that is accounted for in the η-intercalibration contribution. This uncertainty contribution is estimated conservatively.

[1] Additional soft proton-proton collisions that occur simultaneously with any hard interaction in high luminosity runs

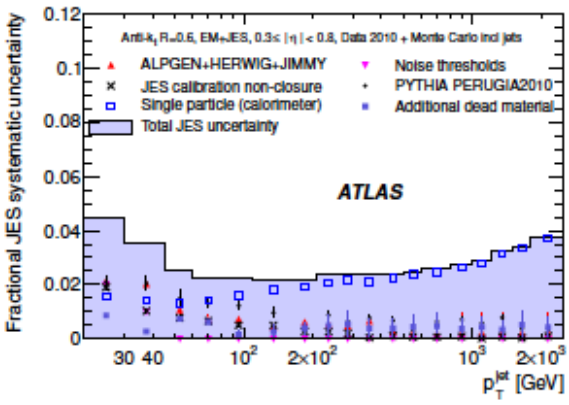

(a) $0.3 \leq |\eta| < 0.8$

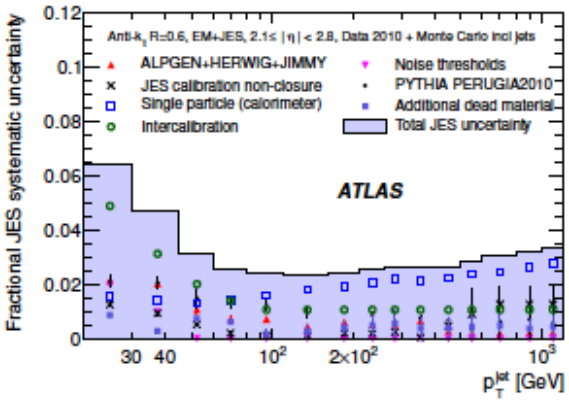

(b) $2.1 \leq |\eta| < 2.8$

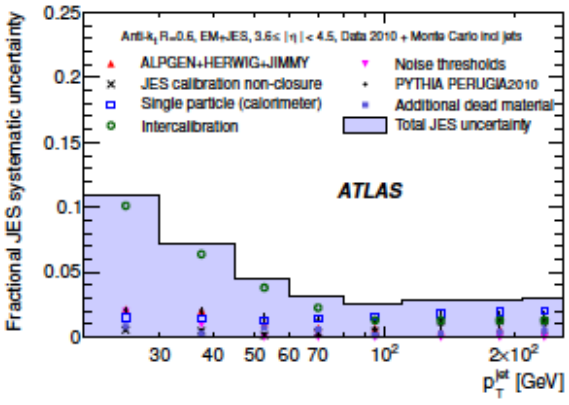

(c) $3.6 \leq |\eta| < 4.5$

Figure 6.1: Fractional jet energy scale systematic uncertainty as a function of p_T^{jet} for jets in the pseudo-rapidity region $0.3 \leq |\eta| \leq 0.8$ in the calorimeter barrel (a), $2.1 \leq |\eta| \leq 2.8$ in the calorimeter endcap (b), and in the forward pseudo-rapidity region $3.6 \leq |\eta| \leq 4.5$. The total uncertainty is shown as the solid light shaded area. The individual sources are also shown together with the uncertainties from the fitting procedure if applicable.

6.1.2 Jet Energy Resolution (JER)

Once the correct jet energy scale is set as described in 4.3.2, another effect to look at is the energy resolution, this is modeled by a simple Gaussian distribution as a function of jet p_T for every event the jet energy is smeared according to that distribution and the effect on the final result is obtaining comparing to the nominal value.

6.2 Lepton Energy Scale/Resolution

Electrons and Muons energy and/or resolution are obtained as described in 4.1.2 uncertainties are managed through official software tools, once the correct nominal value is chosen the uncertainties are computed varying that central according to the p_T and $|\eta|$ position of the electron or muon, then the new value is propagated through the analysis and the impact is calculated as the difference with respect to the nominal values.

6.3 Monte Carlo Generator

Monte Carlo modelling uncertainties are assesed using alternative samples produced with different generators (for the $Z + jets$ and $W + jets$ and $t\bar{t}$ backgrounds), in case of QCD multi-jets background this systematic is not studied since the rate prediction is done purely with collision data as described in section 8.1. The default generators in the analysis are `Alpgen` for $Z + jets$ and $W + jets$ processes and `MC@NLO` for $t\bar{t}$, the generator used for comparison is `sherpa`.

6.4 Initial and Final State Radiation

In every process that contains coloured and/or changed objects in the initial or final state, gluon and/or photon radiation may give large corrections to the overall topology of the events. Starting from a basic 2→2 process, this kind of corrections will generate 2→3, 2→4, and so on, final-state topologies. As the variable energies are increased, hard emission of this kind is increasingly important, relative to fragmentation, in determining the event structure.

This systematic is studied for Top pair production, by changing up/down the initial and final state radiation as described in App. H, and its magnitude is presented when looking at the combined $W+jets$ and $t\bar{t}$ background described in section 8.3.

6.5 Total Uncertainty

The total systematic uncertainty is constructed adding in quadrature every individual component (assuming they are not correlated or they are weakly correlated). For the total uncertainty the statistical and systematic components are added in quadrature and is represented as a yellow band in every plot in the following sections as in Fig. 7.1.

Chapter 7

Particle and Event Selection

In chapter 4 was reviewed how the reconstruction algorithms work to identify and measure properties of elementary particles like electrons, muons and jets, in addition to those requirements every analysis need a set of cuts to select only the interesting events, for instance a Black Hole event is expected to produce high energy particles, therefore a cut on the energy of the final state particles is applied and helps to reduce the rate of non-interesting low energy processes, another set of event variables help us to exclude events that were produced for example by a cosmic ray (which leaves high energy depositions on the calorimeters) and reconstructed as a jet (fake-jet) or fake jets reconstructed from electronic failures on the calorimeters, etc. This chapter motivates our particle and event selection, and for the first time introduces the definition of the signal and control regions crucial part of the analysis.

7.1 Object (Particle) selection

In order to assure the optimal performance in terms of particle reconstruction and identification, the final state particles (leptons and jets) are selected following the recommendations from the different performance groups (e/γ, Combined Muons and Jet/Etmiss) in the ATLAS collaboration, such groups are in charge of deliver the latest recommendations for the reconstruction of the various final state particles: muons, electrons and jets (many of those recommendations are already incorporated in the reconstructions algorithms discussed in chapter 4), although some of the cuts are analysis dependent and mostly motivated by the kind of signal is searched. The following cuts below are the criteria used to select our objects.

7.1.1 Electron selection

Electrons are selected according to the following cuts:

- $|\eta| < 2.47$
- $E_T > 40$ GeV

- $\frac{E_T cone20}{E_T} < 0.1$ (Isolation, the energy deposited in a cone around the electron direction should be less than the 10% of the electron energy).
- Tight ID (Based on EM shower shapes criteria)

7.1.2 Muon selection

Muons are selected according to the following cuts:

- $|\eta|$ <1 and 1.3< $|\eta|$ <2.0
- Requiring hits on the three muon spectrometer layers
- p_T >40 GeV
- Combined muons (Reconstruction algorithm)
- $\frac{p_T cone30}{p_T} < 0.05$ (Isolation, the sum of transverse momentum in a cone around the muon direction should be less than the 5% of the muon transverse momentum)

7.1.3 Jet selection

Jets are selected according to the following cuts:

- $|\eta| < 2.8$
- $E_T > 40$ GeV
- Loose Jet cleaning (Definition in App. D)

7.1.4 Overlap removal

After the selection of electrons, muons and Jets a further requirement is applied requiring that the reconstructed Jet direction don't overlap with the direction of electrons or muons in certain range.

7.2 Event Selection

As discussed previously (Chapter 3) ATLAS records events based on complicated trigger decisions at three levels, furthermore every event contains additional information as a flag, for example the event is categorized as "good" or "bad" depending on the number of sub-detectors that were activated and working 100% at the moment of the event recording, these and more requirements are the ones used for this analysis and are described below:

- **GRL (Good Run List)**: File containing information of every run like the run number (number identifying every run) and luminosity block (chunk of events in certain time interval, smallest unity of events recorded in a run), such file is created according the information on how many sub-detectors were activated at the time the event was recorded. According to every particular analysis the event can be accepted or rejected, (i.e. in an analysis using muons, if the toroidal magnet was off at that instant, the momentum of the muons cannot be measured accurately, in that case the event is considered bad for that specific analysis and is rejected)

- **Trigger**: This cut is also analysis dependent and as pointed out before it is very important tool in order to reduce the rate of events to analyze. In this analysis the events are separated in electron and muon channels as we will see later this is done using the trigger and the flavor of the leading lepton in the event, in case of the electron channel the trigger item used is EF_e20_medium (Event Filter level with a threshold of 20 GeV in energy) in the case of the muon channel and OR is used between EF_mu18 (Event Filter level with a threshold of 18 GeV) and EF_mu40 (this due to a trigger bug at high-p_T the later trigger allow us to recover efficiency at high p_T region).

- **Vertex cut**: To remove non-collision or cosmic events, the first reconstructed primary vertex in the event is required to have at least five tracks associated with it. Events not satisfying this requirement are rejected.

- **Jet cleaning** (loose definition, see App. D): To avoid cosmic-ray events or bad calorimeter noise, we follow the recommended procedure of how to clean jets form detector effects. The procedure is applied for any jet with $p_T \geq 20$ GeV.

- **Liquid Argon Error (LArError)**: cut applied to reject bad quality clusters or fake clusters originating from calorimeter problems. We remove LAr noise burst (from data only, not MC) by requiring special flag (larerror=0), which vetoes noise burst events as well as those with a data integrity error, specially important for electron identification

- **Cosmic veto**: To avoid the inclusion of collision events with an overlayed cosmic event, events are vetoed in which there are one or more selected muons (after ΔR-based jet muon overlap removal) that satisfy the following conditions:

  - $p_T > 20$ GeV
  - $|z_0| > 1$ mm
  - $|d_0| > 0.2$ mm

- **Number of Leptons in the events (numLep) >0**: Only events with leptons are selected
- **Leading lepton (e/μ)**: To separate our events in Electron and Muon channels according to the flavor of the lepton with the biggest transverse momentum value in the event.
- **LArhole veto**: Due to electronic problems in the LAr Calorimeter a region was affected, every jet reconstructed in such region is considered bad jet so the events with such kind of jets are rejected.
- **Tight Electron**: Applied just for the electron channel. The leading electron should have a tight identification requirement based on the shower shape variables.
- **numObj≥3**: This is a multi-object search therefore at least three objects in the events (lepton and/or jets) are required

7.3 $\sum p_T$ variable

To separate the Standard Model background from our Black Hole signal an event variable called sumPt is used, this variable is constructed adding the transverse momentum of the selected final state particles (lepton and jets) passing the requirements in section 7.1 and mathematically is expressed as in equation 7.1

$$SumPt = \sum p_T = \sum_{i=0}^{i=N_P} p_{T_i} \tag{7.1}$$

Where N_p are the number of final state particles (i.e. N_p=3 for an event with one lepton and two jets).

7.4 Control and Signal region

After the last cut (numObj>=3) described in section 7.2 the remaining events are splitted in the so-called control and signal regions using the $\sum p_T$ cut as the main discriminant variable.

- Control Region: 300<$\sum p_T$ <700 GeV
- Signal Region: $\sum p_T$ >700 GeV

The control region is a region enriched with the different kind of backgrounds ($W + jets$,$Z + jets$,$t\bar{t}$,QCD) and with enough statistic to study all of them, in the control region the assumption is that there is no signal events in there, or at least the number of signal events is very small (calculated by using MC simulation), from the control region the different backgrounds are extrapolated to the signal region in a process known as background estimation as described in chapter 8.

7.5 Observed and expected events for $\int Ldt = 1.04 fb^{-1}$

The cut-flow table with observed events in proton collision data after each cut described in section 7.2 is presented in table 7.1, the events are separated in electron and muon channel. In case of expected events for Monte Carlo simulated background and signals the numbers are presented in tables 7.2 and 7.3 (for electron and muon channels), note that for Monte Carlo simulation the comparison with "real" data make sense just after the trigger cut, previous cuts are just meant to be applied to the "real" data. In Fig. 7.1 there are plots comparing different kinematic variables after the pre-selection cut, the black dots represent the proton collision data and the stacked histograms the Monte Carlo simulation of the different background processes and two signal benchmark points (with parameters described in the caption), the plots in Fig. 7.1 are related to lepton distributions and the plots in Fig. 7.2 correspond to the $\sum p_T$ variable for electron and muon channel. More kinematic distribution can be found in Appendix C, all distributions show good agreement between Standard Model background expectation and observed events in data.

In tables 7.4 and 7.5 is presented the event composition in the signal region for the Standard Model background, the two signal benchmark samples and the observed event in collision data as a function of $\sum p_T$ cut (starting from a $\sum p_T$ value of 0.7 TeV up to 1.5 TeV).

Table 7.1: Cut flow in collision data for the electron and muon channels. The total integrated luminosity is 1.04 fb^{-1}

Requirement	Data Stream	
	Egamma	Muon
Initial Events (prior online trigger requirements)	121 676 574	102 143 818
GRL	101 943 472	85 793 481
Trigger	59 553 711	42 216 057
Vertex	59 371 063	41 997 280
Jet cleaning	59 124 438	41 820 281
LArError	59 119 387	41 816 774
Cosmic veto	59 118 755	41 253 074
numLep>0	4 016 121	1 082 675
Leading lepton	4 015 628	1 082 242
LArhole veto	3 959 667	1 075 240
Tight Electron	1 681 111	1 075 240
Number of objects ≥ 3 (**Pre-selection**)	109 305	50 105
$\sum p_{\mathrm{T}} > 0.2$ TeV	66 489	31 334
$\sum p_{\mathrm{T}} > 0.7$ TeV + 3Obj $p_T > 100GeV$	586	241
$\sum p_{\mathrm{T}} > 0.8$ TeV + 3Obj $p_T > 100GeV$	348	145
$\sum p_{\mathrm{T}} > 0.9$ TeV + 3Obj $p_T > 100GeV$	196	78
$\sum p_{\mathrm{T}} > 1.0$ TeV + 3Obj $p_T > 100GeV$	113	46
$\sum p_{\mathrm{T}} > 1.2$ TeV + 3Obj $p_T > 100GeV$	41	15
$\sum p_{\mathrm{T}} > 1.5$ TeV + 3Obj $p_T > 100GeV$	8	2

Table 7.2: Cut flow for individual Monte Carlo samples, through pre-selection, for electron and muon channels. The numbers are normalized to 1.04 fb^{-1}.

	Monte Carlo Simulated Data Samples				
	QCD (Pythia)	QCD (Alpgen)	W+Jets	Z+Jets	$t\bar{t}$
Egamma Stream					
Requirement					
Vertex	$1.76 \times 10^8 \pm 8170000$	$7.095 \times 10^7 \pm 7866000$	5450000 ± 3560	810000 ± 326	27100 ± 47
numElec>0	$2.61 \times 10^6 \pm 3.1 \times 10^5$	$2.64 \times 10^6 \pm 4.21 \times 10^5$	$1.25 \times 10^6 \pm 1640$	$3.69 \times 10^5 \pm 220$	14700 ± 34
Leading e	$2.61 \times 10^6 \pm 3.1 \times 10^5$	$2.64 \times 10^6 \pm 4.21 \times 10^5$	$1.25 \times 10^6 \pm 1640$	$3.69 \times 10^5 \pm 220$	14400 ± 34
Tight	$2.10 \times 10^5 \pm 45000$	$4.13 \times 10^5 \pm 1.73 \times 10^5$	$1.04 \times 10^6 \pm 1490$	$3.0 \times 10^5 \pm 200$	12000 ± 31
nObj>=3	24000 ± 3900	27700 ± 8600	45000 ± 108	24900 ± 57	10400 ± 29
$\sum p_T > 200$ GeV	17700 ± 3100	24400 ± 8300	28300 ± 76	12150 ± 40	8900 ± 27
Muon Stream					
Requirement					
Vertex	$6.08 \times 10^7 \pm 2.2 \times 10^6$	$1.14 \times 10^7 \pm 8.5 \times 10^5$	$5.18 \times 10^6 \pm 3450$	$7.96 \times 10^5 \pm 321$	26700 ± 46
numMuons>0	3700 ± 1700	15100 ± 8050	$7.21 \times 10^5 \pm 1240$	$2.47 \times 10^5 \pm 179$	8490 ± 26
Leading m	3700 ± 1700	15100 ± 8050	$7.21 \times 10^5 \pm 1240$	$2.47 \times 10^5 \pm 179$	8280 ± 25.5
nObj>=3	103 ± 58	15100 ± 8050	28400 ± 86	11300 ± 38	6960 ± 23.5
$\sum p_T > 200$ GeV	103 ± 58	814 ± 467	17400 ± 60	6170 ± 28	5960 ± 22

Table 7.3: Cut flow for individual Monte Carlo samples, through pre-selection, for electron and muon channels. The two benchmark signal Black Hole and string ball samples are generated with fundamental scales and mass threshold scales of $M_D = 0.8$ TeV, $M_{TH} = 4$ TeV, and $M_S = 1$ TeV, $M_{TH} = 3$ TeV, respectively. The numbers are normalized to 1.04 fb^{-1}.

	Monte Carlo Simulated Data Samples			
	diboson	Single Top	Black Hole	String Ball
Requirement	Egamma Stream			
Vertex	5280 ± 13.1	7700 ± 12.6	866 ± 19.3	228 ± 8.6
numElec>0	2.79 $\times 10^3$ ± 9.4	3.77 $\times 10^3$ ± 8.7	615 ± 16	169 ± 7.4
Leading e	2.74 $\times 10^3$ ± 9.3	3.75 $\times 10^3$ ± 8.7	565 ± 16	161 ± 7.2
Tight	2.3 $\times 10^3$ ± 8.5	3.2 $\times 10^3$ ± 8.0	487 ± 14	128 ± 6.4
nObj>=3	543 ± 3.9	1.49 $\times 10^3$ ± 5.3	487 ± 14	128 ± 6.4
$\sum p_T > 200$ GeV	307 ± 2.9	1.02 $\times 10^3$ ± 4.3	487 ± 14	128 ± 6.4
Requirement	Muon Stream			
Vertex	4930 ± 13	7410 ± 12	932 ± 20	330 ± 10
numMuons>0	1590 ± 7	2170 ± 6.6	290 ± 11	78.7 ± 5.0
Leading m	1552 ± 7	2145 ± 6.5	228 ± 10	72 ± 4.8
nObj>=3	335 ± 3.1	992 ± 4.3	228 ± 9.8	72 ± 4.8
$\sum p_T > 200$ GeV	185 ± 2.3	662 ± 3.5	228 ± 9.8	72 ± 4.8

Table 7.4: Events in the signal region for electron channel. Signal and background numbers are from Monte Carlo simulations, normalized by cross-section to 1.04 fb^{-1}. The quoted uncertainties are statistical only.

$\sum p_T$	Black Hole	String Ball	SM	Data
> 00.7	423 ± 13.5	108 ± 5.9	781 ± 75.3	586
> 0.8	423 ± 13.5	108 ± 5.9	358 ± 8.79	348
> 0.9	423 ± 13.5	108 ± 5.9	216 ± 6.84	196
> 1.0	423 ± 13.5	108 ± 5.9	129 ± 5.7	113
> 1.2	422 ± 13.4	106 ± 5.85	49.7 ± 3.13	41
> 1.5	419 ± 13.4	101 ± 5.72	10.8 ± 1.06	8

Table 7.5: Events in the signal region for muon channel. Background numbers are from Monte Carlo simulations, normalized by cross-section to 1.04 fb^{-1}. The quoted uncertainties are statistical only.

$\sum p_T$	Black Hole	String Ball	SM	Data
> 0.7	186 ± 8.9	58.1 ± 4.3	285 ± 5.62	241
> 0.8	186 ± 8.9	58.1 ± 4.3	162 ± 4.26	145
> 0.9	186 ± 8.9	58.1 ± 4.3	91.3 ± 3.22	78
> 1.0	186 ± 8.9	58 ± 4.3	52.7 ± 2.46	46
> 1.2	186 ± 8.9	53.8 ± 4.1	14.2 ± 1.33	15
> 1.5	186 ± 8.9	47.3 ± 3.9	2.93 ± 0.58	2

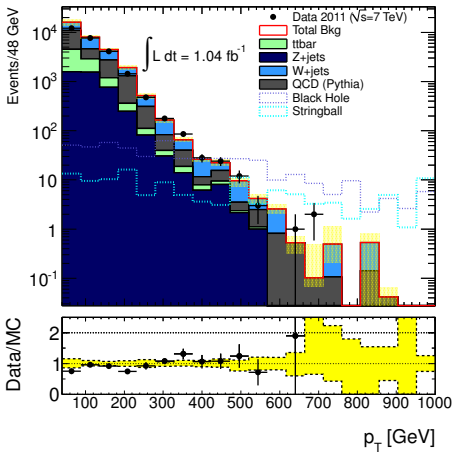

(a) Transverse momentum of leading electron.

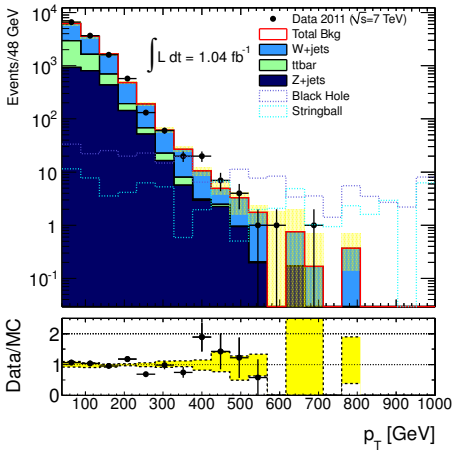

(b) Transverse momentum of leading muon.

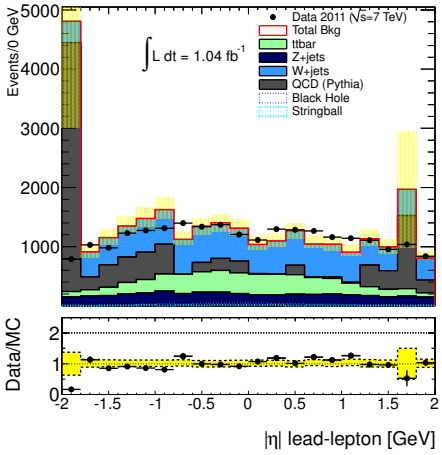

(c) Pseudo-rapidity of leading electron.

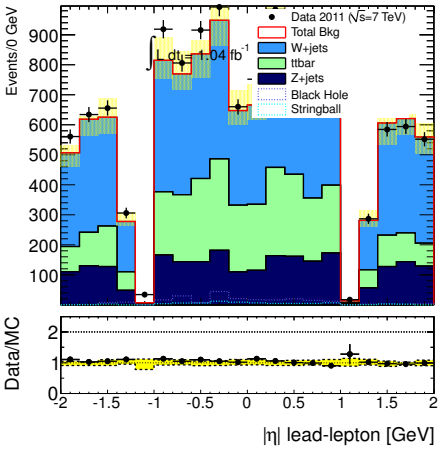

(d) Pseudo-rapidity of leading muon.

Figure 7.1: Transverse momentum and pseudo-rapidity of leading lepton after pre-selection. The yellow error band shows the full (statistical and systematic) error. The Monte Carlo samples are normalized by their cross-section to 1.04 fb^{-1}.

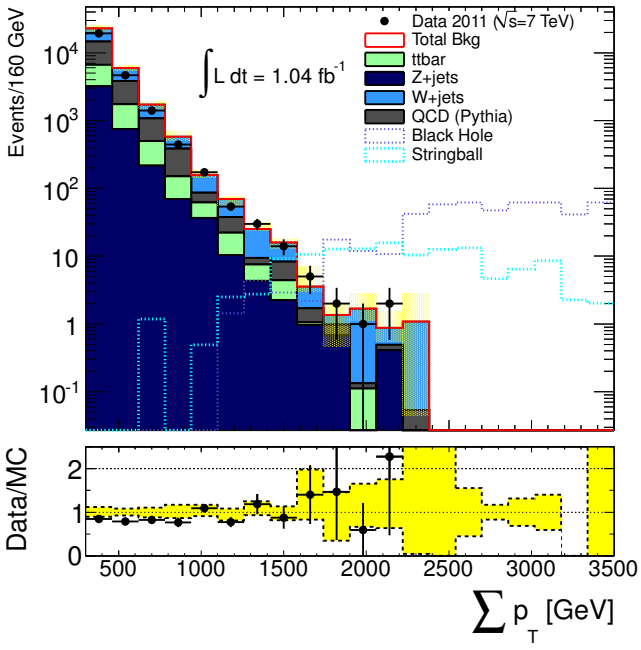

(a) Scalar sum of transverse momentum in electron events.

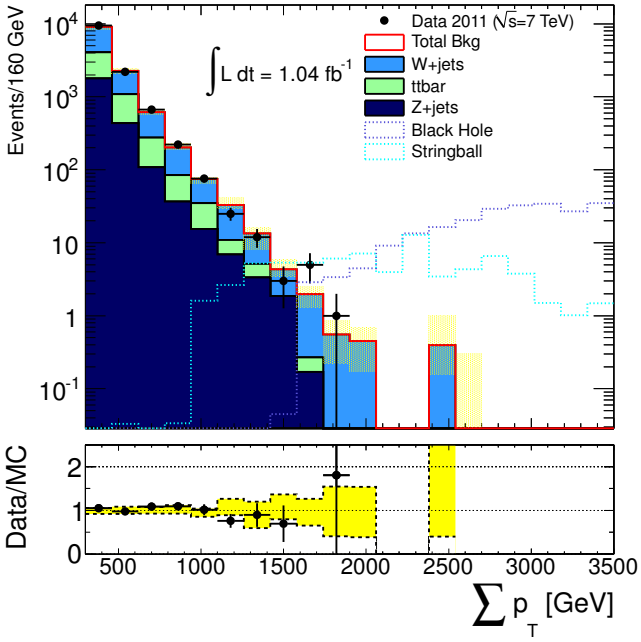

(b) Scalar sum of transverse momentum in muon events.

Figure 7.2: $\sum p_T$ after pre-selection. The yellow error band shows the full (statistical and systematic) error.The Monte Carlo samples are normalized by their cross-section to 1.04 fb^{-1}.

Chapter 8

Background Estimation

Background understanding is one of the key issues in every high-energy-particle analysis, the Monte Carlo background rates presented as cut-flow tables in chapter 7 are not enough to claim an agreement or excess of events in our observed data, specially at the region of interest (very high-p_T) in which the MC simulation generation lacks of statistics at the tails of the distributions (signal region) and the generator prediction at such energy regimes is not well understood (for instance in case of QCD multi-jets process), therefore different techniques have been implemented in order to understand and estimate the background composition in the signal region.

8.1 QCD (multi-jets) background

QCD (multi-jets) are relatively well understood processes at low energy values, while at the high-Pt region (signal region) the theoretical and statistical uncertainties become large, the contribution of these processes to our signal region is mostly due to: The large production of multi-jet events from proton collisions and the instrumental limitation of the calorimeters that can miss-identify a jet as an electron, in the case of muons it is much less likely this to happen and from our studies it was proved such contribution to be negligible, nevertheless in the Appendix E We discuss a method to estimate it from data (in order to probe that actually it is negligible).

An entirely "data-driven" method is required to estimate the background from QCD multi-jet processes in the electron channel, where jets fake electrons. The so-called Matrix method is used for estimation in signal region, in such method the electron quality criteria is relaxed from "tight" to "medium", and two control regions are defined, one in which the dominant contribution comes from prompt real electrons, and the other from fake electrons. The efficiency for an electron in each of these regions to pass the “tight” requirement is determined ($\varepsilon_{\text{real}}$ and $\varepsilon_{\text{fake}}$ for real and fake electrons, respectively). This allows the fraction of events passing medium and tight cuts in the signal region to be determined, the latter provide a data driven estimate of the QCD background. The cuts used to define both samples are as follows (starting from the pre-selection set of events):

- Fake lepton Control Region:
  - Exactly one electron in the event (to reduce the contribution from $Z + jets$ events)
  - $E_T^{miss} < 15$ GeV (QCD multi-jets events characterized with low E_T^{miss} values)
- Real lepton Control Region:
  - Exactly two opposite sign electrons
  - Cut on the di-electron invariant mass (80$< m_{ee} <$100 GeV)

The purity of each region in terms of real ($Z + jets$) and fake (multi-jets) leptons content is quantified in tables 8.1 and 8.2 respectively. The method procedure is summarized as follows. In the signal region we count the numbers of data events in a "looser" electron sample which pass (N_{pass}) and fail (N_{fail}) the final tighter electron selection criteria. We then define N_{real} and N_{fake} as the numbers of events for which the electrons are real and fake, respectively. The following relationships hold:

$$N_{\text{pass}} = \varepsilon_{\text{real}} N_{\text{real}} + \varepsilon_{\text{fake}} N_{\text{fake}}, \tag{8.1}$$

$$N_{\text{fail}} = (1 - \varepsilon_{\text{real}}) N_{\text{real}} + (1 - \varepsilon_{\text{fake}}) N_{\text{fake}} \tag{8.2}$$

Simultaneous solution of these two equations gives a prediction for the number of events in data in the signal region that have fake electrons:

$$N_{\text{fake}}^{\text{pass}} = \varepsilon_{\text{fake}} N_{\text{fake}} = \frac{N_{\text{fail}} - (1/\varepsilon_{\text{real}} - 1) N_{\text{pass}}}{1/\varepsilon_{\text{fake}} - 1/\varepsilon_{\text{real}}} \tag{8.3}$$

Table 8.1: Background composition in the $Z + jets$ (real lepton) dominated control region.

QCD (Pythia)	W+jets	Z+jets	$t\bar{t}$
0%	1.5×10^{-2}%	99.2%	0.8%

The corresponding $\varepsilon_{\text{fake}}$ and $\varepsilon_{\text{true}}$ are presented in equations 8.4 and 8.5 respectively along with its statistical plus systematic uncertainty and as a function of $\sum p_T$ in Fig. 8.1 (flatness dependency motivates the extrapolation from control 300 $<\sum p_T <$ 700 GeV to signal region $\sum p_T >$ 700 GeV), systematic uncertainty was calculated changing both $\varepsilon_{\text{fake}}$ and $\varepsilon_{\text{true}}$ by a percentage of its value an then looking at the effect of the final estimation.

Table 8.2: Background composition in the QCD-Multi-jet (fake lepton) dominated control region.

QCD (Pythia)	W+jets	Z+jets	$t\bar{t}$
88.8%	6.1%	3.3%	1.8%

The final results for QCD multi-jets estimation as a function of $\sum p_T$ cut is presented in table 8.3, the last two columns present the only MC prediction comparing two different generators (Pythia and Alpgen) the second column shows the estimation from the Matrix method, from the number in the table it is clear that only MC prediction is lacking of statistics in the signal region which makes unreliable its prediction, the matrix method offers a better estimation and the uncertainties are reduced as well.

$$\varepsilon_{\text{fake}} = 0.17 \pm 0.002(\text{stat.}) \pm 0.04(\text{sys.}), \tag{8.4}$$

$$\varepsilon_{\text{true}} = 0.91 \pm 0.05(\text{stat.}) \pm 0.04(\text{sys.}). \tag{8.5}$$

$\sum p_T$ [GeV]	**QCD (data-driven)**	QCD(Pythia)	QCD (Alpgen)
>0.7 TeV	137 ± 9.67 ± 44.6	256 ± 74.9	101 ± 52
>0.8 TeV	75.0 ± 7.34 ± 24.5	53.4 ± 6.6	96.1 ± 50.9
>0.9 TeV	41.5 ± 5.5 ± 13.6	34.1 ± 5.1 a	96.1 ± 50.9
>1.0 TeV	24.6 ± 4.2 ± 8.1	28.1 ± 4.6	96.1 ± 50.9
>1.2 TeV	8.1 ± 2.5 ± 2.7	8.85 ± 2.3	96.1 ± 50.9
>1.5 TeV	1.30 ± 1.07 ± 0.44	1.14 ± 0.12	0

Table 8.3: Comparison of expected number of expected QCD Multi-jet events, for the electron channel, using Alpgen and Pythia MC samples and the output of the data-driven method, as a function of $\sum p_T$ cut. The MC samples are normalized according to luminosity.

8.2 $Z + jets$ background

The Z+jets background is estimated by simply counting events in both data and MC in a control region enriched in Z+jets events, and defining a scale factor as the ratio of events observed in data, with small non-Z backgrounds subtracted, to that observed in MC. The resulting scale factor (SF) is used to

scale the MC prediction for the Z+jets background in the signal region. The Z+jets control region is defined as follows (after the pre-selection):

- Exactly two opposite charge leptons in the event (e^+e^-,$\mu^+\mu^-$).
- Invariant mass cut $80 < M_{\ell\ell} < 100$ GeV;
- $300 < \sum p_T < 700$ GeV (Control region)

In Fig. 8.2 we illustrate a comparison between data and Monte Carlo in the $Z + jets$ control region as a function of invariant mass. Fig. 8.3 compares the data to the Monte Carlo simulation, as a function of $\sum p_T$. The agreement between data and Monte Carlo is reasonable, though fluctuations are observed in the muon channel. The nominal scale factors are 0.926 ± 0.031 for the electron channel and 0.848 ± 0.039 for the muon channel, where the errors are statistical only.

Systematic effects due to variation of the scale factors as a function of $\sum p_T$ are evaluated by recalculating the scale factors in different $\sum p_T$ bins, the results of which are given in Tables 8.4 and 8.5 (and illustrated in Fig. 8.3). We conservatively take the largest variation, 3.4% for the electron channel and 16% for the muon channel, as the systematic uncertainty for this effect. These scale factors are also affected by uncertainties on both jet and lepton energy scales, evaluated by varying the jet energy scales and resolutions and lepton momentum resolutions, as described in chapter 6. Tables 8.6 and 8.7 summarize the effect of all Z+jets SF systematic uncertainties considered on the control region. The final values of the scaling factors are:

$$\text{SF (muon)} = 0.85 \pm 0.04 \pm 0.14 \quad (8.6)$$

$$\text{SF (electron)} = 0.93 \pm 0.03 \pm 0.08 \quad (8.7)$$

As described above, these scale factors are used to scale the observed number of Monte Carlo simulated Z+jets events in the signal region, to obtain the final estimate of the Z+jets background. Uncertainties remain on the extrapolation from the $\sum p_T$ range of the control region ($300 < \sum p_T < 700$ GeV) to that of the signal regions ($\sum p_T > 700$ GeV). This systematic uncertainty is estimated by tabulating the variations in the number of Monte Carlo simulated Z+jets in the SR, after normalization in the control region, when using different MC generators (Sherpa in place of the nominal Alpgen), Tables 8.8 and 8.9, and different parton distribution functions (`CTEQ6.6` in place of the nominal `CTEQ6L1`), Tables 8.10 and 8.11. For Sherpa the statistics are poor (nearly a factor of four less than that of Alpgen), which contributes to large, purely statistical, fluctuations, particularly in the highest $\sum p_T$ SR bins. Thus, we

$\sum p_T$ bin (GeV)	Scale Factor (SF)	Deviation from Nominal (%)
[200-700]	0.971 ± 0.026	14
[250-700]	0.927 ± 0.032	9
[300-700]	0.848 ± 0.039	0
[350-700]	0.843 ± 0.050	−0.8
[400-700]	0.755 ± 0.058	−11
[450-700]	0.740 ± 0.072	−13
[500-700]	0.712 ± 0.089	−16

Table 8.4: Variation from the nominal value of the Z+jets scale factor for different choices of $\sum p_T$ bin, for the muon channel. The nominal SF is from the 300 $<\sum p_T <$ 700 GeV bin.

$\sum p_T$ bin (GeV)	Scale Factor (SF)	Deviation from Nominal (%)
[200-700]	0.948 ± 0.020	2.0
[250-700]	0.945 ± 0.025	1.6
[300-700]	0.926 ± 0.031	0.0
[350-700]	0.962 ± 0.040	3.4
[400-700]	0.943 ± 0.049	1.4
[450-700]	0.941 ± 0.061	1.2
[500-700]	0.905 ± 0.075	−2.7

Table 8.5: Variation from the nominal value of the Z+jets scale factor for different choices of $\sum p_T$ bin, for the electron channel. The nominal SF is from the 300 $<\sum p_T <$ 700 GeV bin.

SF	JES up (%)	JES down (%)	JER (%)	MMR up (%)	MMR down (%)	CR def. (%)
0.85 ± 0.04	2.8	2.9	1.2	0.4	3.7	16

Table 8.6: Nominal Z+jets scale factor (SF), for the muon channel, and systematic uncertainties derived from varying the jet energy scale (JES), jet energy resolution (JER), muon momentum resolution scale factors (MMR) and control region (CR) $\sum p_T$ definition.

SF	JES up (%)	JES dwn (%)	JER (%)	EER dwn/up (%)	EES dwn/up (%)	CR def. (%)
0.93 ± 0.03	6.4	4.3	2.5	0.4/0.4	2.4/4.4	3.4

Table 8.7: Nominal Z+jets scale factor (SF), for the electron channel, and systematic uncertainties derived from varying the jet energy scale (JES), jet energy resolution (JER), electron energy resolution (EER), electron energy scale (EES) and control region (CR) $\sum p_T$ definition.

quote the generator-associated systematic uncertainty as the mean variation from the nominal Alpgen value for the SR bins with minimum $\sum p_T$ no greater than 1000 GeV. For the final systematic uncertainty resulting from variations in the PDFs, we use the largest observed deviations from the nominal PDFs, which come from varying the error sets in the `CTEQ6.6` PDFs.

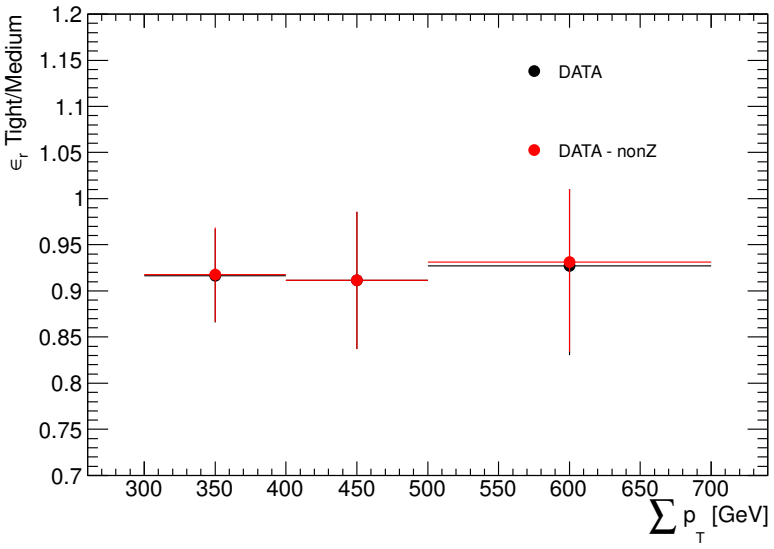

(a) $\varepsilon_{\text{real}}$ as a function of $\sum p_T$, red curve shows efficiency DATA/MC subtracting the non-Z components from the data.

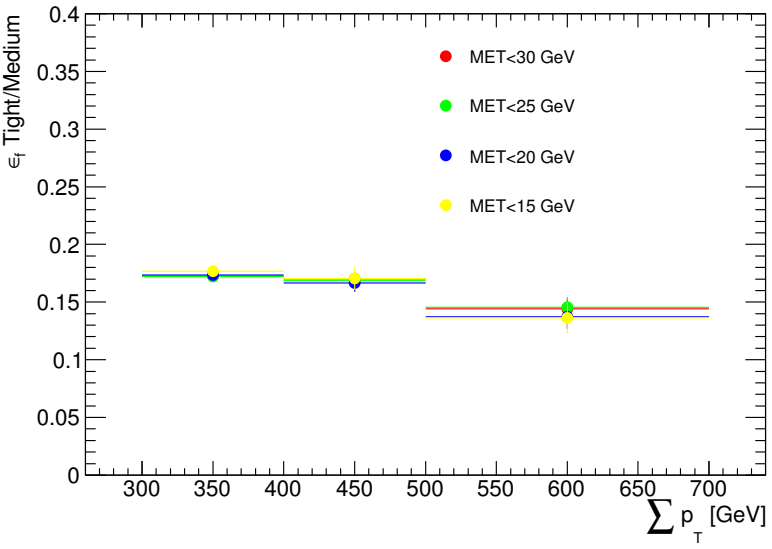

(b) ε_{fake} as a function of $\sum p_T$, for different cuts on E_T^{miss}

Figure 8.1: $\sum p_T$ dependencies of $\varepsilon_{\text{real}}$ and $\varepsilon_{\text{fake}}$

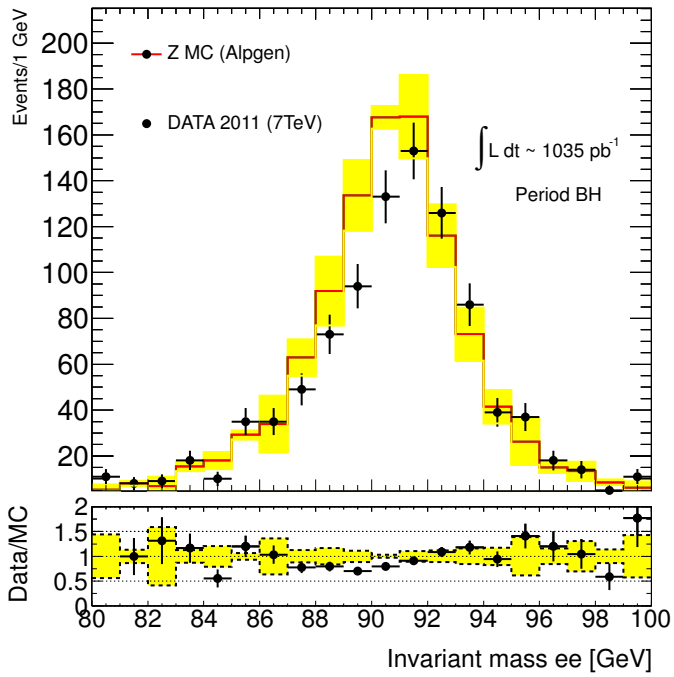

(a) electron channel

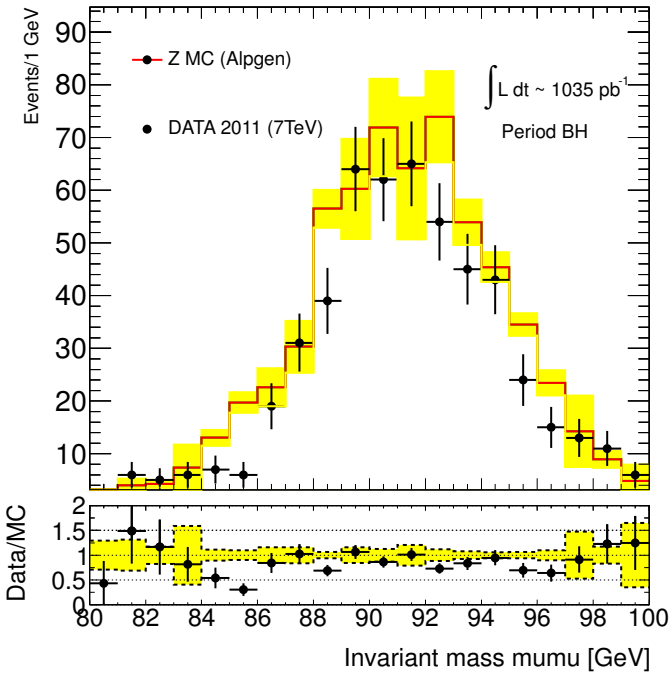

(b) muon channel

Figure 8.2: The invariant mass $M_{\ell\ell}$ distribution for data and Monte Carlo simulation for the Z+jets CR.

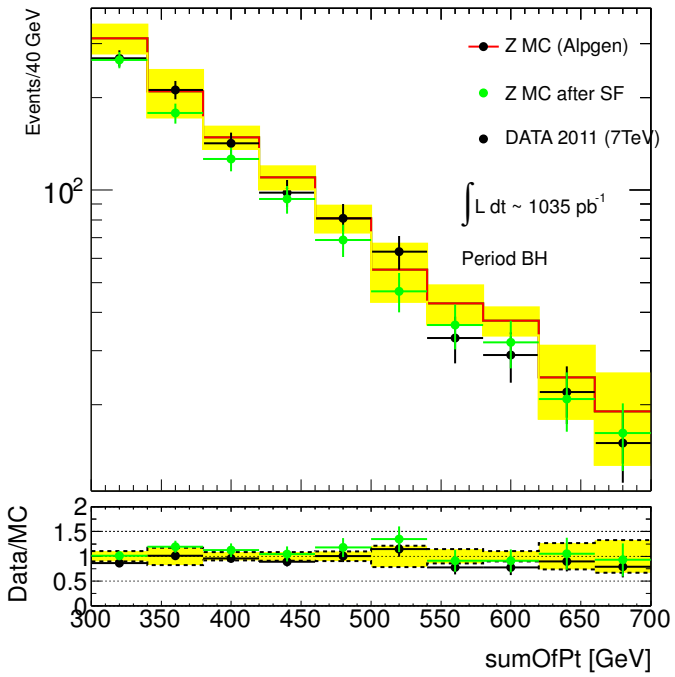

(a) electron channel

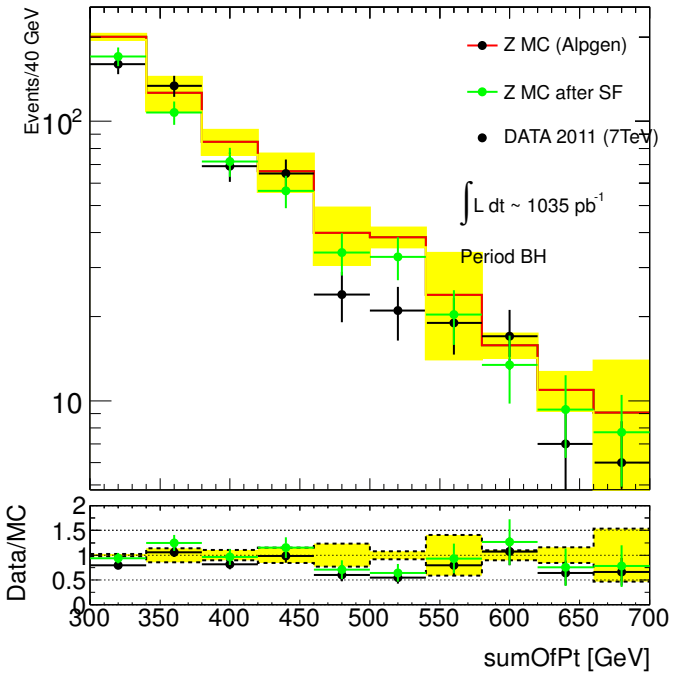

(b) muon channel

Figure 8.3: The $\sum p_T$ distributions for data and Monte Carlo simulation for the Z+jets CR. The green histogram displays the MC $\sum p_T$ distribution after having applied the SF correction.

Signal Region	Evts. Alpgen (SF$= 0.85 \pm 0.04$)	Evts. Sherpa (SF$= 1.16 \pm 0.07$)	Frac. Diff. (%)
$\sum p_T > 700$ GeV	49.5	58.5	+18
$\sum p_T > 800$ Gev	32.0	32.5	+2
$\sum p_T > 900$ GeV	19.6	15.8	−19
$\sum p_T > 1000$ GeV	13.1	10.7	−18
$\sum p_T > 1200$ GeV	3.97	3.5	−11
$\sum p_T > 1500$ GeV	0.63	0.6	−4

Table 8.8: Number of predicted Z+jets events, for the muon channel, in the SR using Alpgen (nominal) and Sherpa. In each case, a SF is derived from the CR to scale the raw number of observed events in the SR. The last column shows the difference between the Sherpa and Alpgen predictions.

Signal Region	Evts. Alpgen (SF$= 0.93 \pm 0.03$)	Evts. Sherpa (SF$= 1.26 \pm 0.06$)	Frac. Diff. (%)
$\sum p_T > 700$ GeV	119.0	118.3	−0.1
$\sum p_T > 800$ GeV	73.7	60.2	−18
$\sum p_T > 900$ GeV	47.0	33.8	−28
$\sum p_T > 1000$ GeV	22.2	18.2	−18
$\sum p_T > 1200$ GeV	9.0	7.3	−18
$\sum p_T > 1500$ GeV	2.63	0.9	−65

Table 8.9: Number of predicted Z+jets events, for the electron channel, in the SR using Alpgen (nominal) and Sherpa. In each case, a SF is derived from the CR to scale the raw number of observed events in the SR. The last column shows the difference between the Sherpa and Alpgen predictions.

Signal Region	CTEQ6.6	CTEQ6.6: Up	CTEQ6.6: Low
$\sum p_T > 700$ GeV	-0.051	0.048	-0.041
$\sum p_T > 800$ GeV	-0.066	0.050	-0.045
$\sum p_T > 900$ GeV	-0.071	0.058	-0.050
$\sum p_T > 1000$ GeV	-0.091	0.055	-0.047
$\sum p_T > 1200$ GeV	-0.067	0.085	-0.071
$\sum p_T > 1500$ GeV	-0.224	0.029	-0.052

Table 8.10: Fractional change in expected Z+jets background in the SR after CR normalization, for several PDF choices: CTEQ6.6 compared to nominal CTEQ6L1 CTEQ6.6 with upper error set uncertainties, and CTEQ6.6 with lower error set uncertainties (relative to CTEQ6.6 central value). These are for the muon channel.

Signal Region	CTEQ6.6	CTEQ6.6: Up	CTEQ6.6: Low
$\sum p_T > 700$ GeV	-0.059	0.034	-0.029
$\sum p_T > 800$ GeV	-0.071	0.041	-0.035
$\sum p_T > 900$ GeV	-0.091	0.039	-0.035
$\sum p_T > 1000$ GeV	-0.147	0.046	-0.044
$\sum p_T > 1200$ GeV	-0.158	0.067	-0.063
$\sum p_T > 1500$ GeV	0.109	0.107	-0.100

Table 8.11: Fractional change in expected Z+jets background in the SR after CR normalization, for several PDF choices: CTEQ6.6 relative to nominal CTEQ6L1 CTEQ6.6 with upper error set uncertainties, and CTEQ6.6 with lower error set uncertainties (relative to CTEQ6.6 central value). These are for the electron channel.

The relative uncertainties on Z+jets events in the SR (before applying SF), including full systematic uncertainties, are detailed in Tables 8.12 and 8.13 for the muon and electron channels respectively. The final percentage uncertainties for the signal regions, after the normalization in the control regions, are given in Tables 8.14 (electron channel) and 8.15 (muon channel), whilst Tables 8.16 and 8.17 show the final prediction and absolute uncertainties as a function of minimum $\sum p_T$.

$\sum p_T$ [TeV]	JES u [%]	JES d [%]	JER [%]	EER d [%]	EER u [%]	EES up [%]	EES down [%]
>0.7	-10.9	10.2	-0.8	0	-0.8	-2.3	0.8
>0.8	-7.3	7.2	-0.8	0	0.3	-0.6	2.0
>0.9	-14.1	9.1	1.4	-1.6	-1.0	-3.6	2.6
>1.0	-16.3	14.2	-4.2	0	0	-5.9	4.6
>1.2	-12.9	12.3	8.3	0	0	-3.7	0
>1.5	-4.6	0.0	-4.6	0	0	0	0

Table 8.12: Relative uncertainty on number of Z+jets events in signal region due to JES, JER, EER, EES for electron channel.

$\sum p_T$ [TeV]	JES u [%]	JES d [%]	JER [%]	MMR u [%]	MMR d [%]
>0.7	-8.9	4.6	-0.7	0.5	4.6
>0.8	-10.1	7.4	4.5	0.8	4.5
>0.9	-14.8	10.0	-2.2	-1.3	7.4
>1.0	-9.7	6.5	-4.5	0	5.8
>1.2	-17.3	6.6	-17.3	0	6.6
>1.5	-47.2	59.9	-7.3	0	0

Table 8.13: Relative uncertainty on number of Z+jets events in signal region due to JES, JER, MMR for muon channel.

$\sum p_T$ [GeV]	JES u	JES d	JER	EES u	EES d	EER u	EER d	MC	PDF	CR	Total
>0.7	3.9	-6.4	-1.7	-2.1	1.6	0.4	-0.4	16.0	3.4	3.4	18.1
>0.8	0.1	-3.6	-2.1	-4.1	-0.01	-0.2	-0.7	16.0	4.1	3.4	17.9
>0.9	6.9	-5.2	1.2	-0.9	-0.1	0.7	1.3	16.0	3.9	3.4	18.3
>1.0	9.0	-10.5	1.7	1.3	2.2	0.5	-0.3	16.0	4.6	3.4	20.2
>1.2	4.8	-9.4	-6.9	-1.7	1.5	-0.5	-1.3	16.0	6.6	3.4	21.2
>1.5	-1.9	4.3	2.2	-4.2	2.6	0.6	0.2	16.0	10.7	3.4	20.6

Table 8.14: Relative uncertainty on Z+jets estimation for electron channel, by varying JES,JER,EES,EER (maximum between up and down considered for Total) both in both control and signal region, additional uncertainty considered from MC generator (Alpgen vs Sherpa), PDF re-weighting and control region definition

$\sum p_t$ [GeV]	JES u	JES d	JER	MMR u	MMR d	MC	PDF	CR	Total
>0.7	5.8	-1.9	0.6	-0.2	-1.2	14.2	4.8	16	22.7
>0.8	6.9	-4.9	-3.5	-0.5	-1.1	14.2	5.0	16	23.3
>0.9	11.9	-7.2	1.2	1.1	-3.8	14.2	5.8	16	25.5
>1.0	6.6	-3.9	3.2	0.3	-2.4	14.2	5.5	16	23.4
>1.2	13.9	-4.1	15.8	0.3	-3.3	14.2	8.5	16	31.4
>1.5	52.0	-56.2	12.6	6.7	10.1	14.2	5.2	16	62.5

Table 8.15: Relative uncertainty on Z+jets estimation for muon channel, by varying JES,JER,MMR (maximum between up and down considered for Total) both in both control and signal region, additional uncertainty considered from MC generator (Alpgen vs Sherpa), PDF re-weighting and control region definition

$\sum p_T$ (GeV)	Z+jets (MC)	SF	Z+jets (final)
> 700	$128 \pm 4 \pm 15$	$0.93 \pm 0.03 \pm 0.08$	$119 \pm 4 \pm 21.5$
> 800	$79.3 \pm 3.1 \pm 6.6$	$0.93 \pm 0.03 \pm 0.08$	$74 \pm 4 \pm 13.2$
> 900	$50.5 \pm 2.5 \pm 7.7$	$0.93 \pm 0.03 \pm 0.08$	$46.9 \pm 2.8 \pm 8.6$
> 1000	$23.9 \pm 1.7 \pm 4.3$	$0.93 \pm 0.03 \pm 0.08$	$22.2 \pm 1.8 \pm 4.5$
> 1200	$9.7 \pm 1.1 \pm 1.6$	$0.93 \pm 0.03 \pm 0.08$	$9.1 \pm 1.0 \pm 1.9$
> 1500	$2.8 \pm 0.58 \pm 0.2$	$0.93 \pm 0.03 \pm 0.08$	$2.6 \pm 0.5 \pm 0.5$

Table 8.16: Estimated Z+jets background in signal region as a function of $\sum p_T$, in the electron channel, normalized according to the scale factor derived from the control region. The first quoted error is the statistical uncertainty, the second is the systematic.

$\sum p_T$ (GeV)	Z+jets (MC)	SF	Z+jets (final)
> 700	$58.2 \pm 2.7 \pm 6.2$	$0.85 \pm 0.04 \pm 0.14$	$49.5 \pm 3.2 \pm 11.2$
> 800	$37.6 \pm 2.1 \pm 4.8$	$0.85 \pm 0.04 \pm 0.14$	$32.0 \pm 2.4 \pm 7.5$
> 900	$23.0 \pm 1.7 \pm 4.0$	$0.85 \pm 0.04 \pm 0.14$	$19.5 \pm 1.7 \pm 5.0$
> 1000	$15.4 \pm 1.3 \pm 1.9$	$0.85 \pm 0.04 \pm 0.14$	$13.1 \pm 1.3 \pm 3.1$
> 1200	$4.7 \pm 0.7 \pm 1.2$	$0.85 \pm 0.04 \pm 0.14$	$4.0 \pm 0.6 \pm 1.2$
> 1500	$0.75 \pm 0.23 \pm 0.50$	$0.85 \pm 0.04 \pm 0.14$	$0.6 \pm 0.2 \pm 0.4$

Table 8.17: Estimated Z+jets background in the signal region as a function of $\sum p_T$, in the muon channel, normalized according to the scale factor derived from the control region. The first quoted error is the statistical uncertainty, the second is the systematic.

8.3 Combined $W + jets$ and $t\bar{t}$ background

The W+jets and $t\bar{t}$ processes comprise significant backgrounds[1] in the signal region for both electron and muon channels, and, consequently, their accurate estimation is highly important. The simplest way to predict the contribution from these processes is based on Monte Carlo estimates. The generators for these processes are relatively advanced and estimates of their cross-sections are known quite accurately; nonetheless, other methods relying upon the data can be used to supplement and improve the predictions. In this semi-data-driven approach, the W+jets and $t\bar{t}$ estimates from MC simulation are compared to data in a *control region* that is dominated by those two processes. This yields a scale factor, which is then used to scale the size of these backgrounds predicted by the MC in the *signal region*.

The control region is selected as follows (after pre-selection):

- $30 < E_{\mathrm{T}}^{\mathrm{miss}} < 60$ GeV (both W+jets and Top processes include neutrino generation)
- exactly one lepton passing pre-selection cuts
- $300 < \sum p_T < 700$ GeV;
- $40 < M_{\mathrm{T}} < 100$ GeV (to increase W boson production), where $M_{\mathrm{T}} = \sqrt{2 \cdot p_{\mathrm{T}}^{\ell} \cdot E_T^{miss} \cdot (1 - \cos(\Delta\phi(\vec{p}_{\mathrm{T}}^{\ell}, \vec{p}_{\mathrm{T}}^{\mathrm{miss}})))}$

The $\sum p_T$ requirement ensures orthogonality with the signal region and the $E_{\mathrm{T}}^{\mathrm{miss}}$ and single lepton requirements suppress the Z+jets and QCD contributions. The predicted composition of this control region, along with the observed number of events in data, are given in Tables 8.18 and 8.19.

W+jets/$t\bar{t}$ (MC)	Z+jets (MC)	QCD (data-driven)	Data
3150 ± 20	370 ± 7	710 ± 24	3996

Table 8.18: Event composition in the W+jets/$t\bar{t}$ control region for the electron channel. The error shown is statistical only; the size of the systematic errors on the prediction are detailed in Table 8.21.

Separating the W+jets and $t\bar{t}$ backgrounds is difficult, without the use of b-tagging techniques, which introduce significant systematic uncertainties through the imperfect simulation of the tagging efficiency at high p_T. For this

[1] Single top is a small background, approximately 10% the size of the $t\bar{t}$ background and for the rest of this thesis the single top process is included in what we denote as $t\bar{t}$, unless explicitly noted otherwise.

W+jets/$t\bar{t}$ (MC)	Z+jets (MC)	Data
2040 ± 15	198 ± 5	2331

Table 8.19: Predicted events in the W+jets/$t\bar{t}$ control region for the muon channel (there are zero predicted QCD events). The error shown is statistical only; the size of the systematic errors on the prediction are detailed in Table 8.20.

Nominal SF	JES up (%)	JES down (%)	JER (%)	MMR up (%)	MMR down (%)	Total (%)
1.05 ± 0.02	8.2	7.6	3.8	6.6	1.0	11.2

Table 8.20: Nominal W+jets + $t\bar{t}$ scale factor (SF), for the muon channel, and systematic uncertainties derived from varying the jet energy scale (JES), jet energy resolution (JER), and muon momentum resolution scale factors (MMR).

analysis, there is, in fact, no need to separate the two contributions, given the $\sum p_T$ distributions (the sole quantity that is used in setting limits on new physics) are nearly identical, as can be seen in Fig. 8.4. Thus, we treat W+jets and $t\bar{t}$ as a single background and derive a scale factor that is used to extrapolate the observed sum of the two backgrounds from the CR to the SR. The calculations of the SF and associated systematic uncertainties follow exactly those of the Z+jets background, as described in Section 8.2, except that the variation of the SF as a function of $\sum p_T$ CR bin for the combined W+jets and $t\bar{t}$ background is negligible.

The systematic errors on the control region, and hence on the scaling factor, given here are described in greater detail in Tables 8.20 and 8.21 for the muon and electron channels respectively. We measure:

$$\text{SF (muon)} = 1.05 \pm 0.02 \pm 0.12\,, \tag{8.8}$$

$$\text{SF (electron)} = 0.93 \pm 0.02 \pm 0.14\,. \tag{8.9}$$

Both SF are consistent with unity. In Fig. 8.5, the $\sum p_T$ distributions of the data (with the small contributions from Z+jets and QCD backgrounds subtracted according to their MC expectation) and the MC simulation in the control region are displayed, and demonstrate good agreement.

There are additional uncertainties from the extrapolation from control to signal regions. These are evaluated by comparison with alternative generators, and are detailed in Tables 8.22 (muon channel), 8.23 (electron channel). The experimental uncertainties evaluated on the control regions are also determined for the signal regions, and detailed in Tables 8.24 and 8.25 for electron

Nominal SF	JES up (%)	JES down (%)	JER (%)	EER dwn/up (%)	EES dwn/up (%)	Total (%)
0.93 ± 0.02	13.0	8.6	6.4	1.0/ 0.0	1.0/2.4	14.7

Table 8.21: Nominal W+jets + $t\bar{t}$ scale factor (SF), for the electron channel, and systematic uncertainties derived from varying the jet energy scale (JES), jet energy resolution (JER), electron energy resolution (EER) and electron energy scale (EES).

and muon channels.

The relevant uncertainty is not the *a priori* effect, but the *residual* uncertainty after the control region normalization procedure. These final uncertainties are given in Tables 8.26 and 8.27 for electron and muon channels.

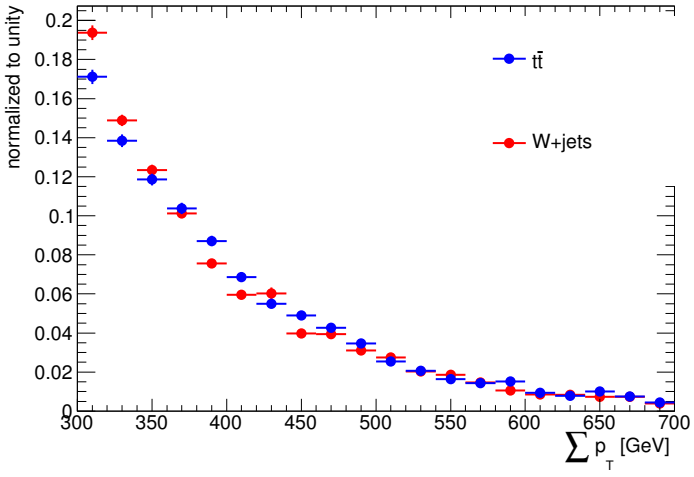

(a) Electron Channel

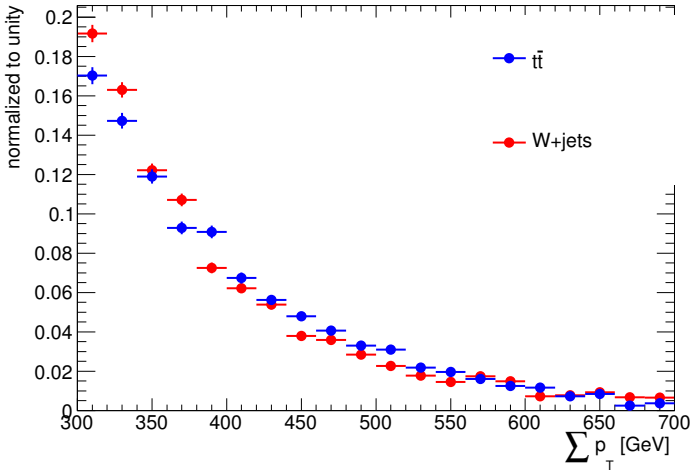

(b) Muon Channel

Figure 8.4: The $\sum p_T$ distributions for MC simulated W+jets (red) and $t\bar{t}$ (blue) events in the control region.

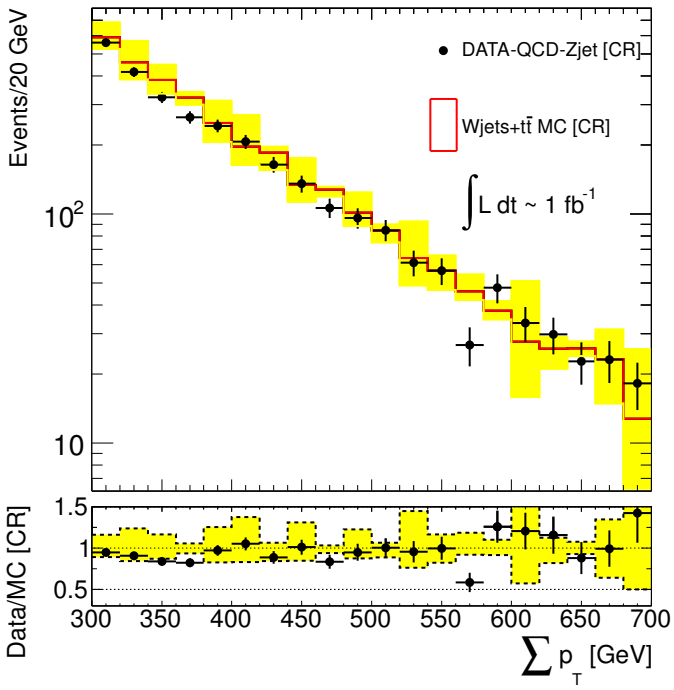

(a) Electron Channel

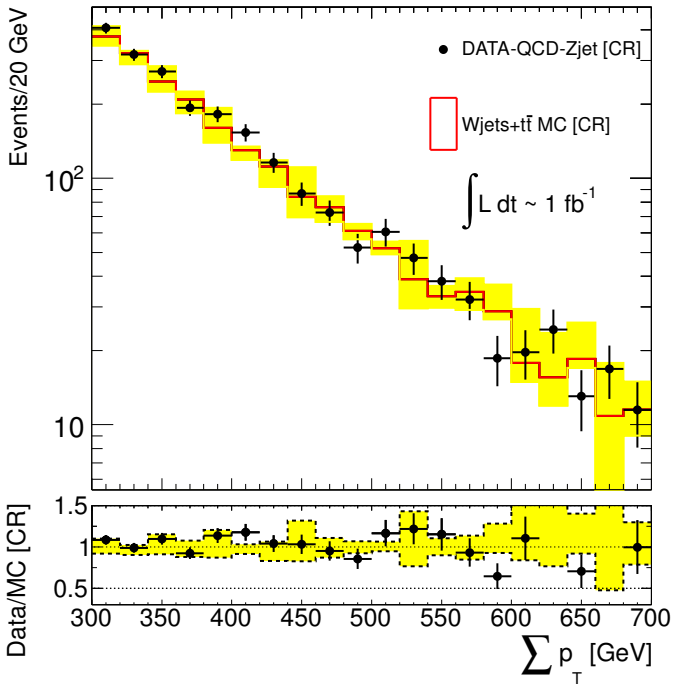

(b) Muon Channel

Figure 8.5: The $\sum p_T$ distributions for data (black points) and MC simulation (red histograms) of W+jets and $t\bar{t}$ background. For the data distribution, the small Z+jets and QCD processes have been subtracted, using the predicted shapes and normalization from the MC simulation.

Signal Region	Evts. Alpgen (SF= 1.05 ± 0.02)	Evts. Sherpa (SF= 1.09 ± 0.04)	Frac. Diff. (%)
$\sum p_T > 700$ GeV	231.4	188.7	-18
$\sum p_T > 800$ Gev	127.0	111.4	-12
$\sum p_T > 900$ GeV	70.3	66.9	-5
$\sum p_T > 1000$ GeV	38.3	45.7	$+19$
$\sum p_T > 1200$ GeV	9.8	(no stat.)	(no stat.)
$\sum p_T > 1500$ GeV	2.19	(no stat.)	(no stat.)

Table 8.22: The number of predicted W+jets and $t\bar{t}$ events, for the muon channel, in the SR using Alpgen (nominal) and Sherpa. In each case, a SF is derived from the CR to scale the raw number of observed events in the SR. The last column shows the difference between the Sherpa and Alpgen predictions. For $\sum p_T > 1200$ GeV there are no events observed in the SR for Sherpa so we assume a 19% difference from Alpgen, taken from the $\sum p_T > 1000$ GeV bin.

Signal Region	Evts. Alpgen (SF= 0.93 ± 0.02)	Evts. Sherpa (SF= 1.10 ± 0.04)	Frac. Diff. (%)
$\sum p_T > 700$ GeV	358.0	407.0	+13
$\sum p_T > 800$ GeV	202.4	233.9	+15
$\sum p_T > 900$ GeV	118.1	125.8	+6
$\sum p_T > 1000$ GeV	69.7	89.6	+28
$\sum p_T > 1200$ GeV	28.1	38.7	+27
$\sum p_T > 1500$ GeV	6.22	(no stat.)	(no stat.)

Table 8.23: The number of predicted W+jets and $t\bar{t}$ events, for the electron channel, in the SR using Alpgen (nominal) and Sherpa. In each case, a SF is derived from the CR to scale the raw number of observed events in the SR. The last column shows the difference between the Sherpa and Alpgen predictions. For $\sum p_T > 1500$ GeV there are no events observed in the SR for Sherpa so we assume a 27% difference from Alpgen, taken from the $\sum p_T > 1200$ GeV bin.

$sump_T$	EER (up/down) [%]	JES (up/down) [%]	JER [%]	EES (up/down) [%]
> 0.7	0 / 0.5	-12.0 / 11.5	-1.0	-4.2 / 2.1
> 0.8	0.4 / 0.1	-11.1 / 11.5	-1.3	-2.7 / 2.5
> 0.9	0 / -1.7	-13.3 / 15.4	2.1	-3.2 / 2.1
> 1.0	1.2 / -0.1	-12.3 / 12.5	-2.5	-1.9 / 1.5
> 1.2	0.5 / 1.2	-12.3 / 18.4	-4.1	0 / 3.2
> 1.5	-1.9 / 0	-7.5 / 21.4	4.4	0 / 0

Table 8.24: Relative uncertainty on the combined W+jets/$t\bar{t}$ events in signal region, due to variations on JES,JER,EES, and EER in the electron channel.

$\sum p_T$	MMR (up/down) [%]	JES (up/down) [%]	JER [%]
> 0.7	2.4 / 0.1	-9.3 / 8.8	3.4
> 0.8	1.7 / 0.3	-12.8 / 10.4	-1.9
> 0.9	1.8 / 0.9	-9.5 / 14.6	4.0
> 1.0	2.0 / 1.3	-10.1 / 5.2	5.2
> 1.2	6.2 / 0	-26.8 / 6.8	-15.2
> 1.5	1.9/ 0	-16.7 / 17.7	13.3

Table 8.25: Relative uncertainty on the combined W+jets/$t\bar{t}$ events in signal region, due to variations on JES,JER and MMR in the muon channel.

In Tables 8.28 and 8.29 we present a summary of the systematic uncertainties for our estimation of the W+jets/$t\bar{t}$ background, for the electron and muon channels, respectively. The quoted numbers give the percentage change in the evaluated background prediction in the signal region, after normalization in the relevant control region. Where control and signal region are affected similarly, there is a cancellation in the uncertainty (the residual shape uncertainty, after normalization in the control region, is smaller than the a priori normalization uncertainty). For large cancellations, the small 'shape' error is more sensitive to statistical fluctuations. The columns labeled "syst (up/down)" refer to the uncertainties derived from varying scale factors and expected events in the signal region due to: JES,JER,EER, and MMR. The column labeled "Gen(Alp vs Sherpa)" refers to the uncertainty derived from comparing background estimations using different W+jets MC generators (`Alpgen` versus `Sherpa`. As the `Sherpa` sample has no statistics for the highest $\sum p_T$ bins we assume a uniform value by considering only the bins with $\sum p_T < 1TeV$. The column labeled "Gen (MC@NLO vs Acer)" refers to the uncertainty obtained by comparing the background estimation

$\sum p_T$	EER (up/down) [%]	JES (up/down) [%]	JER [%]	EES (up/down) [%]
> 0.7	-5.0 / -1.1	-2.5/-3.8	-5.4	1.7 / -1.0
> 0.8	-1.3 / 2.5	-3.6/ -4.1	-5.5	-0.1 /-1.8
> 0.9	1.5 / -1.2	-1.6/ -8.2	4.0	-0.6/ -1.2
> 1.0	-0.4 / -0.5	-2.9/ -5.5	-4.6	-1.1 /-1.1
> 1.2	-1.3 / 3.7	-2.4/-11.4	-2.6	-2.5 / -2.3
> 1.5	-1.1 / -4.0	-7.5/-15.5	0.6	-3.4 / -0.03

Table 8.26: Residual uncertainty on combined W+jets/ttbar estimation, after normalization from control region in the electron channel.

$\sum p_T$	MMR (up/down) [%]	JES (up/down) [%]	JER
> 0.7	4.2 / 0.2	0.4 / 0.6	0.4
> 0.8	-5.0 / -0.7	3.5 / 2.0	-2.0
> 0.9	5.3 / 0.7	1.1 / 6.5	0.2
> 1.0	4.4 / -0.4	1.0 / -3.0	-1.8
> 1.2	-0.1 / -0.2	17.3/ -0.6	11.7
> 1.5	6.8 / 3.2	9.5 /11.1	-8.1

Table 8.27: Residual uncertainty on combined W+jets/ttbar estimation, after normalization from control region in the muon channel

using different $t\bar{t}$ MC generators (M@NLO or AcerMC). The column labeled "ISR/FSR" refers to the uncertainty derived by varying the $t\bar{t}$ final and initial state radiation and tabulating its effect on the final background estimation (see appendix H). The column labeled "pdf" refers to the uncertainty on the background estimation derived from PDF re-weighting in control and signal regions. Further details can be found in Appendix I. Finally, the last column is the total systematic uncertainty (sum in quadrature of the individual systematic uncertainties). The results with the final estimation of $W + jets/t\bar{t}$ in the signal region is presented in tables 8.30 and 8.31 for the muon and electron channel respectively.

Table 8.28: Summary of systematic background uncertainties for W+jets/$t\bar{t}$ due to JES,JER,EER,EES (maximum between up and down), MC generators, ISR/FSR and PDF re-weighting electron channel

$\sum p_T$	JES %	JER %	EER	EES	MC1 %	MC2 %	ISR/FSR	pdf%	Total%
>0.7 TeV	3.8	5.4	5.0	1.7	15	4.0	7.8	7.9	20.9
>0.8 TeV	4.1	5.5	2.5	1.8	15	0.24	7.6	7.6	19.9
>0.9 TeV	8.2	4.0	1.5	1.2	15	1.1	11.8	8.9	23.1
>1.0 TeV	5.5	4.6	0.5	1.1	15	6.0	11.0	11.1	23.6
>1.2 TeV	11.4	2.6	3.7	2.5	15	9.5	5.4	14.7	26.8
>1.5 TeV	15.5	0.6	4.0	3.4	15	18.2	11.0	24.1	39.1

Table 8.29: Summary of systematic background uncertainties for W+jets/$t\bar{t}$ due to JES,JER,MMR (maximum between up and down), MC generators, ISR/FSR and PDF re-weighting muon channel

$\sum p_T$	JES %	JER %	MMR %	MC1 %	MC2 %	ISR/FSR	pdf%	Total%
>0.7 TeV	0.6	0.4	4.2	13	8.4	5.8	5.9	18.1
>0.8 TeV	3.5	2.0	5.0	13	9.0	6.4	7.4	19.7
>0.9 TeV	6.5	0.4	5.3	13	9.0	7.8	10.2	22.0
>1.0 TeV	3.0	1.8	4.4	13	9.3	9.4	9.1	21.4
>1.2 TeV	17.3	11.7	0.2	13	23.0	8.7	11.0	36.5
>1.5 TeV	11.1	8.1	6.8	13	23.0	33.1	17.8	48.4

$\sum p_T$ (GeV)	W+jets/$t\bar{t}$ (MC)	SF	W+jets/$t\bar{t}$ (final)
> 700	$225 \pm 5 \pm 25$	$1.05 \pm 0.02 \pm 0.12$	$236 \pm 7 \pm 42.6$
> 800	$123 \pm 4 \pm 17$	$1.05 \pm 0.02 \pm 0.12$	$129 \pm 4 \pm 25.4$
> 900	$68 \pm 3 \pm 13$	$1.05 \pm 0.02 \pm 0.12$	$71 \pm 3 \pm 15.6$
> 1000	$37.0 \pm 2.1 \pm 5.9$	$1.05 \pm 0.02 \pm 0.12$	$38.9 \pm 2.3 \pm 8.3$
> 1200	$9.5 \pm 1.1 \pm 3.3$	$1.05 \pm 0.02 \pm 0.12$	$9.9 \pm 1.2 \pm 3.6$
> 1500	$2.14 \pm 0.51 \pm 0.50$	$1.05 \pm 0.02 \pm 0.12$	$2.2 \pm 0.5 \pm 1.1$

Table 8.30: Estimated combined W+jets and $t\bar{t}$ background in the signal region as a function of $\sum p_T$, in the muon channel, normalized according to the scale factor derived from the control region. The first quoted error is the statistical uncertainty, the second is the systematic. (Extrapolation uncertainties are not included on the pure MC estimate).

$\sum p_T$ (GeV)	W+jets/$t\bar{t}$ (MC)	SF	W+jets/$t\bar{t}$ (final)
> 700	$399 \pm 7 \pm 50$	$0.93 \pm 0.02 \pm 0.13$	$371 \pm 10 \pm 77.4$
> 800	$225 \pm 5 \pm 30$	$0.93 \pm 0.02 \pm 0.13$	$210 \pm 6 \pm 41.8$
> 900	$131 \pm 4 \pm 23$	$0.93 \pm 0.02 \pm 0.13$	$122 \pm 5 \pm 28.1$
> 1000	$78 \pm 3 \pm 11$	$0.93 \pm 0.02 \pm 0.13$	$73 \pm 3 \pm 17.2$
> 1200	$30.6 \pm 1.9 \pm 5.2$	$0.93 \pm 0.02 \pm 0.13$	$28.5 \pm 1.8 \pm 7.6$
> 1500	$6.7 \pm 0.9 \pm 2.4$	$0.93 \pm 0.02 \pm 0.13$	$6.3 \pm 0.8 \pm 2.5$

Table 8.31: Estimated combined W+jets and $t\bar{t}$ background in signal region as a function of $\sum p_T$, in the electron channel, normalized according to the scale factor derived from the control region. The first quoted error is the statistical uncertainty, the second is the systematic. (Extrapolation uncertainties are not included on the pure MC estimate).

Chapter 9

Background Estimation in SUSY di-lepton searches

Supersymmetry [39] (most commonly known as "SUSY") is one of the most exciting theories beyond the Standard Model, it predicts the existence of a new whole set of particles, one for each of the known particles in the Standard Model, with the property that those new particles differ by half a unit of spin compared with the ones in the SM, for instance in the case of quarks should exist a new group called squarks ($\tilde{q}$), for the gluons the gluinos ($\tilde{g}$) and so on. The dominant SUSY production channels at the LHC are: squark-(anti)squark, squark-gluino, and gluino pair production. The squarks and the gluinos are expected to decay into quarks and the SUSY partners of the gauge and Higgs bosons: charginos ($\tilde{\chi}^{\pm}$), and neutralinos ($\tilde{\chi}^{0}$), there are four neutralinos and two charginos.

9.1 Two lepton event production in SUSY cascade decay

SUSY events can produce charged leptons with high transverse momentum (p_T) through the decay of neutralinos and charginos. The main processes are: (a) $\tilde{\chi}_i^0 \to l^{\pm}\nu\tilde{\chi}_j^{\mp}$, (b) $\tilde{\chi}_i^{\pm} \to l^{\pm}\nu\tilde{\chi}_j^0$, (c) $\tilde{\chi}_i^0 \to l^{\pm}l^{\mp}\tilde{\chi}_j^0$, and (d) $\tilde{\chi}_i^{\pm} \to l^{\pm}l^{\mp}\tilde{\chi}_j^{\pm}$ where l is a: e, μ or τ lepton (where only e and μ are considered). The previous cascade decays could produce a final state with two leptons in the following ways:

- Two same-sign leptons (i.e. $\mu^-\mu^-$), in events in which two gauginos decay via cascade (a) or (b).
- Opposite sign leptons (i.e. $\mu^+\mu^-$), in events in which one gaugino decays via cascade (c) or (d).

For this analysis the ATLAS detector was used and the description is the same as presented in chapter 2. The reconstruction algorithms are also identical as described in chapter 4, and some of the Monte Carlo background samples described in chapter 5 are common for Black Holes and SUSY searches.

9.2 Background Topology

The opposite-sign (OS) and same-sign (SS) channels have quite different background composition, in the case of opposite sign the dominant backgrounds are: $t\bar{t}$, Z+jets, dibosons and single-top which are processes containing high-p_T well isolated leptons. For the SS channel the dominant background is coming from processes which contain "fake" leptons (here the term "fake" is related to processes which contain non-isolated leptons, mostly coming from semi-leptonic decay of b-quarks).

The signal regions for the two processes are quite similar, a high E_T^{miss} value is applied to reduce the SM backgrounds and different jet multiplicities scenarios are considered (2 jets, 4jets).

9.3 Background estimation in the OS channel

The background estimation in the OS channel is done in similar fashion to the methods described in sections 8.2 and 8.3, this is, a control region is constructed by using a set of cuts and aiming to have an enriched selection of events for certain background process, then, in that control region the ratio of events DATA/MC is measured and the resulting factor is used as a correction to the number of events in the signal region.

9.3.1 $t\bar{t}$ background

A control region for $t\bar{t}$ process is constructed by using a "top-tagging" algorithm. The top-tagging algorithm works through the use of a variable known as m_{CT} which is constructed using information from the four-vectors of the selected jets and leptons and is defined in the following way:

$$m_{CT}^2(\nu_1, \nu_2) = [E_T(\nu_1) + E_T(\nu_2)]^2 - [\mathbf{p_T}(\nu_1) - \mathbf{p_T}(\nu_2)]^2 \tag{9.1}$$

where ν_i can be a lepton (l), a jet (j), or a lepton-jet combination (jl), transverse momentum vectors are defined by p_T and transverse energies E_T are defined as $E_T = \sqrt{p_T^2 + m^2}$. The quantities $m_{CT}(j,j)$, $m_{CT}(l,l)$, $m_{CT}(jl,jl)$ are bounded from above by analytical functions of the top quark and W boson masses. A genuine top-tagged event should contain at least two jets with $p_T > 20$ GeV, and the scalar sum of the p_T of at least one combination of two jets and the two leptons in the event must exceed 100 GeV. Furthermore top-tagged events must have m_{CT} values consistent with expected bounds from $t\bar{t}$ events. After all requirements the ratio DATA/MC results in a value

compatible with unity, which means a good description of the Monte Carlo for this specific background.

9.3.2 $Z + jets$ background

For the $Z+jets$ background a control region is constructed with the following requirements:

- Only events with two leptons are selected
- A low missing transverse energy ($E_T^{miss} < 20$ GeV) value is required
- Invariant mass cut $81 < m_{ll} < 101$ GeV

In this control region the number of events observed in data are in good agreement with the MC expectations therefore the correction factor is also compatible with unity (within uncertainties).

9.3.3 Dibosons and single top

Since the contribution of these processes is quite small the prediction of events in the signal region is taken purely from MC without further correction from any control region. Following the background estimations techniques described above the resulting distributions for the OS channel are presented in Fig. 9.1

9.4 Background estimation in the SS channel

In the SS channel the main background comes from processes with "fake" leptons, as already mentioned above by "fake" we mean a lepton coming from the semi-leptonic decay of a b-quark, such as those in $b\bar{b}$ processes, this background has to be estimated purely from data since most likely the Monte Carlo description is wrong or the MC statistic in the signal region is not enough for this process. The method used is the "matrix" method (same as the method used for the QCD background in Black Hole analysis, section 8.1). The "fake" lepton samples for electron and muon channels are constructed by using a "loose" identification criteria for the particles, in the case of the muon channel the selection is identical to the one in the signal region, except the isolation requirement is dropped. For the electron channel the quality criteria is lowered to "medium", in addition a low value of missing transverse energy is required (as for the Black Hole analysis). this is $E_{miss}^T < 30$ GeV (same for both electron and muon channel). The "real" lepton samples are constructed

identical to the prescriptions in chapter 8.1. Once the "fake" and "real" leptons control regions are defined the system of equations is solved and the estimation for events with "fake" leptons in the signal region is obtained.

The resulting plots after background estimation for the SS channel is presented in Fig. 9.2

9.5 Systematics

The sources of systematics for this SUSY search is similar to the sources for Black Hole analysis presented in chapter 6, this is, the Jet Energy scale, Jet Energy resolution, MC modelling, lepton identification, control region selection, etc.

Given the good agreement of the expected SM backgrounds and the observed data (evident in Figs. 9.1 and 9.2) after the corrections from control regions, the conclusion is that in 1.04fb^{-1} of data analyzed in a di-lepton final state there is no indication of any SUSY signal [40]. This chapter also illustrates how the Background estimation techniques in different beyond the Standard Model searches can be shared as in the case of SUSY and Black Holes.

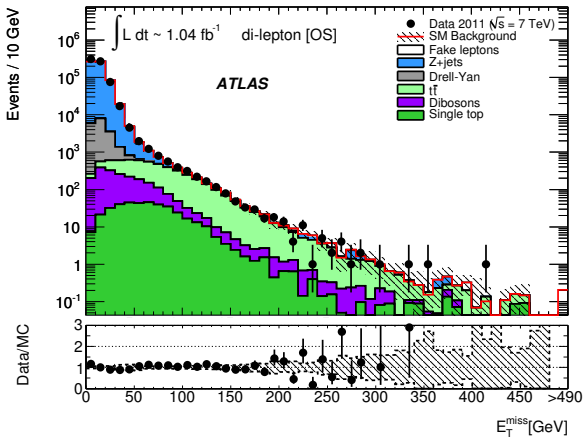

(a) The E_T^{miss} distributions of OS dilepton events before any jet requirement

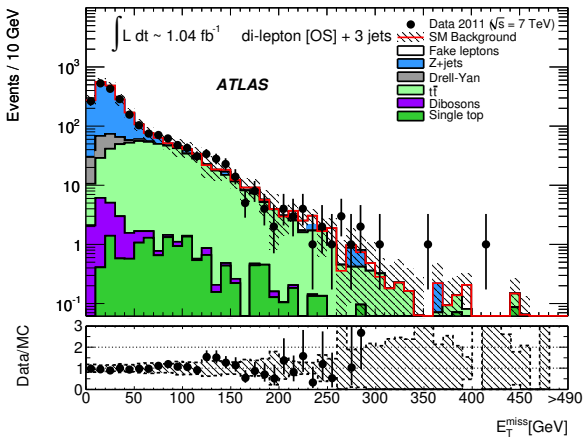

(b) The E_T^{miss} distributions of OS dilepton events after requiring 3 high-p_T jets

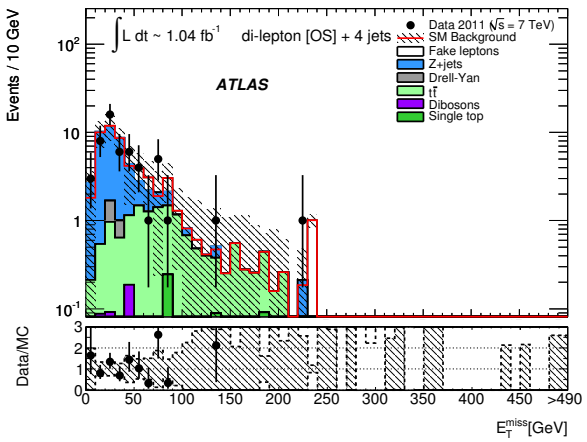

(c) The E_T^{miss} distributions of OS dilepton events after requiring 4 high-p_T jets

Figure 9.1: The E_T^{miss} distributions of OS dilepton events, the error band on the SM background represent the total uncertainty.

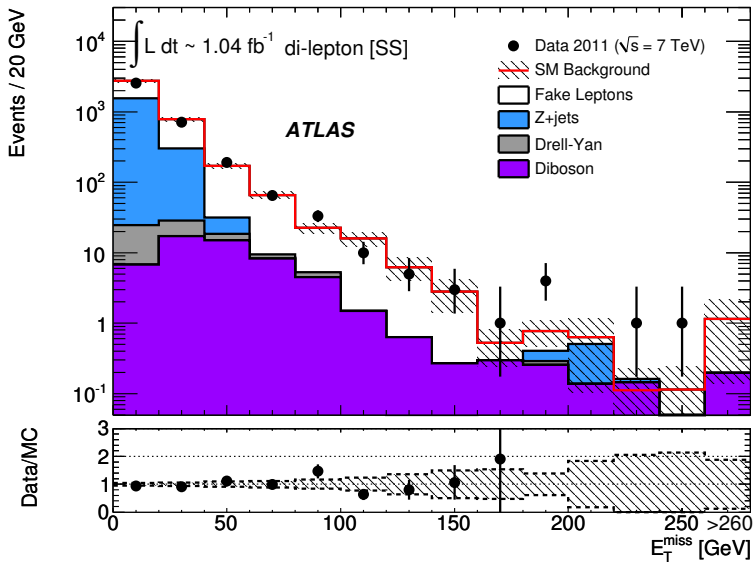

(a) The E_T^{miss} distributions of SS dilepton events before any jet requirement

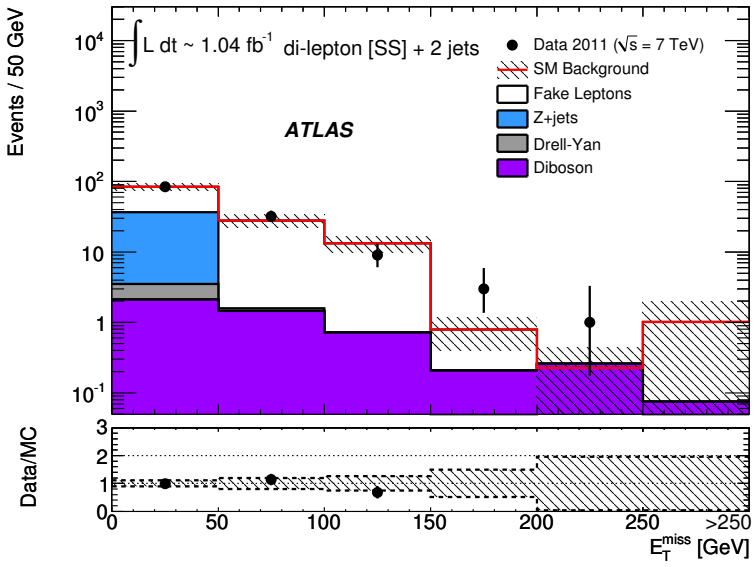

(b) The E_T^{miss} distributions of SS dilepton events after requiring two high-p_T jets

Figure 9.2: The E_T^{miss} distributions of SS dilepton events, the error band on the SM background represent the total uncertainty.

Chapter 10

Results and Interpretations

10.1 Event yield and distributions

The observed and predicted event yields, following the estimations described in chapter 8, are given in Tables 10.1 and 10.2 for electron and muon channels respectively, as a function of minimum $\sum p_T$ cut.

The agreement between the data and the background model expectation is good, and the distribution of $\sum p_T$ is shown in Fig. 10.1. The distribution of p_T of the object with the highest value of p_T is shown in Fig. 10.2. No evidence of a signal is observed, with SM background estimates in good agreement with the observed data, for all choices of $\sum p_T$ threshold, more distributions in the signal region are presented in appendix K. In Appendix J it is shown an event display of one of the events in our signal region with the highest-p_T value and also high multiplicity of objects (lepton and jets).

$\sum p_T$ (GeV)	QCD	W+jets/$t\bar{t}$	Z+jets	Total SM	Data
> 700	$137 \pm 10 \pm 45$	$371 \pm 10 \pm 77$	$119 \pm 4 \pm 22$	$627 \pm 15 \pm 92$	586
> 800	$75 \pm 7 \pm 25$	$210 \pm 6 \pm 42$	$74 \pm 4 \pm 13$	$358 \pm 10 \pm 51$	348
> 900	$42 \pm 5 \pm 14$	$122 \pm 5 \pm 28$	$46.9 \pm 2.8 \pm 8.6$	$210 \pm 8 \pm 33$	196
> 1000	$24.6 \pm 4.2 \pm 8.0$	$73 \pm 3 \pm 17$	$22.2 \pm 1.8 \pm 4.5$	$119 \pm 5 \pm 20$	113
> 1200	$8.1 \pm 2.5 \pm 2.7$	$28.5 \pm 1.8 \pm 7.6$	$9.1 \pm 1.0 \pm 1.9$	$45.7 \pm 3.2 \pm 8.3$	41
> 1500	$1.3 \pm 1.1 \pm 0.4$	$6.3 \pm 0.8 \pm 2.5$	$2.6 \pm 0.5 \pm 0.5$	$10.2 \pm 1.4 \pm 2.6$	8

Table 10.1: Background estimation summary as a function of $\sum p_T$ in the electron channel, using the methods described in chapter 8. The first quoted errors are statistical, the second systematic. All other backgrounds considered (WW, ZZ and WZ) are estimated to have negligible contributions.

$\sum p_T$ (GeV)	W+jets/$t\bar{t}$	Z+jets	Total SM	Data
> 700	$236 \pm 7 \pm 43$	$49 \pm 3 \pm 11$	$285 \pm 8 \pm 44$	241
> 800	$129 \pm 4 \pm 25$	$32.0 \pm 2.4 \pm 7.5$	$161 \pm 5 \pm 26$	145
> 900	$71 \pm 3 \pm 16$	$19.5 \pm 1.7 \pm 5.0$	$91 \pm 3 \pm 16$	78
> 1000	$38.9 \pm 2.3 \pm 8.3$	$13.1 \pm 1.3 \pm 3.1$	$52.0 \pm 2.6 \pm 8.9$	46
> 1200	$9.9 \pm 1.2 \pm 3.6$	$4.0 \pm 0.6 \pm 1.2$	$14.0 \pm 1.3 \pm 3.8$	15
> 1500	$2.2 \pm 0.5 \pm 1.1$	$0.6 \pm 0.2 \pm 0.4$	$2.8 \pm 0.5 \pm 1.1$	2

Table 10.2: Background estimation summary as a function of $\sum p_T$ in the muon channel, using the methods described in chapter 8. The first quoted errors are statistical, the second systematic. All other backgrounds considered (WW, ZZ, WZ and QCD multi-jet processes) are estimated to have negligible contributions.

10.2 Model Independent limits

No excess is observed beyond the Standard Model expectation; *p-values* for the signal regions are in the range 0.43 – 0.47[1]. Therefore, model-independent exclusion limits are determined on the fiducial cross section for non-SM production of these final states, $\sigma(pp \to \ell X)$, as a function of minimum $\sum p_T$.

The translation from an upper limit on this number of events to a fiducial cross section requires knowledge of the mapping (or equivalently, the selection efficiency), $\varepsilon_{\text{selection}}$, from the true signal production to that reconstructed, in the true fiducial region.

The true fiducial region for the electron (muon) channel is defined by the events with true final states passing these requirements: the leading lepton is an prompt electron (muon) within experimental acceptance, with $p_T > 100$ GeV, separated from jets formed at hadron level with $p_T > 20$ GeV by ΔR(lepton,jet)< 0.4, at least two additional isolated leptons or jets with $p_T > 100$ GeV and truth-level $\sum p_T$ above the respective signal region threshold. True jets are defined using the anti-k_T algorithm with R=0.4 on stable particles.

For the models considered, $\varepsilon_{\text{selection}}$ varies, and averages 74% for the electron channel, and 51% for the muon channel. The full range of $\varepsilon_{\text{selection}}$ is 60–90% for the electron channel and 40–60% for the muon channel.

Under the assumption of equal *a priori* signal model production of e and

[1] *p-values* close to zero excludes the Standard Model hypothesis, *p-values* close to one indicate that the variable measured in data is consistent with the Standard Model (see Apendix F)

μ, a combined limit can be also be calculated: this is a limit on the fiducial cross section for all final states with at least one lepton (e *or* μ), for which the $\varepsilon_{\text{selection}}$ averages 64%, with a range from 53 – 74%.

For the derivation of the upper limits on the fiducial cross section, the lowest observed acceptance for each channel is used, for all mass bins. The corresponding observed and expected upper limits on the fiducial cross-section $\sigma(pp \to \ell X)$, at 95% confidence level are displayed in Images 10.3, 10.4 and Table 10.3. These exclusion regions are obtained using the CL_s prescription described in App. G.

$\sum p_T$	$\sigma(pp \to \ell X)$ 95% C.L. Upper Limit (fb) Observed (Expected)		
(GeV)	Muon Channel	Electron Channel	Channels Combined
> 700	166 (233)	282 (323)	448 (536)
> 800	117 (145)	179 (186)	279 (317)
> 900	72.6 (92.8)	108 (125)	173 (202)
> 1000	48.2 (58.2)	70.9 (78.5)	107 (124)
> 1200	31.0 (28.5)	33.5 (38.0)	51.0 (56.8)
> 1500	11.0 (12.3)	12.8 (15.4)	16.7 (20.4)

Table 10.3: Expected and observed 95% C.L. upper limits on the fiducial cross sections $\sigma(pp \to \ell X)$ for the production of final states with at least 3 objects above a 100 GeV p_T cut including at least one isolated lepton, and $\sum p_T$ above threshold, for muon and electron channels separately, and for their combination (where $l = e$ or μ).The CL_s method is used to obtain the limits.

The observed limits are slightly smaller for the muon channel due to the lower acceptance, because of the lower trigger efficiency and the more stringent requirements needed to guarantee the best possible muon resolution at high-p_T .

For the models considered, the total signal acceptance is highly model-dependent, driven primarily by the fraction of events containing a lepton in the final states, and averages about 10% and 5% for the (mutually exclusive) electron and muon channels respectively. It is lowest for the low multiplicity, low mass states (small values of M_{TH}/M_D, or M_{TH} and M_D) that are theoretically or experimentally disfavoured.

10.3 Limits for benchmark models

The observed counts of data events in the signal region (for $\sum p_T > 1500$ GeV) along with the background expectations are used to obtain exclusion contours in the plane of M_D (M_D refers to the Planck scale in extra-dimensions $M_{Pl(4+n)}$) and M_{TH} (Mass threshold of the Black Hole) for several benchmark models (rotating and non-rotating black holes or string balls) that are considered representative of the gravitational states to which this analysis has sensitivity. No theoretical uncertainty on signal prediction is assessed; that is, the exclusion limits are set for the exact benchmark models as implemented in the `Blackmax` and `Charybdis` generators. Experimental systematic and luminosity uncertainties, along with the larger statistical error on the signal acceptances, are included in deriving the exclusion contours, and are found to be less than 10%. Some of the theoretical uncertainties comes from the effects of rotation, or spin. One of the more significant theoretical uncertainties is that associated with the decay of the state as its mass approaches M_D. Common prescriptions are to assume thermal emissions as the mass falls below M_D, all the way down to complete evaporation, or to end thermal emissions at some mass close to M_D, at which point the state decays immediately to a remnant state, the multiplicity of which is uncertain. The efficiency of the event selection in analyses could differ significantly according to the remnant model choice, particularly for samples in which a limited number of Hawking emissions are anticipated, motivating the consideration of multiple remnant models.

The 95% exclusion contours in the M_D-M_{TH} plane (M_S-M_{TH} plane for string balls) for different models are obtained using the CL_s prescription (see Appendix G). Fig. 10.5 shows exclusion contours for rotating black hole benchmark models with high- and low-multiplicity remnant decays. Their comparison allows an assessment of the effect of this modelling uncertainty on the analysis, which is inevitably greatest in the regime of low M_{TH}/M_D. Limits for rotating and non-rotating string ball models are shown in Fig. 10.6. The string ball models illustrated were simulated using a high-multiplicity remnant model.

A comparison between the limits obtained in the Lepton plus jets analysis and the alternative same-sign di-muon analysis for a Black Hole simulation with n=6 extra dimensions is presented in Appendix L, as seen there the limits are stringent for the lepton plus jets analysis.

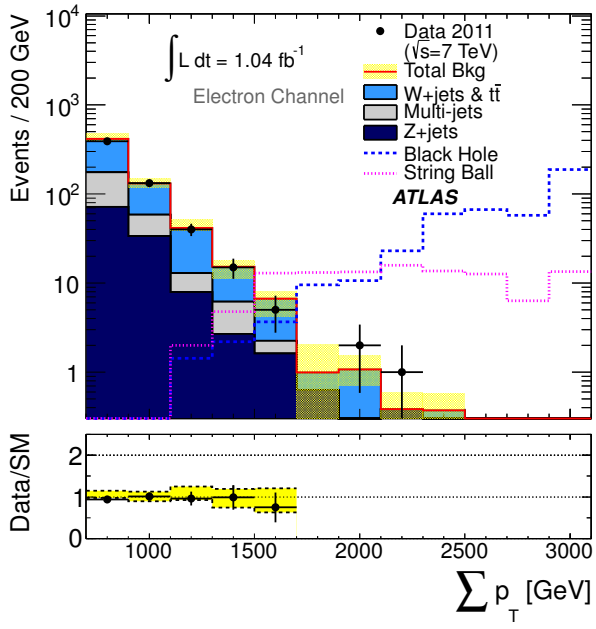

(a) Electron channel

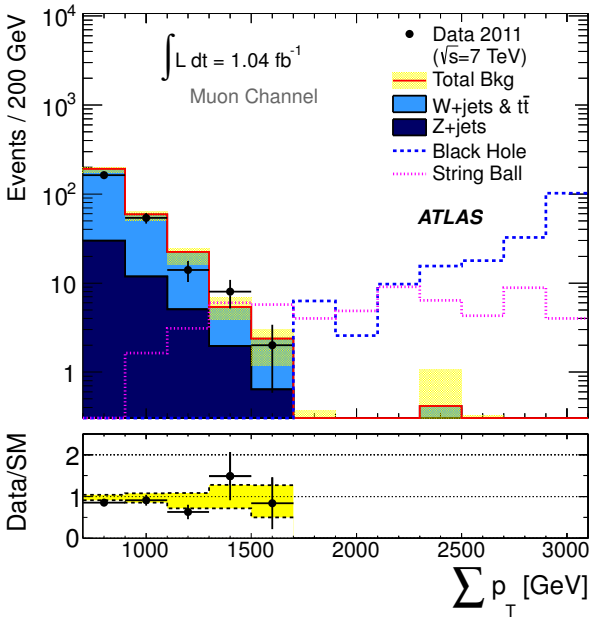

(b) Muon channel

Figure 10.1: Final $\sum p_T$ distributions for the signal region. Background processes are shown according to their data-derived estimates, as described in the text. The yellow band indicates the uncertainty on the expectation from finite statistics, jet and lepton energy scales and resolutions. Two representative signal distributions are overlaid for comparison purposes. The signal labelled "Black Hole" is a non-rotating black hole sample with $n = 6$, $M_D = 0.8$ TeV and $M_{TH} = 4$ TeV. The signal labelled "Stringball" is a rotating string ball sample with $n = 6$, $M_D = 1.26$ TeV, $M_S = 1$ TeV and $M_{TH} = 3$ TeV. The last bin in the signal sample histograms is the integral of all events with $\sum p_T \geq 3300$ GeV.

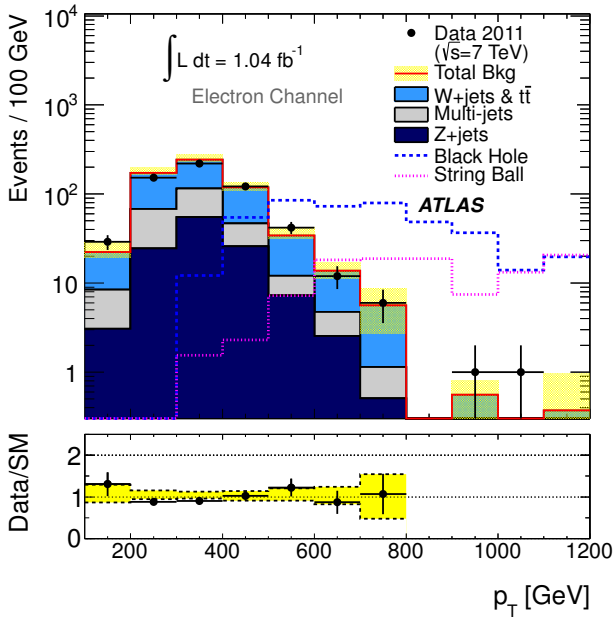

(a) Electron channel

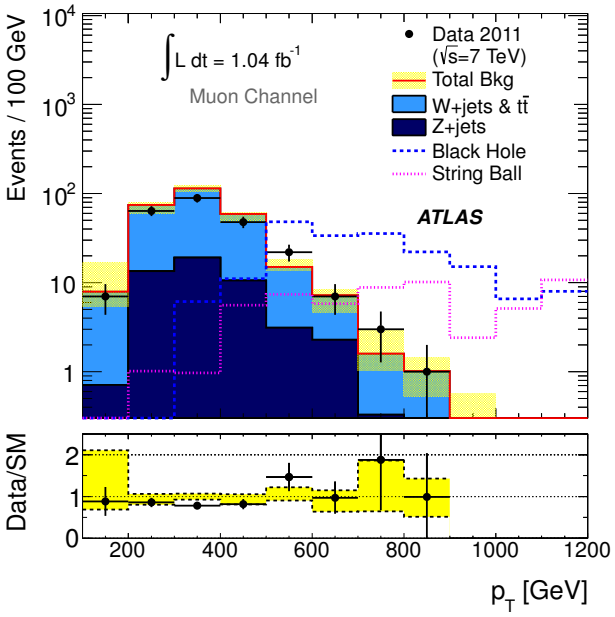

(b) Muon channel

Figure 10.2: Final distributions for p_T of the object (jet or lepton) with the largest value of p_T for the signal region. Background processes are shown according to their data-derived estimates, as described in the text. The yellow band indicates the uncertainty on the expectation from finite statistics, jet and lepton energy scales and resolutions. Two representative signal distributions are overlaid for comparison purposes. The signal labelled "Black Hole" is a non-rotating black hole sample with $n = 6$, $M_D = 0.8$ TeV and $M_{TH} = 4$ TeV. The signal labelled "Stringball" is a rotating string ball sample with $n = 6$, $M_D = 1.26$ TeV, $M_S = 1$ TeV and $M_{TH} = 3$ TeV. The last bin in the signal sample histograms is the integral of all events with $p_T \geq 1400$ GeV.

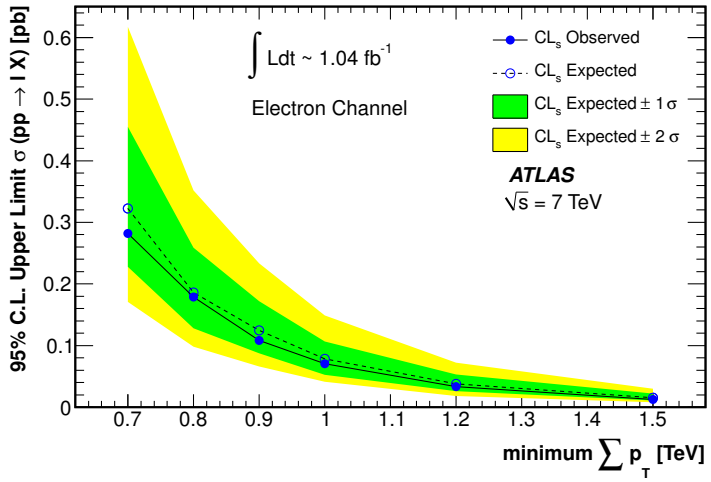

(a) Electron channel

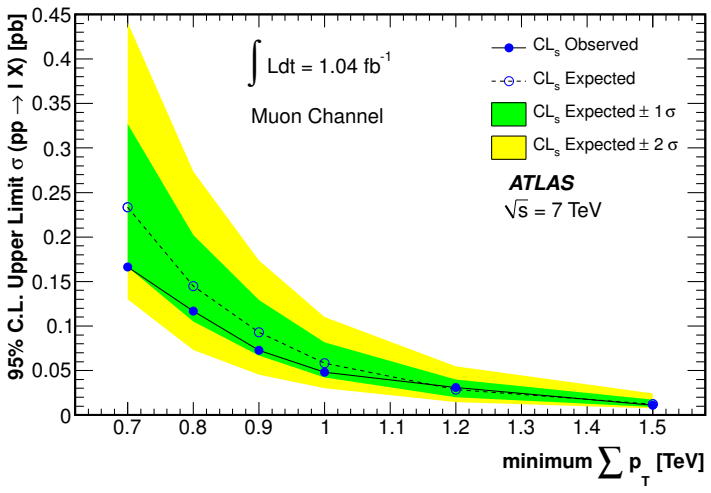

(b) Muon channel

Figure 10.3: 95% C.L. limits on the fiducial cross sections $\sigma(pp \to \ell X)$ for the production of final states with at least 3 objects above a 100 GeV p_T cut including at least one isolated lepton, and $\sum p_T$ above threshold. The observed and expected limits according to the CL_s prescription are shown, as well as the 1σ and 2σ bounds on the expected limit.

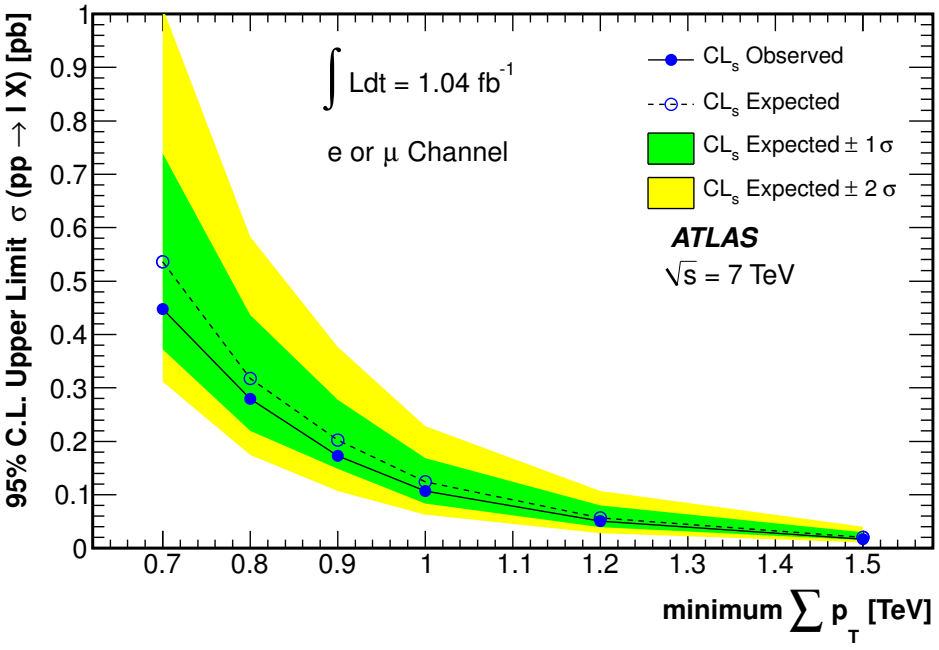

Figure 10.4: Limits on the fiducial cross sections $\sigma\,(pp \to \ell X)$ for the production of final states with at least 3 objects above a 100 GeV p_T cut including at least one isolated lepton, and $\sum p_T$ above threshold, for all final states with at least one electron or muon. The observed and expected 95% C.L. limits according to the $\mathrm{CL_s}$ prescription are shown, as well as the 1σ and 2σ bounds on the expected limit.

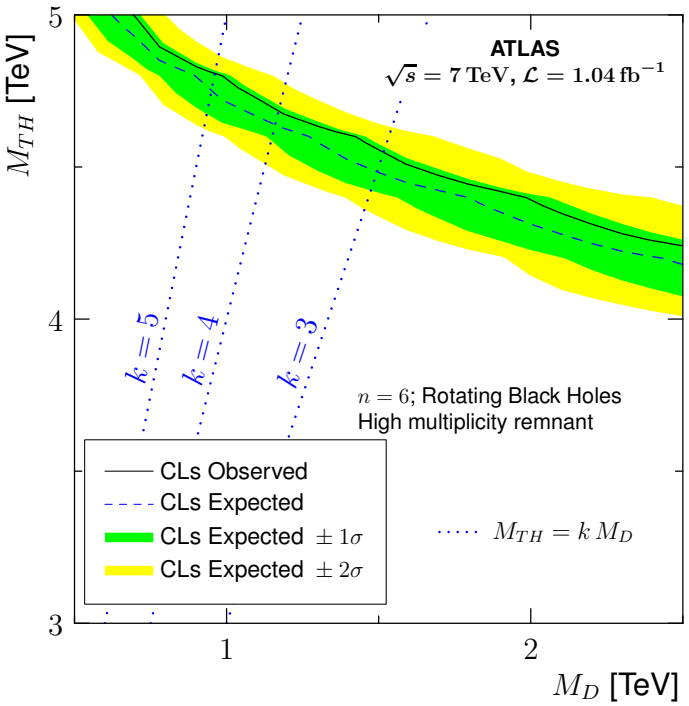

(a) Rotating black holes, with decays ending in a high-multiplicity remnant state, generated with `Blackmax`.

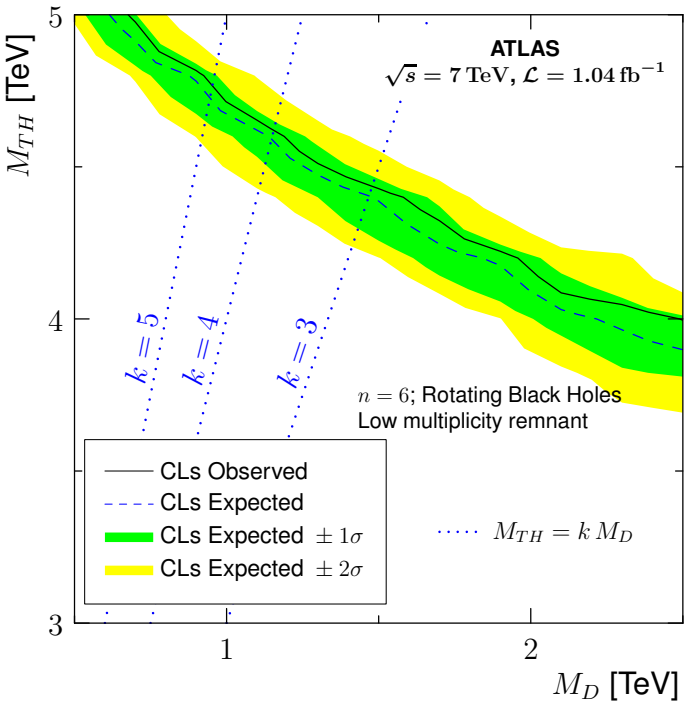

(b) Rotating black holes, with decays ending in a low-multiplicity remnant state, generated with `Charybdis`.

Figure 10.5: 95% C.L. limit in the M_{TH}-M_D plane, both channels combined, for a rotating black hole model with six extra dimensions. The solid (dashed) line shows the observed (expected) limits, with the green and yellow bands the expected 1σ and 2σ variations of the expected limits. The dotted blue lines show lines of constant $k = M_{TH}/M_D$. In this plots M_D refers to the Planck scale in extra-dimensions $M_{Pl(4+n)}$ and M_{TH} to the mass threshold of the Black Hole.

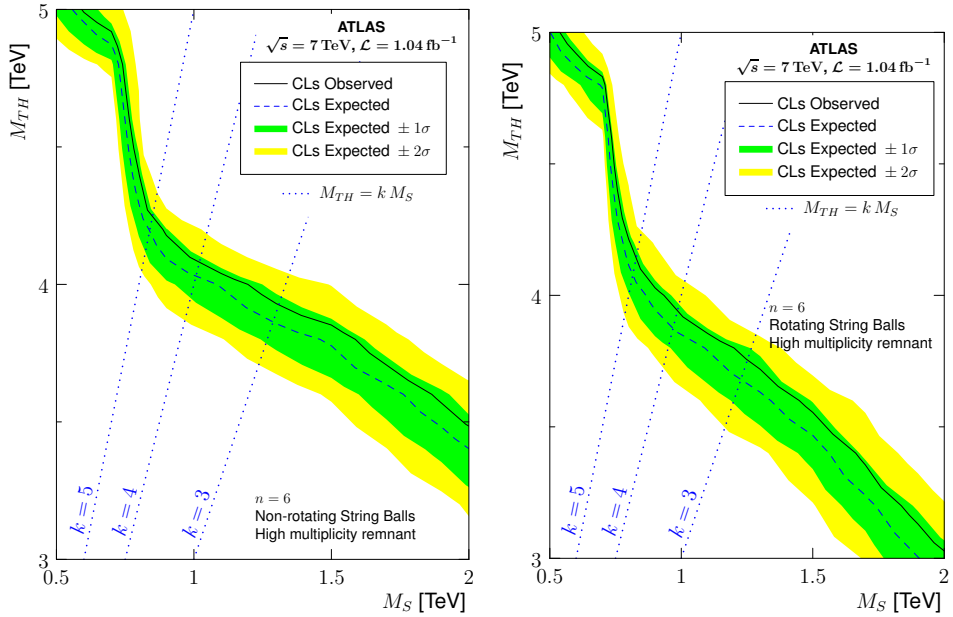

(a) Non-rotating string balls. (b) Rotating string balls.

Figure 10.6: 95% C.L. limit in the M_{TH}-M_D plane, both channels combined for rotating and non-rotating string balls with six extra dimensions. The solid (dashed) line shows the observed (expected) limits, with the green and yellow bands the expected 1σ and 2σ variations of the expected limits. The dotted blue lines show lines of constant $k = M_{TH}/M_D$. All samples were produced with the `Charybdis` generator.

Chapter 11
conclusions

The analysis described in this thesis correspond to a search for new physics beyond the Standard Model, looking for strong gravity effects at the TeV-scale and using models of extra dimensions this search was focused on microscopic Black Holes and String Ball states expected to be produced in proton-proton collisions at the LHC and detected by the ATLAS experiment, the data collected and analyzed correspond to a total integrated luminosity of 1.04 fb^{-1}. Along with previous analysis using different topologies this search has considered final states with three or more high transverse momentum objects, at least one of which was required to be a lepton (electron or muon). Special consideration was given to background modelling methods and the extrapolation from control to signal region with no deviation from the Standard Model observed in either the electron or the muon channels. Consequently, limits are set on TeV-scale gravity models, interpreted in a two-dimensional parameter grid of benchmark models (the $M_{Pl(4+n)}$-M_{TH} plane). Upper limits, at 95% C.L., are set on the fiducial cross-sections for new physics production of high-$\sum p_T$ multi-object final states containing a high-p_T (> 100 GeV) isolated lepton inside experimental acceptance. For final states with $\sum p_T > 1.5$ TeV, a limit of 16.7 fb is placed.

One of the perspectives for future updates to the analysis would be the improvement in the quantity of statistical data. For the year 2012 the LHC expects to produce around 20 fb^{-1} of integrated luminosity at a center of mass energy collision of 8 TeV, twenty times bigger statistic than the one used for the present analysis, the later will allow us to reach a wider energy range, and in the case of no signal detected, the possibility to extend the exclusion limits (over the higher-dimensional Planck scale $M_{Pl(4+n)}$). Another important improvement would be the reduction of the systematic uncertainties, the most important source of uncertainty in this analysis is the one related to the correct measurement of the Jet Energy (Jet Energy Scale), by finding new ways to constrain this uncertainty more accurate measurements could be reported.

In addition to the Black Hole, a search for Supersymmetry signal was presented in a final state with two leptons, background modelling methods were discussed and compared with those ones used in the Black Hole analysis, after applying corrections from control regions a good agreement between SM

expectations and data is observed excluding any evidence for SUSY signals in 1.04 fb^{-1} of data analyzed as reported in recent publication [40]

Appendix A

Monte Carlo Datasets

A.1 Background Monte Carlo Datasets

ID	Process	Cross-section [pb]
113129	NjetsNp2_J1x	297000000.0
113130	NjetsNp2_J2	13800000.0
113131	NjetsNp2_J3	424803.0
113132	NjetsNp2_J4	10787.6
113133	NjetsNp2_J5	216.184
113134	NjetsNp2_J6p	2.86
113135	NjetsNp3_J1x	16800000.0
113136	NjetsNp3_J2	10900000.0
113137	NjetsNp3_J3	766004.0
113138	NjetsNp3_J4	27041.0
113139	NjetsNp3_J5	656.0
113140	NjetsNp3_J6p	9.78
113141	NjetsNp4_J1x	1920000.0
113142	NjetsNp4_J2	2350000.0
113143	NjetsNp4_J3	441244.0
113144	NjetsNp4_J4	25468.6
113145	NjetsNp4_J5	826.57
113146	NjetsNp4_J6p	12.64
113147	NjetsNp5_J1x	190916.0
113148	NjetsNp5_J2	49627.0
113149	NjetsNp5_J3	171713.0
113150	NjetsNp5_J4	15419.2
113151	NjetsNp5_J5	628.739
113152	NjetsNp5_J6p	11.0
113153	NjetsNp6_J1x	19553.6
113154	NjetsNp6_J2	102498.0
113155	NjetsNp6_J3	59525.2
113156	NjetsNp6_J4	9428.42
113157	NjetsNp6_J5	517.482
113158	NjetsNp6_J6p	10.11

Table A.1: QCD alpgen samples. Tag e600_s933_s946_r2215_r2260_p543.

ID	Process	Cross-section [pb]
113159	BBjetsNp0_J1x	1680000.0
113160	BBjetsNp0_J2	60602.0
113161	BBjetsNp0_J3	1973.62
113162	BBjetsNp0_J4	48.61
113163	BBjetsNp0_J5p	0.95
113164	BBjetsNp1_J1x	283001.0
113165	BBjetsNp1_J2	195409.0
113166	BBjetsNp1_J3	12564.2
113167	BBjetsNp1_J4	383.52
113168	BBjetsNp1_J5p	7.16
113169	BBjetsNp2_J1x	67350.8
113170	BBjetsNp2_J2	76440.6
113171	BBjetsNp2_J3	12911.0
113172	BBjetsNp2_J4	650.63
113173	BBjetsNp2_J5p	16.6
113174	BBjetsNp3_J1x	9478.47
113175	BBjetsNp3_J2	22753.1
113176	BBjetsNp3_J3	7101.22
113177	BBjetsNp3_J4	578.05
113178	BBjetsNp3_J5p	18.51
113179	BBjetsNp4_J1x	1329.8
113180	BBjetsNp4_J2	6564.0
113181	BBjetsNp4_J3	3808.0
113182	BBjetsNp4_J4	550.0
113183	BBjetsNp4_J5p	27.0

Table A.2: QCD alpgen $b\bar{b}$ samples. Tag e600_s933_s946_r2215_r2260_p543.

ID	Process	Cross-section [pb]
105009	J0_pythia_jetjet	9752970000.0
105010	J1_pythia_jetjet	673020000.0
105011	J2_pythia_jetjet	41194700.0
105012	J3_pythia_jetjet	2193250.0
105013	J4_pythia_jetjet	87848.7
105014	J5_pythia_jetjet	2328.56
105015	J6_pythia_jetjet	33.8461
105016	J7_pythia_jetjet	0.13741
105017	J8_pythia_jetjet	6.2789×10^{-6}

Table A.3: QCD pythia samples. Tag e574_s934_s946_r2213_r2260_p543.

ID	Process	Cross-section [pb]
107680	WenuNp0	6913.3×1.19887
107681	WenuNp1	1293.0×1.19887
107682	WenuNp2	377.1×1.19887
107683	WenuNp3	100.9×1.19887
107684	WenuNp4	25.3×1.19887
107685	WenuNp5	6.9×1.19887
107690	WmunuNp0	6913.3×1.19887
107691	WmunuNp1	1293.0×1.19887
107692	WmunuNp2	377.1×1.19887
107693	WmunuNp3	100.9×1.19887
107694	WmunuNp4	25.3×1.19887
107695	WmunuNp5	6.9×1.19887
107700	WtaunuNp0	6913.3×1.19887
107701	WtaunuNp1	1293.0×1.19887
107702	WtaunuNp2	377.1×1.19887
107703	WtaunuNp3	100.9×1.19887
107704	WtaunuNp4	25.3×1.19887
107705	WtaunuNp5	6.9×1.19887

Table A.4: W alpgen samples. Tag e760_s933_s946_r2215_r2260_p543.

ID	Process	Cross-section [pb]
107650	ZeeNp0	830.125
107651	ZeeNp1	166.2375
107652	ZeeNp2	50.2825
107653	ZeeNp3	13.9225
107654	ZeeNp4	3.615625
107655	ZeeNp5	0.9417875
107660	ZmumuNp0	830.125
107661	ZmumuNp1	166.2375
107662	ZmumuNp2	50.2825
107663	ZmumuNp3	13.9225
107664	ZmumuNp4	3.615625
107665	ZmumuNp5	0.9417875
107670	ZtautauNp0	830.125
107671	ZtautauNp1	166.2375
107672	ZtautauNp2	50.2825
107673	ZtautauNp3	13.9225
107674	ZtautauNp4	3.615625
107675	ZtautauNp5	0.9417875

Table A.5: Z alpgen samples. Tag e737_s933_s946_r2215_r2260_p543. A k-factor of 1.25 is already included in the cross-section for consistency with the NNLO values.

ID	Process	Cross-section [pb]
106280	WbbNp0	3.2×1.22
106281	WbbNp1	2.6×1.22
106182	WbbNp2	1.4×1.22
106183	WbbNp3	0.6×1.22

Table A.6: W + bb + jets alpgen samples. Tag e600_s933_s946_r2302_r2300_p575.

ID	Process	Cross-section [pb]
105985	WW_Herwig	25.59×0.388
105986	ZZ_Herwig	4.59×0.21
105987	WZ_Herwig	11.23×0.3084

Table A.7: Diboson Herwig samples. Tag e598_s933_s946_r2302_r2300_p575.

ID	Process	Cross-section [pb]
105200	T1_McAtNlo	160.79×0.556
105204	TTbarFullHad_McAtNlo	160.79×0.444
108340	st_tchan_enu	7.00
108341	st_tchan_munu	7.00
108342	st_tchan_taunu	7.00
108343	st_schan_enu	0.468
108344	st_schan_munu	0.468
108345	st_schan_taunu	0.468
108346	st_Wt_McAtNlo	13.00

Table A.8: Top quark MC@NLO samples. Tag e598_s933_s946_r2215_r2260_p543.

A.2 Signal Monte Carlo Datasets

Process	Rotating	Initial-State Graviton Rad.	Lepton number Conservation	Remnant Decay
PytBMx_BH1_BM_n#	no	no	no	final burst
PytBMx_BH2_BM_n#	yes	no	no	final burst
PytBMx_BH2_BM_c1_n#	yes	no	yes	final burst
CH2_BH1n#	no	no	no	⟨4⟩-body
CH2_BH2n#	yes	no	no	⟨4⟩-body
PytChr2_BH6_CH_n#	yes	no	no	⟨4⟩-body
CH2_BH21n#	no	no	no	2-body
CH2_SB1n6	no	no	no	⟨4⟩-body
CH2_SB2n6	yes	no	no	⟨4⟩-body
CH2_SB4n6	yes	yes	no	2-body

Table A.9: Signal samples. BlackMax (PytBMx), Charbydis (PytChar2, CH2), ⟨4⟩-body is Poisson distributed multiplicity with mean of four, and $n\#, \# = 2, 4, 6$. In these samples gravitons can only occur in pairs in the production phase.

Appendix B

The Atlas framework Athena

The ATLAS framework is called Athena, Athena is a control framework based on the GAUDI component architecture originally developed by LHCb, the Gaudi architecture object diagram is shown in figure B.1.

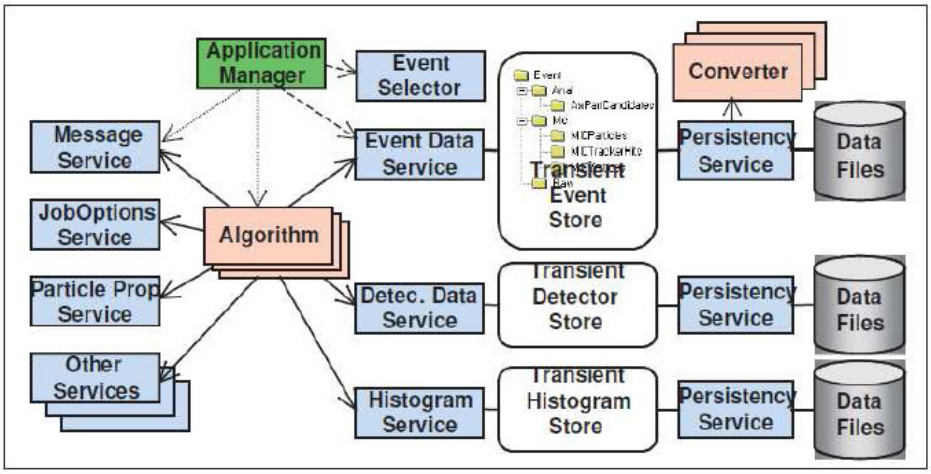

Figure B.1: Object diagram of the GAUDI Architecture

It consists of an application manager, services and algorithms. Services refer to classes whose job is to provide a set of facilities or utilities to be used by other components, e.g. algorithms. The functionality of an algorithm is to take input data, manipulate it and produce new output data. The algorithms included in Athena are almost exclusively written in C++. The framework model produces only one executable application. The other components produce shared libraries, which typically contain algorithms for data processing, or service for the algorithms. Scripts for the run time control of code execution are written in python. The algorithms are configured and sequenced at run time using job options interpreted by the core software. Three steps are performed in a standard Athena job:

- Initialization: Services and Algorithms loaded on demand

- Event Loop: Algorithms in list run sequentially on each event
- Finalization: Algorithms are terminated and objects are deleted

B.1 Integration of external generators in Athena

The Monte Carlo (MC) generator codes are developed independently of the experiments. To unify the access to the generator libraries the Generator Services project (GENSER) collaborates with the LHC experiments. GENSER provides validated LCG compliant code for both the theoretical and experimental communities at the LHC. In Athena the Configuration Management Tool (CMT) provides standard formalism to make these generator libraries available to be used in the framework. Those light-weight packages are called "glue" packages and mainly consist of one requirements file only. In addition an interface package is needed to provide the steering possibility and to actually call the generator routines. With these two extra packages per generator a default work-flow for a generator job in Athena can be drawn, as illustrated in figure B.2

1.- The Athena parameter and generator specific settings are passed to the interfaced package via the job options, 2.- During the initialization step the generator will be configured by the interface according to the settings in the job option. In the events loop the interface calls the generator and the event will be generated. 3.- The generator returns the generated event back to the interface 4.- The interface stores the generated event in HepMC format in the transient store named Store-gate, 5.- Helper classes, e.g. GeneratorFilter and TruthTools, get the HepMC container form the transient store, modify the event according to the selected algorithms and write the modified event back into Store-gate. The event can also be skipped. Simulation and other downstream processing steps will also access the HepMC container via Store-Gate 6.- The events can be read out of Store-gate, converted to a root-style format and written out to a persistent store, namely an output file

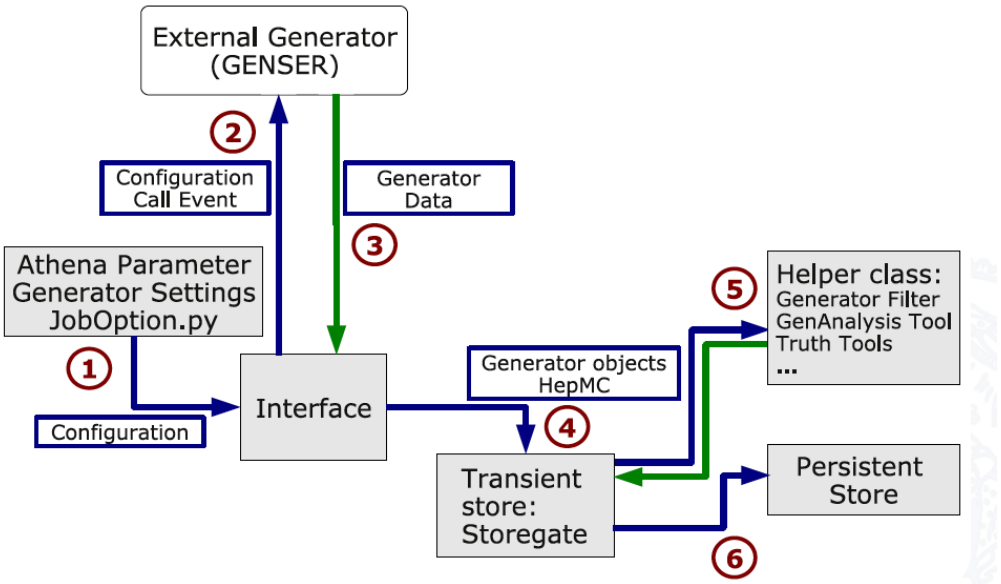

Figure B.2: Default workflow for generators in Athena

Appendix C

Distributions After Pre-selection

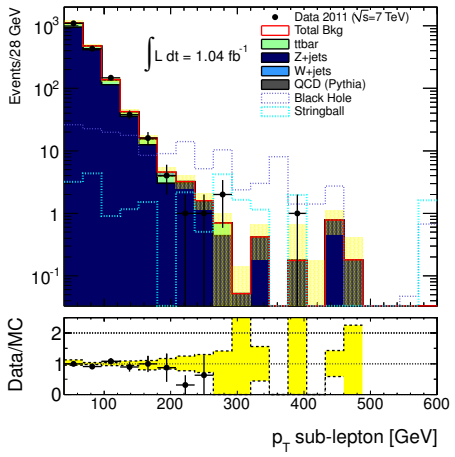

(a) Transverse momentum of sub-leading electron.

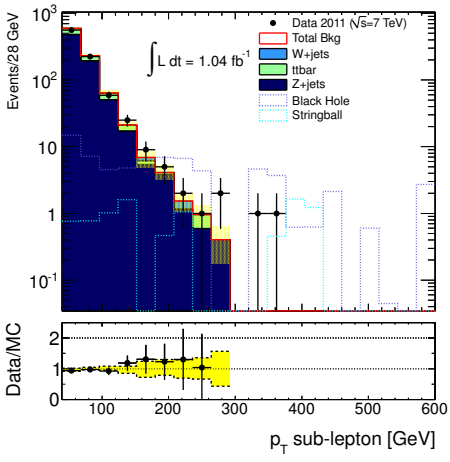

(b) Transverse momentum of sub-leading muon.

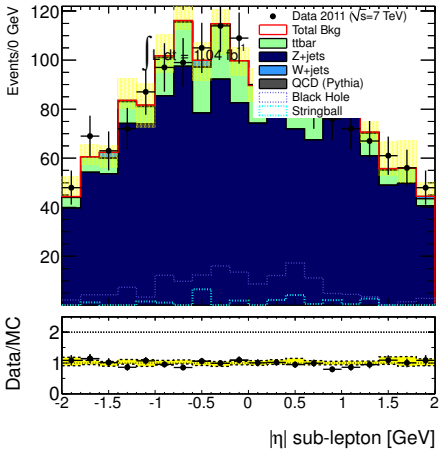

(c) Pseudo rapidity of sub-leading electron.

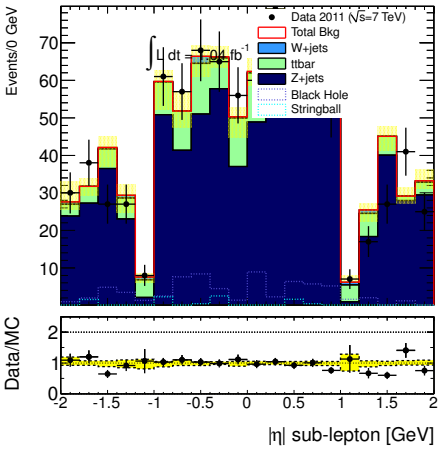

(d) Pseudo rapidity of sub-leading muon.

Figure C.1: Transverse momentum and pseudo-rapidity of sub-leading lepton after pre-selection. The Monte Carlo samples are normalized by their cross-section to 1.04 fb^{-1}.

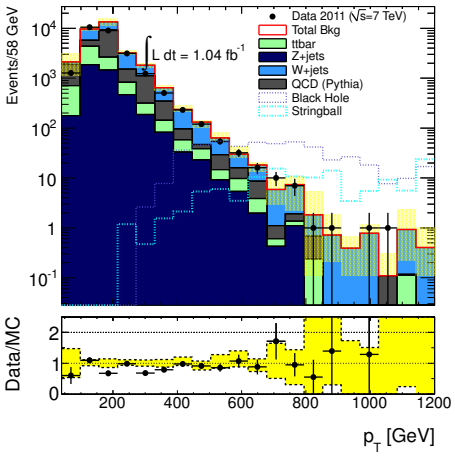

(a) Transverse momentum of leading object in electron events.

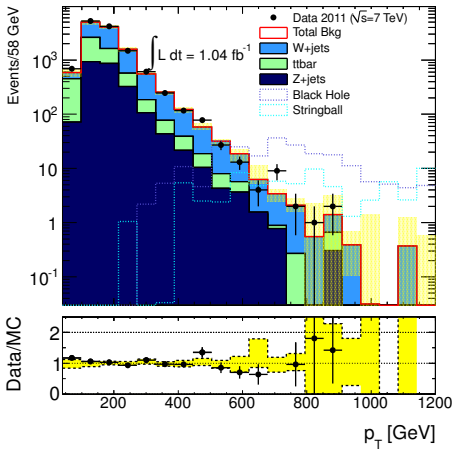

(b) Transverse momentum of leading object in muon events.

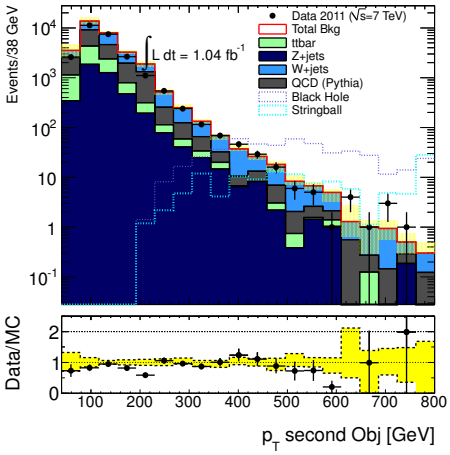

(c) Transverse momentum of second leading object in electron events.

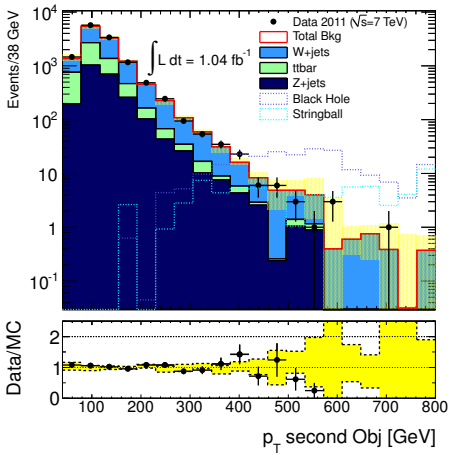

(d) Transverse momentum of second leading object in muon events.

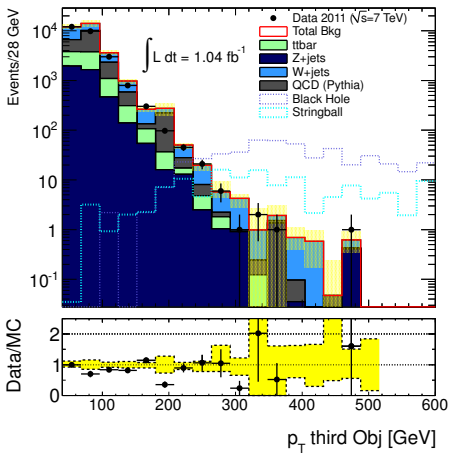

(e) Transverse momentum of third leading object in electron events.

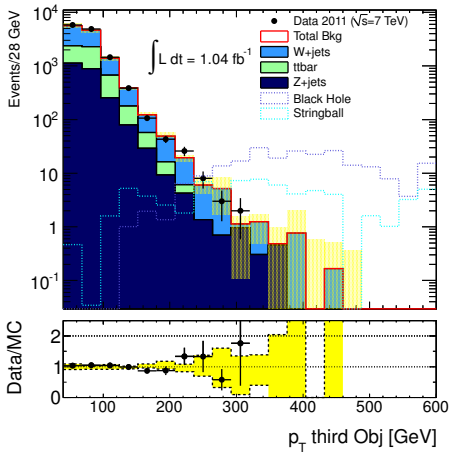

(f) Transverse momentum of third leading object in muon events.

Figure C.2: Transverse momentum of the three most leading objects after pre-selection. The Monte Carlo samples are normalized by their cross-section to 1.04 fb^{-1}.

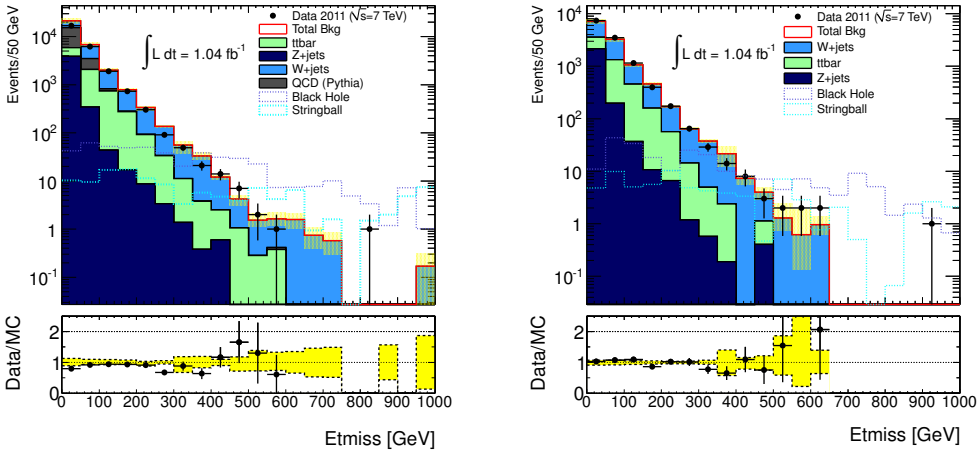

(a) Missing transverse energy in electron events.

(b) Missing transverse energy in muon events.

Figure C.3: Missing transverse energy in events after pre-selection. The yellow error band shows the full (statistical and systematic) error. The Monte Carlo samples are normalized by their cross-section to 1.04 fb^{-1}.

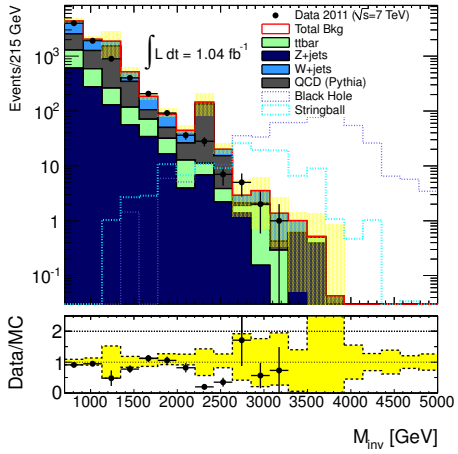

(a) Invariant mass of electron events.

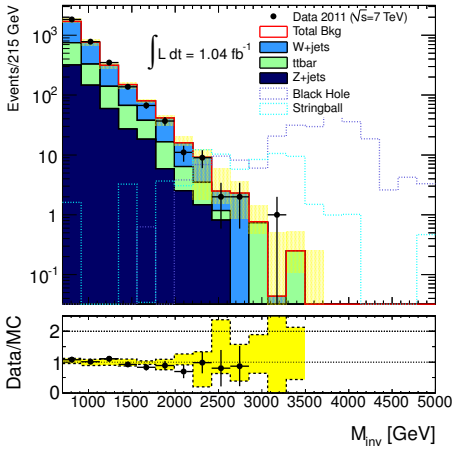

(b) Invariant mass of muon events.

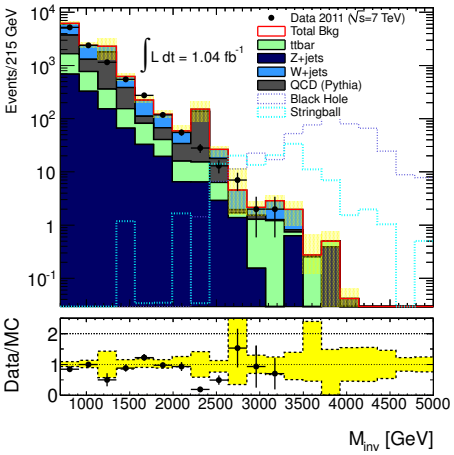

(c) Invariant mass including missing transverse energy of electron events.

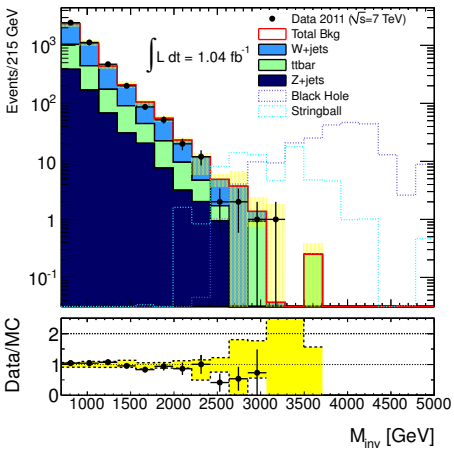

(d) Invariant mass including missing transverse energy of muon events.

Figure C.4: Invariant mass of events after pre-selection. The yellow error band shows the full (statistical and systematic) error. The Monte Carlo samples are normalized by their cross-section to 1.04 fb^{-1}.

Appendix D

Loose Jet cleaning

Bad jets are jets not associated to real energy deposits in the calorimeters. They arise from various sources, ranging from hardware problems (HEC spike, EM coherent, ...), LHC beams conditions, and cosmic-ray showers. Several sets of cuts are provided to identify such jets, the bad jet definition is based on the following variables:

- emf: electromagnetic fraction
- fmax: maximum energy fraction in one calorimeter layer
- HECf: energy fraction in the HEC
- Q: jet quality is the fraction of energy corresponding to LAr cells with a cell Q-factor greater than 4000. The cell Q-factor measures the difference between the measured pulse shape (a_i^{meas}) and the predicted pulse shape (a_i^{pred}) that is used to reconstruct the cell energy. It is computed as $\sum_{samples}(a_i^{meas} - a_i^{pred})^2$ and it is stored as 16-bit integer.
- HECq: same as the LArQuality except calculated only with HEC
- NegativeE: negative energy in the jet.
- t: jet time computed as the energy squared cells mean time
- AverageLArQF: jet quality computed as the energy squared cell mean quality
- qmean: normalized jet quality computed as the energy squared cells mean quality (qmean=AverageLArQF/65335)
- n90: minimum number of cells containing at least 90% of the jet energy
- eta: is the eta at the emscale.
- chf: is the charged fraction. It is the ratio of the sum pt of tracks (sumPtTrk) associated to the jets divided by the CALIBRATED jet pt. In rel15 data, sumPtTrk can be computed from AOD using the JetVertexAssociationTool. In rel16 data, this variable is stored as a jet moment called sumPtTrk.

	Loose	Medium = Loose OR	***under discussion*** Tight = Medium OR
HEC spikes	HECf>0.5 && |HECQ|>0.5 or |neg. E|>60GeV	HECf>1-|HECQ|	
EM coherent noise	EMf>0.95 &&|LArQ|>0.8 && |eta|<2.8	EMf>0.9 && |LArQ|>0.8 && |eta|<2.8	|LArQ|>0.95 or EMf>0.98 && |LArQ|>0.05
Non-collision background & Cosmics	|t|>25ns or EMf<0.05 && Chf<0.05 && |eta|<2 or EMf<0.05 && |eta|>=2 or FMax>0.99 && |eta|<2	|t|>10ns or EMf<0.05 && Chf<0.1 && |eta|<2 or EMf>0.95 && Chf<0.05 && |eta|<2	EMf<0.1 && Chf<0.2 && |eta|<2 or EMf<0.1 && |eta|>=2 or EMf>0.9 && Chf<0.02 && |eta|<2

Figure D.1: Definition of loose, medium or tight jet selections

Appendix E

QCD Estimation in the Muon Channel (ABCD Method)

We expect a negligible contribution of QCD processes in the muon channel, as the muon quality cuts (including the overlap removal with jets and muon ptcone isolation (see Section 7.1) and the high muon p_{T} requirement are highly effective in removing the QCD background in our signal region. Unlike the electron case, there is no contribution from jets faking a muon through calorimeter energy deposits. We also observe zero QCD events in the various control regions (W+jets/$t\bar{t}$, Z+jets), wherein the muon p_{T} threshold is lowered substantially from 100 to 40 GeV and $\sum p_T < 700$ GeV. We therefore conclude that this background has a negligible contribution in the signal region. In order to obtain an estimation directly from data we make use of the ABCD method which defines four different regions based on two uncorrelated variables; in this case we use ptcone relative isolation ($Risol30$) and $\sum p_T$. Each of the four regions is defined such that, except for the signal region (region A), they are populated by QCD events. The regions are defined as follows.

- Region A (Signal region): characterized by events with isolated muons and high $\sum p_T$ (*i.e.* $\sum p_T > 700$ GeV).
- Region B (Control region 1): characterized by events with non-isolated muons and high $\sum p_T$ (*i.e.* $\sum p_T > 700$ GeV).
- Region C (Control region 2): characterized by events with isolated muons and low $\sum p_T$ (*i.e.* $\sum p_T < 700$ GeV).
- Region D (Control region 3): characterized by events with non-isolated muons and low $\sum p_T$ (*i.e.* $\sum p_T < 700$ GeV).

In order to allow that sufficient QCD events populate the different regions, we use a relaxed signal region definition in which we lower the p_{T} requirements on the muon and the two other leading objects: we just impose a 50 GeV cut for the muon and the nominal pre-selection 40 GeV cut for the other objects.

Table E.1: Background composition in regions A,B,C and D

Region	QCD	W+jets	Z+jets	ttbar	DATA
A	0	294.0 ± 6.0	60.3 ± 2.7	121.6 ± 3.1	484
B	2.0 ± 0.5	0.4 ± 0.2	0.6 ± 0.3	0.002 ± 0.0	6
C	6.6 ± 4.7	2811.0 ± 21.4	1279.8 ± 12.7	1014.0 ± 9.0	5223
D	74.3 ± 17.1	4.6 ± 0.8	2.5 ± 0.6	3.8 ± 0.5	225

Table E.2: QCD estimated events in signal region

$\sum p_T$ cut	Estimated QCD (DATA)	Estimated QCD (MC)
0.7	2.7 ± 2.2	0.17 ± 0.14
0.8	1.4 ± 1.3	0.11 ± 0.09
0.9	0.9 ± 0.9	0.08 ± 0.06
1.0	0.9 ± 0.9	(no stat)
1.2	0.5 ± 0.5	(no stat)
1.5	$< 0.5 \pm 0.5$	(no stat)

In addition, the muon isolation is relaxed from $Risol30 < 0.05$ to $Risol30 < 0.1$ (and the requirement for non-isolated muons is therefore $Risol30 > 0.1$).

In Table E.1 we present the background composition in each one of the four regions and compare with the observed events in data. Regions B and D are dominated by QCD processes (non-isolated muons), while region C has a large contamination from processes with real leptons (W+jets, $t\bar{t}$ and Z+jets). The contamination from events with real leptons in region C is subtracted, using MC estimates, from the observed events in data, to obtain the QCD component. Assuming the relation $\frac{A}{B} \sim \frac{C}{D}$ holds, the number of estimated QCD events from data in the signal region (A) is given by $QCD_{\text{estimated}}(A) = B \times \frac{C}{D}$. The results as a function of the $\sum p_T$ cut are presented in Table E.2. The estimation of the QCD background determined from the data in this way is consistent with zero (and the MC prediction). Given that here we are using a very relaxed signal region definition (see description above), this estimation should be considered conservative.

Appendix F

Statistical significance and the *p-value*

In particle physics analysis when a quantity "X" in data is measured (i.e. number of events after some selection, number of leptons, total energy of the final state particles, etc..), very often one tries to match this quantity with certain model which it is supposed to describe what we are looking at. It is a common practice to use "at least" two models, one model which is expected to fully describe our measurements and that has been tested before in previous experiments, lets call this model as H_0 (and this model will be recognized as the Standard Model), and a second model which includes the Standard Model plus a new process that hasn't been measured before in previous experiments and that postulates the existence of a new particle or force not seen before and certainly not included in H_0, such model will be referred as H_1. In the next lines a formal method will be introduced, which main motivation is to explain from a statistical point of view if our data is consistent either with model H_0 or H_1 and define a very useful variable known as the *p-value*.

First of all lets define some quantities:

- $f_0(X)$ and $f_1(X)$ which are probability distributions associated to H_0 and H_1 (usually Poisson distributions are used)
- critical region ω: hypothetical region such that if $X\ \varepsilon\ \omega$ then H_1 is true otherwise H_0 is true.

A graphical representation of the variables defined can be seen in Fig. F.1. Given the definition of the critical region there are four possible outcomes:

- X lies inside the critical region and H_1 is true, then we have chosen the correct hypothesis.
- X lies inside the critical region and H_1 is false, we have made a mistake (first type), and the probability for this to happen is $\int_{X\varepsilon w} f_0(X)dX = \alpha$, α is known as the "significance" of the test,
- X lies outside the critical region and H_0 is true, we have chosen the correct hypothesis.

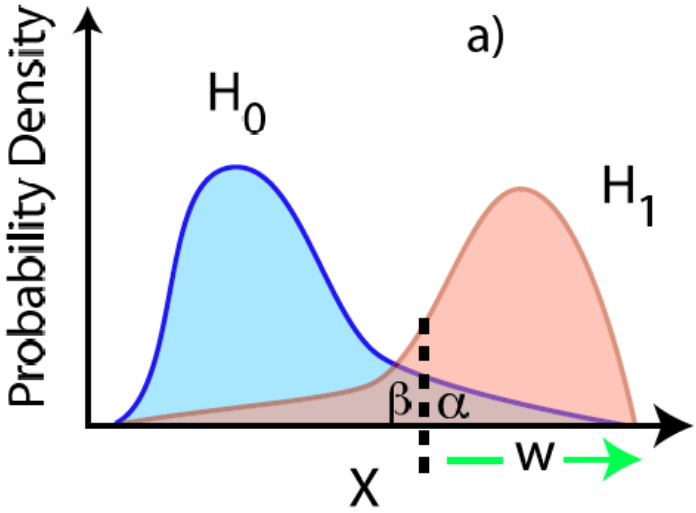

Figure F.1: Graphical representation of H_0, H_1, $f_0(x)$, $f_1(X)$ and the critical region ω.

- X lies outside the critical region and H_0 is false, we have made a mistake (second type), and the probability for this to happen is $\int_{X\varepsilon w} f_1(X)dX = \beta$, The probability $1-\beta$ is known as the "power" of the test.

In an optimal test one would like to choose X and the critical region ω such that α and β are as small as possible.

The previous formalism can be translated to a real experiment, lets not assume a critical region ω, but a value X_0 for the actual measurement, and lets assume we are expecting our data to more or less consistent with H_0, a measure of the consistency of the observed value X_0 with the hypothesis H_0 is the probability

$$\int_{X>X_0} f_0(X)dX \tag{F.1}$$

If then we define the critical region as $w = \{X|X > X_0\}$, the probability of observing a value X equal or greater than our observation. This probability is formally known as the p-value and has a number of good features:

- It only depends on the measurement (X_0) and the probability density for the hypothesis.
- It is not a hypothesis test.

- It only provides a measure of the consistency of the hypothesis and the measurement.

From definition a very small p-value is used to support the inference that the specific hypothesis should be rejected, for the analysis described in this thesis we found *p-values* in the range $0.43 - 0.47$, therefore we conclude our observation is consistent with the H_0 model (the Standard Model).

Appendix G

The CLs Method for limit setting

In this section a brief description of the method for setting upper limits is provided, it is known as CLs, it is one of the three methods for setting limits mentioned in the Review of Particle Physics by the PDG [41] and has been widely used in High Energy Physics in recent years.

Following the same notation as in Appendix F and assuming a test statistic "$X = q$" has been constructed to distinguish between hypothesis that the data contains signal and background (H_1) and that of background only (H_0), these corresponds to the distributions $f(q|s+b)$ and $f(q|b)$ respectively and are graphically presented in Fig. G.1.

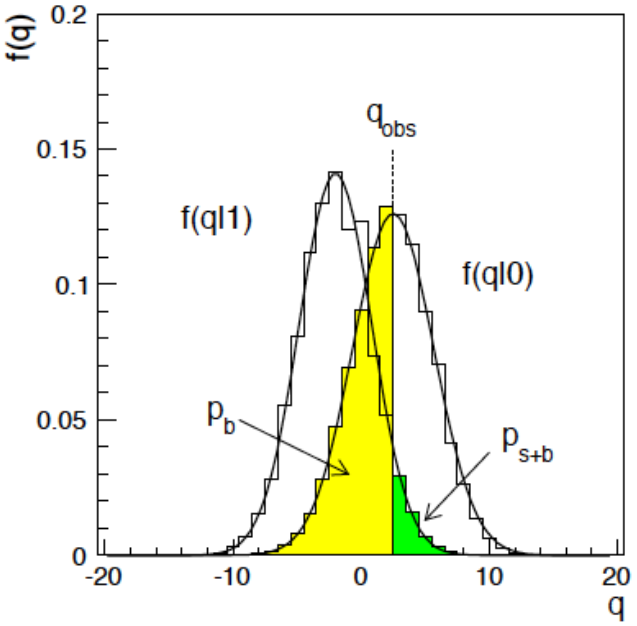

Figure G.1: Distribution of the test variable q under the $s+b$ and b hypothesis, in the plot $f(q|1)$ and $f(q|0)$ correspond to $f(q|s+b)$ and $f(q|b)$ respectively, P_b and P_{s+b} correspond to the *p-values* for the background and signal plus background models respectively.

Suppose the actual data results in a value q_{obs} of the test variable. The *p-value* of the $s+b$ hypothesis is defined as the probability under assumption

of this hypothesis, to find a value of q with equal or less compatibility with the $s+b$ model relative to what is found with q_{obs}. As the background-only distribution $f(q|b)$ is here shifted to the right, one takes the *p-value* of $s+b$ to be the probability to find q greater than or equal to q_{obs}, under assumption of the $s+b$ hypothesis, i.e.,

$$p_{s+b} = P(q \geq q_{obs}|s+b) = \int_{q_{ob}}^{\infty} f(q|s+b)dq \tag{G.1}$$

In a similar way , one takes the *p-value* of the background-only hypothesis to be

$$p_b = P(q \leq q_{obs}|b) = \int_{-\infty}^{q_{obs}} f(q|b)dq \tag{G.2}$$

In what is called the "CL_{s+b}" method, one carries out a standard statistical test of the $s+b$ hypothesis based on its *p-value*, p_{s+b}. The signal model is regarded as excluded at a confidence level of 1-α = 95% if one finds

$$p_{s+b} \leq \alpha \tag{G.3}$$

where $\alpha = 0.05$. A confidence interval at confidence level CL=1-α for the rate of the signal process can be constructed from those values of rate s (or cross section) that are not excluded, and the upper limit s_{up} is the largest value of s not excluded. By construction the interval [0,s_{up}] will cover s with a probability of at least 95%, regardless of the value of s.

The problem with CL_{s+b} procedure is that one will exclude with probability close to α (i.e, 5%) hypothesis to which one has little or not sensitivity. This corresponds to the case where the expected number of signal events is much less than that of background. Such a scenario is illustrated in Fig. G.2, and corresponding to having the distributions of q under both the b and $s+b$ hypotheses almost overlapping with each other. If for example the expected number of signal and background events are s and b, respectively, and one has $s \ll b$, then if the observed number of events has a sufficient downward fluctuation relative to $s+b$ (which is approximately equal to b), then this value of s will be excluded. In the limits where $s \ll b$, one might want intuitively this exclusion probability to go to zero, but in fact in the CL_{s+b} procedure it approaches α =5%. Given that one carries out many test for different signal models, it is not desirable that one out of twenty searches where one has no sensitivity should results in exclusion.

To protect against excluding models to which one has little sensitivity, in the CL_s procedure a signal model is regarded as excluded if one finds.

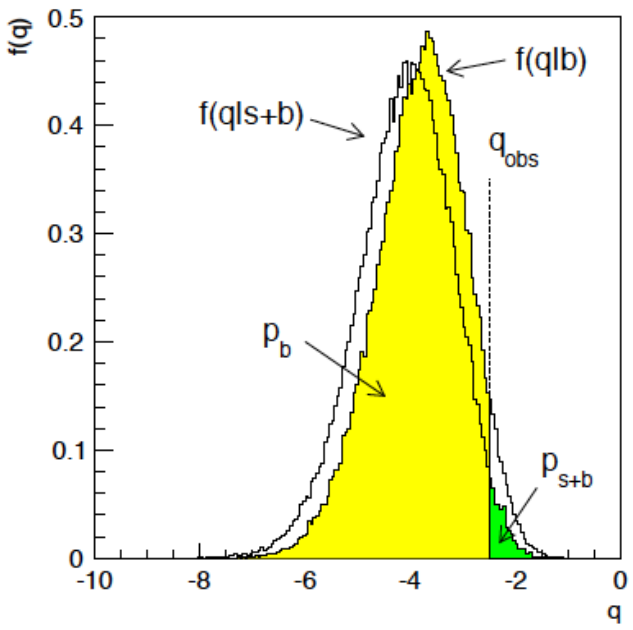

Figure G.2: Distributions of the test variable q under the $s+b$ and b hypothesis in an example where one has very little sensitivity to the signal model.

$$CL_S = \frac{p_{s+b}}{1 - p_b} \leq \alpha \tag{G.4}$$

Appendix H

ISR/FSR $t\bar{t}$ Variation and Effect on Combined $W + jets/t\bar{t}$ Estimation

$t\bar{t}$ background is the third dominant background in the analysis described in this thesis, very close in number of expected events to Z+jets, given the fact that we combine this process with W+jets as one background, it is necessary to study the uncertainties coming from using different $t\bar{t}$ MC generators (MC@NLO and AcerMC), and variation of ISF/FSR (Initial and Final state radiation) up and down in control and signal regions. Since W+jets background has a bigger contribution that $t\bar{t}$ we expect all these variations to have a relatively small impact on our final background estimation,

We start by looking at the number of $t\bar{t}$ (AcerMC) expected events in control region for the nominal sample and the different ISR/FSR samples as presented in figures H for electron and muon channel, looking at the numbers in table H.1 we can see the maximum change is around 10%, while in the signal region the changes are a bit higher (lower statistics as well) looking at the numbers in table H.2

At the end all these variations in $t\bar{t}$ are reflected as a systematic uncertainty in the final W+jets/$t\bar{t}$ estimation, as an example in tables H.3 and H.4 are presented the W+jets/$t\bar{t}$ scale factors, expected events in signal region and final estimation using nominal AcerMC $t\bar{t}$ and comparing with the different ISR/FSR samples, it is shown as well the uncertainty on the estimation by comparing predictions using different $t\bar{t}$ MC generators MC@NLO (nominal) and AcerMC, as an example we just show the values for $\sum p_T > 700$ GeV cut, the uncertainties for the rest of the signal region scenarios are reported in tables 8.28 and 8.29.

Table H.1: Number of $t\bar{t}$ events in W+jets/$t\bar{t}$ control region normalized to 1 fb^{-1}

Channel	nominal	ISRD	ISRU	FSRD	FSRU
Elec	1006.68 ± 9.3	923.628 ± 8.9	1061.54± 9.6	1045.57 ± 9.5	973.635 ± 9.1
Muons	721.378 ± 7.9	641.034 ± 7.4	716.804 ± 7.8	773.749 ± 8.2	668.179 ± 7.6
Elec	1006.68 ± 9.3	-8.2%	5.4%	3.9%	-3.2%
Muons	721.378 ± 7.9	-11.1%	-0.6%	7.2%	-7.4%

Table H.2: Number of $t\bar{t}$ events in signal region $\sum p_T > 700$ GeV normalized to 1 fb^{-1}

Channel	nominal	ISRD	ISRU	FSRD	FSRU
Elec	152.4 ± 3.6	110.4 ± 3.1	164.3 ± 3.8	161.9± 3.7	135.1 ± 3.4
Muons	88.0 ± 2.8	62.4 ± 2.3	96.7 ± 2.9	99.6 ± 2.9	75.5 ± 2.5
Elec	1006.68 ± 9.3	-27.3%	7.8%	6.2%	-11.3%
Muons	721.378 ± 7.9	-29.1%	9.9%	13.2%	-14.2%

Table H.3: Uncertainty on W+jets/$t\bar{t}$ background estimation due to ISR/FSR variations and different MC samples used for $t\bar{t}$ using $\sum p_T > 700$ GeV (electron channel)

variation	SF (W+jets/$t\bar{t}$)	SR (W+jets/$t\bar{t}$)	Estimation
nominal	0.91 ± 0.018	425.74 ± 7.03	386.1 ± 9.9
ISR down	0.93 ± 0.018	383.72 ± 6.75	356.8 ± 9.3
ISR up	0.89 ± 0.017	437.64 ± 7.11	389.4 ± 9.8
FSR down	0.90 ± 0.017	435.23 ± 7.09	389.9 ± 9.7
FSR up	0.92 ± 0.018	408.45 ± 6.92	375.7 ± 9.7
max. uncert (ISR/FSR)			7.8%
Gen. uncert(MC@NLO vs AcerMC)			4.0%

Table H.4: Uncertainty on W+jets/$t\bar{t}$ background estimation due to ISR/FSR variations and different MC samples used for $t\bar{t}$ using $\sum p_T > 700$ GeV (muon channel)

variation	SF (W+jets/$t\bar{t}$)	SR (W+jets/$t\bar{t}$)	Estimation
nominal	1.02 ± 0.023	250.51 ± 5.23	255.5 ± 7.8
ISR down	1.07 ± 0.024	224.92 ± 5.02	240.7 ± 7.6
ISR up	1.03 ± 0.023	259.24 ± 5.32	267.0 ± 8.1
FSR down	1.00 ± 0.023	262.11 ± 5.35	262.1 ± 8.1
FSR up	1.05 ± 0.024	238.02 ± 5.14	249.9 ± 7.9
max. uncert			5.8 %
Gen. uncert (MC@NLO vs AcerMC)			8.4 %

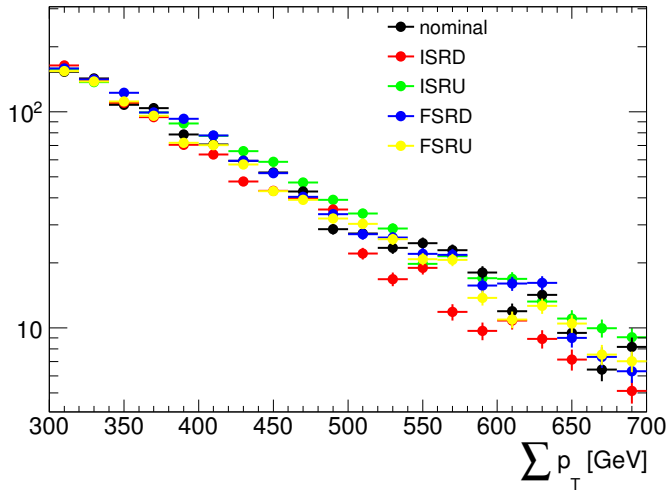

(a) $\sum p_T$ in control region electron channel

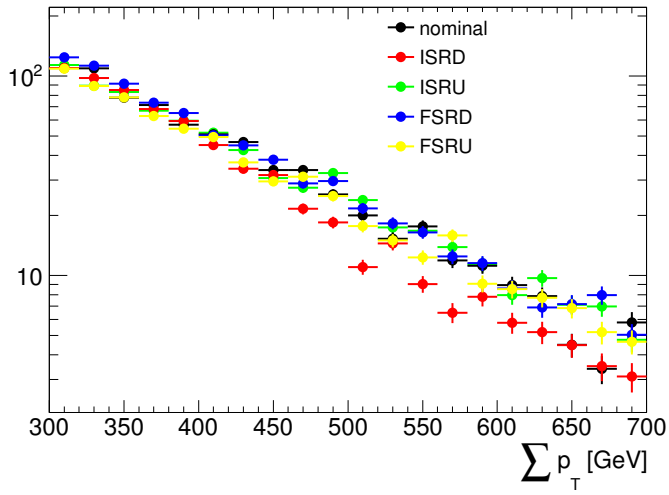

(b) $\sum p_T$ in control region muon channel

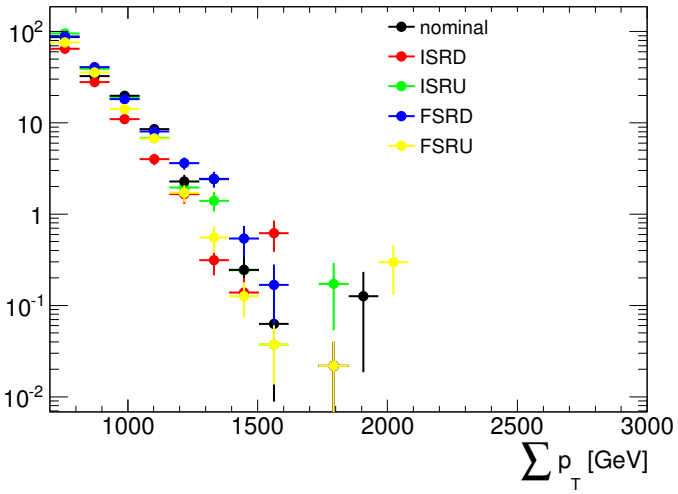

(c) $\sum p_T$ in signal region electron channel

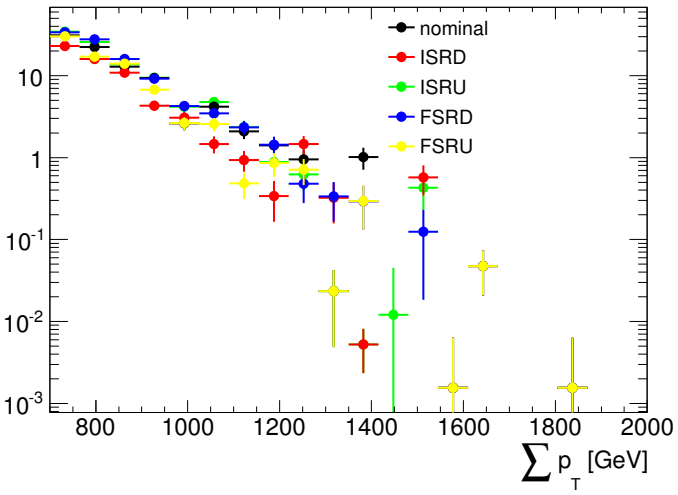

(d) $\sum p_T$ in signal region muon channel

Appendix I

Individual PDF Uncertainties for W+jets/$t\bar{t}$ Estimate

To calculate the uncertainty due to the choice of PDF, the samples are re-weighted and the effect in the control and signal regions evaluated. The relevant uncertainty is the change in the signal region prediction after normalization in the control region.

Two or three values are determined: the fractional change moving between the default PDF `CTEQ6L1` and `CTEQ6.6` (where applicable), and the difference between the upper and lower error-set of `CTEQ6.6` with respect to the nominal value.

The final uncertainty used in the analysis and given in Section 8.3 is the larger of the two `CTEQ6.6` error set effects, for the combined W+jets and $t\bar{t}$ estimate.

Tables I.1 and I.2 show the individual sample uncertainties for the muon channel, with their electron channel equivalents given in Table I.3 and I.4.

Signal Region	`CTEQ6.6`	`CTEQ6.6`: Up	`CTEQ6.6`: Low
$\sum p_T > 700$ GeV	-0.055	0.051	-0.041
$\sum p_T > 800$ GeV	-0.064	0.061	-0.049
$\sum p_T > 900$ GeV	-0.072	0.074	-0.059
$\sum p_T > 1000$ GeV	-0.072	0.091	-0.073
$\sum p_T > 1200$ GeV	-0.103	0.110	-0.094
$\sum p_T > 1500$ GeV	-0.210	0.175	-0.178

Table I.1: Fractional change in expected W+jets background in the SR after CR normalization, for several PDF choices: `CTEQ6.6` relative to nominal `CTEQ6L1` `CTEQ6.6` with upper error set uncertainties, and `CTEQ6.6` with lower error set uncertainties (relative to `CTEQ6.6` central value). These are for the muon channel.

Signal Region	CTEQ6.6: Up	CTEQ6.6: Low
$\sum p_T > 700$ GeV	0.074	0.0828
$\sum p_T > 800$ GeV	0.100	0.121
$\sum p_T > 900$ GeV	0.179	0.233
$\sum p_T > 1000$ GeV	*no stat.*	*no stat.*
$\sum p_T > 1200$ GeV	*no stat.*	*no stat.*
$\sum p_T > 1500$ GeV	*no stat.*	*no stat.*

Table I.2: Fractional change in expected $t\bar{t}$ background in the SR after CR normalization, for CTEQ6.6 with upper error set uncertainties, and CTEQ6.6 with lower error set uncertainties (relative to CTEQ6.6 central value). These are for the muon channel.

Signal Region	CTEQ6.6	CTEQ6.6: Up	CTEQ6.6: Low
$\sum p_T > 700$ GeV	-0.043	0.061	-0.046
$\sum p_T > 800$ GeV	-0.059	0.061	-0.047
$\sum p_T > 900$ GeV	-0.064	0.069	-0.055
$\sum p_T > 1000$ GeV	-0.068	0.096	-0.075
$\sum p_T > 1200$ GeV	-0.068	0.130	-0.100
$\sum p_T > 1500$ GeV	0.0035	0.269	-0.204

Table I.3: Fractional change in expected W+jets background in the SR after CR normalization, for several PDF choices: CTEQ6.6 relative to nominal CTEQ6L1, CTEQ6.6 with upper error set uncertainties, and CTEQ6.6 with lower error set uncertainties (relative to CTEQ6.6 central value). These are for the electron channel.

Signal Region	CTEQ6.6: Up	CTEQ6.6: Low
$\sum p_T > 700$ GeV	0.123	0.102
$\sum p_T > 800$ GeV	0.114	0.101
$\sum p_T > 900$ GeV	0.143	0.128
$\sum p_T > 1000$ GeV	0.155	0.144
$\sum p_T > 1200$ GeV	0.189	0.221
$\sum p_T > 1500$ GeV	0.103	0.119

Table I.4: Fractional change in expected $t\bar{t}$ background in the SR after CR normalization, for CTEQ6.6 with upper error set uncertainties, and CTEQ6.6 with lower error set uncertainties (relative to CTEQ6.6 central value). These are for the muon channel.

Appendix J

Black Hole candidate event

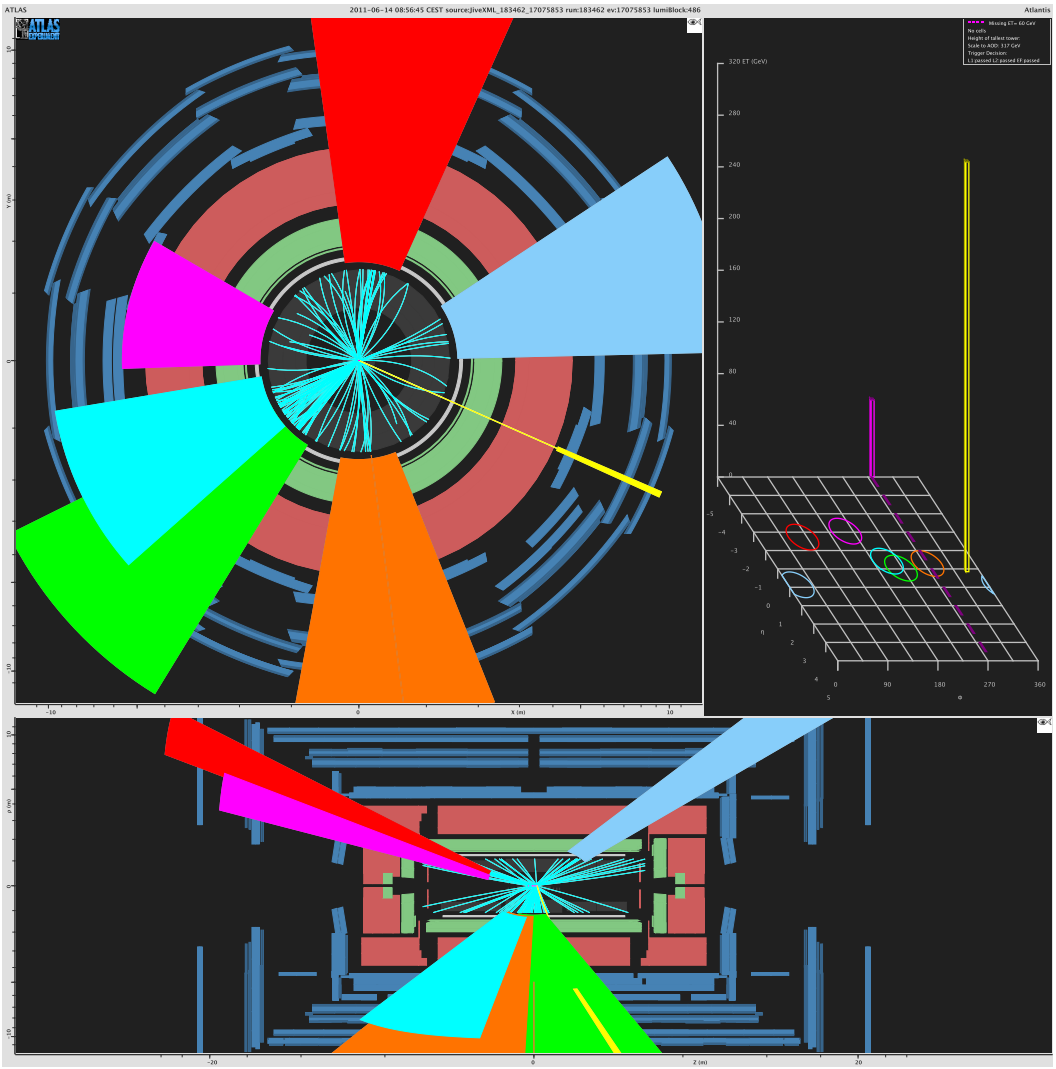

Figure J.1: One of the highest-p_T event in our selection it is located in the signal region and it is a genuine black hole candidate event, it contains one isolated high-p_T muon and 4 hard jets (p_T >100 GeV), all the objects make a $\sum p_T$ ~1.6 TeV, in the figure the jets are represented by the cones of different colors, the muon is the yellow line and the E_T^{miss} representation is the purple line

Appendix K

Distributions with $\sum p_T > 700$ GeV After Normalization from Control Regions

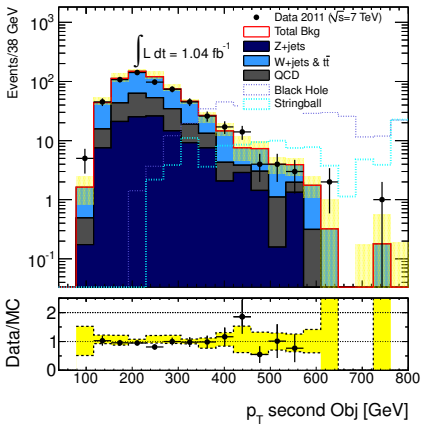

(a) Transverse momentum of second leading object in electron events.

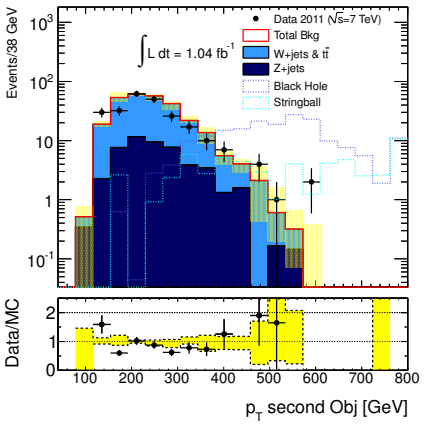

(b) Transverse momentum of second leading object in muon events.

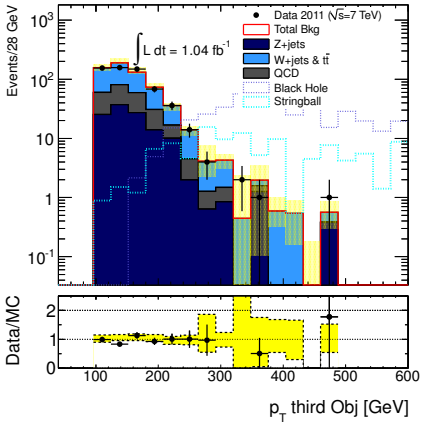

(c) Transverse momentum of third leading object in electron events.

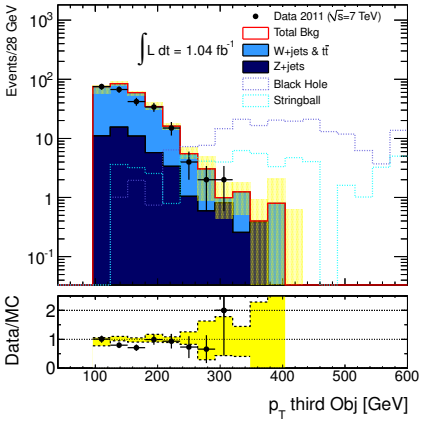

(d) Transverse momentum of third leading object in muon events.

Figure K.1: Transverse momentum of three most leading objects after preselection. The Monte Carlo samples are normalized by their cross-section to 1.04 fb^{-1}.

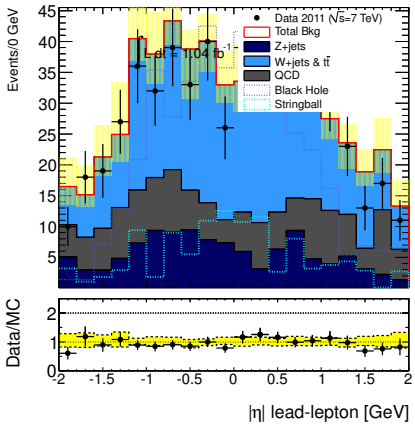

(a) Pseudorapidity distribution of the leading lepton in electron events.

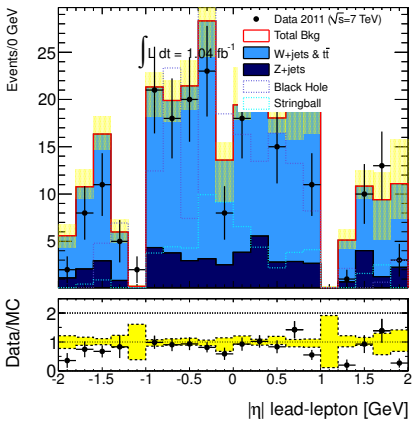

(b) Pseudorapidity distribution of the leading lepton in muon events.

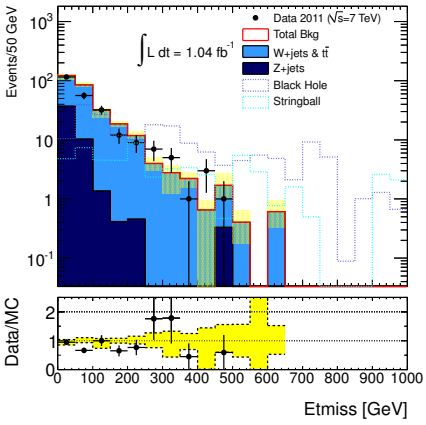

(c) Missing energy distribution in muon events.

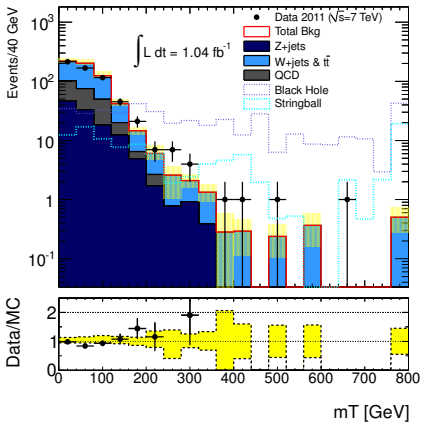

(d) Transverse mass distribution of the leading lepton in electron events.

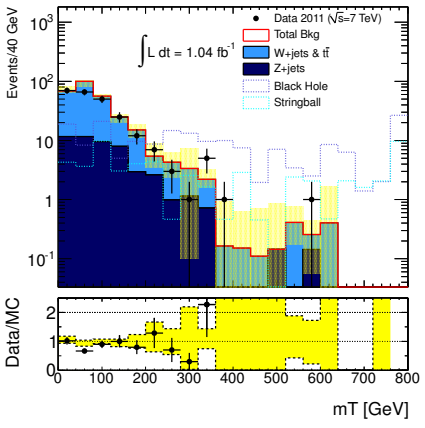

(e) Transverse mass distribution of the leading lepton in muon events.

Figure K.2: Lepton η, E_T^{miss} and m_T distributions for events in signal region, defined by a $\sum p_T > 700$ GeV requirement.

Appendix L

Comparison between Lepton plus Jets and Same-sign di-muon Black Hole analysis

In parallel to the lepton plus jets analysis described in this thesis, another analysis was developed and recently published in the ATLAS collaboration, such analysis was looking as well for Black Hole and String Ball production but in a final state with two same-sign muons, one of the advantages of such analysis is that the SM background is very small (very few SM processes produce two same-sign muons), the disadvantage is that the statistics would be smaller compared to the Lepton plus jets search and therefore the energy reach will be weaker. In the case of the di-muon analysis the main discriminant variable was the number of tracks in events with two same-sign muons as presented in Fig. L.1, as expected the particle multiplicity in Black hole decay will be higher than SM processes.

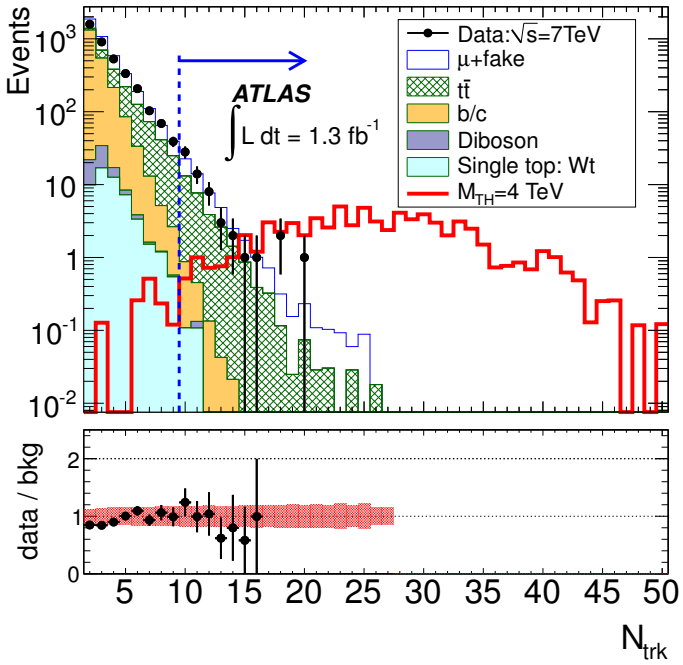

Figure L.1: The track multiplicity distribution for same-sign di-muon events. The region with Ntrk>9 is selected as the signal region. The background histograms are stacked. The signal expectation for a non-rotating Black Hole model with parameters M_D = 800 GeV, M_{TH}=4 TeV, and six extra dimensions is overlaid for illustrative purposes. The bottom panels shows the ratio of data to the expected background (points) and the total systematic uncertainty on the background (shaded area).

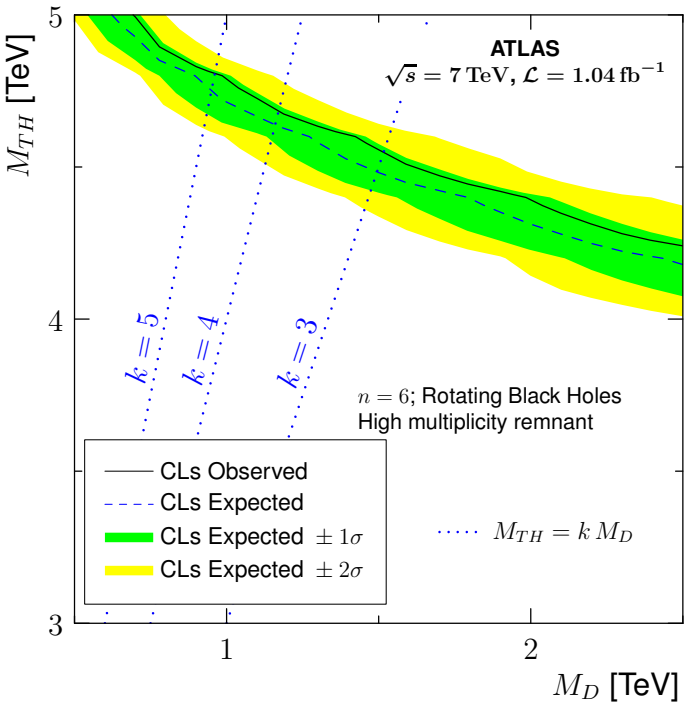

(a) Rotating Black Holes in the Lepton plus Jets analysis

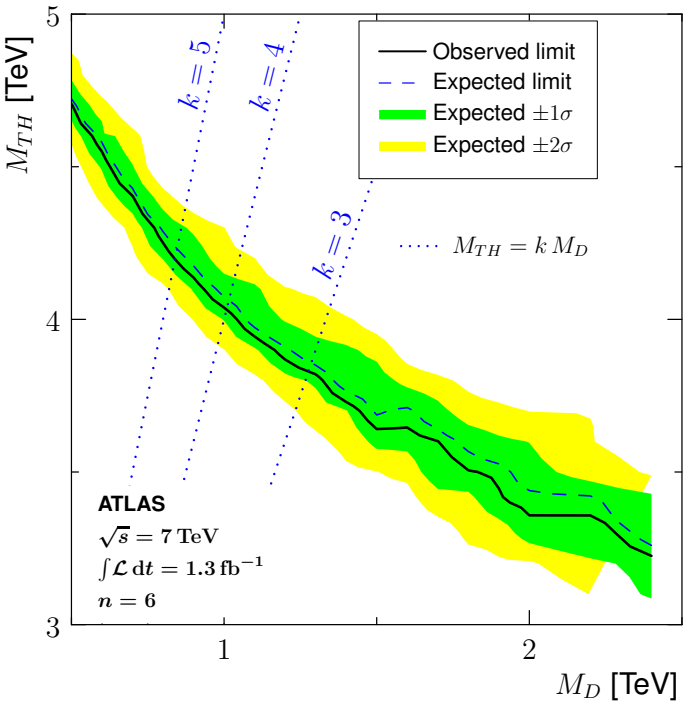

(b) Rotating Black Holes in the Same-sign di-muon analysis

Figure L.2: 95% C.L. limit in the M_{TH}-M_D plane, for a rotating Black Hole model with six extra dimensions. The solid (dashed) line shows the observed (expected) limits, with the green and yellow bands the expected 1σ and 2σ variations of the expected limits. The dotted blue lines show lines of constant $k = M_{TH}/M_D$. The plot on the top refers to the Lepton plus Jets analysis and the plot on the bottom to the Same-sign di-muon one, clearly the exclusion power is bigger for the Lepton plus Jets one

Appendix M

Glossary

- **Schwarzschild radius**: (also known as the gravitational radius) It is defined as the radius from the center of an object such that all the mass of that object is compressed within that sphere and for a particle to escape from that surface it must travel with the speed of light. The object which real size correspond to the Schwarzchild radius is precisely a Black Hole.
- **TeV**: is a unit of energy used in particle physics (10^{12} eV). 1 TeV is about the energy of motion of a flying mosquito. What makes the LHC so extraordinary is that it squeezes that energy into a space of about a million million times smaller than a mosquito.
- **Event**: What occurs when two particles collide or a single particle decay.
- **Jet**: Depending on their energy, the quarks and gluons emerging from a collision will materialize into 5-30 particles (mostly mesons and baryons). At high momentum, these particles will appear in clusters called "jets", these jets are group of particles moving in roughly the same direction centered about the original quark and gluon.
- **Track**: The record of the path of a particle traversing the detector.
- **Luminosity**: The number of particles per square-centimeter per second generated in the beams of high energy particle experiments. The higher the luminosity, the greater the number of events produced for study.
- E_T^{miss} : Missing energy, is the jargon used in high energy physics to refer to the energy of the neutrino which cannot be measured directly but from energy conservation is calculated indirectly
- **Cut**: A selection in particle properties like energy, number of particles, position in the space, etc. In order to reduce the rate of events to analyze and usually motivated by the kind of signal the analyzer is looking for.
- η: In experimental particle physics pseudo-rapidity (η), is a commonly used spatial coordinate describing the angle of a particle relative to the beam axis. It is defined as

$$\eta = -ln\left[tan\left(\frac{\theta}{2}\right)\right] \tag{M.1}$$

In hadron collider physics, the rapidity (or pseudo-rapidity) is prefered over the polar angle θ because, loosely speaking, particle production is constant as a function of rapidity. The relation of θ and η can be seen in figure M.1

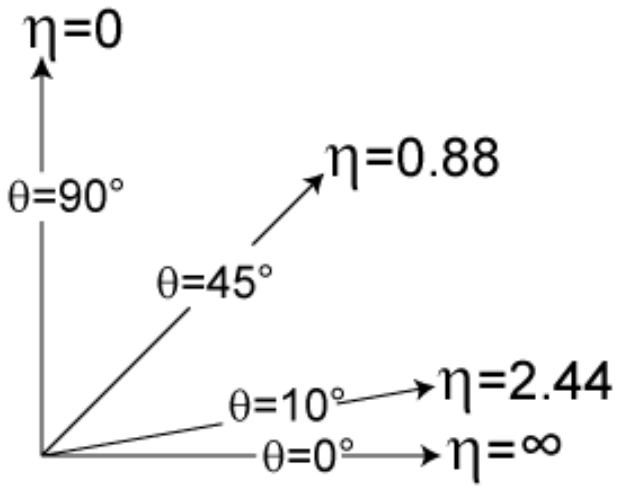

Figure M.1: As angle increases from zero, pseudo-rapidity decreases from infinity. In particle physics an angle of zero is usually along the beam axis.

- ϕ: Is the azimuthal angle located on the same plane than the beam trajectory.

Bibliography

[1] N. Mistry, *"A brief introduction to particle physics,"* Cornell University, (Cited on page 1.)

[2] M. Gell-Mann, *"A schematic model of baryons and Mesons"*, Phys. Lett., Vol 8, number 3, (1964) 214-215 (Cited on page 2.)

[3] J.Chiaverini, S.J. Smullin, et al. *"New experimental constrains on non-Newtonian forces below 100μm*, Phys.Rev.Lett. 90, 151101 (2003) (Cited on page 6.)

[4] N. Arkani-Hamed, S. Dimopolous, and G. Dvale, *The Hierarchy Problem and New Dimensions at a Millimeter*, Phys. Lett B. 429, 263 (1998) (Cited on page 6.)

[5] Ramesh Narayan, *"Evidence for the Black Hole Horizon"*, arXiv:astro-ph/0310692v1, 2003 (Cited on page 8.)

[6] D. Gingrich, K. Martell *"Study of highly excited string states at the Large Hadron Collider"* Phys.Rev.D, Vol 78, 115009 (2008) (Cited on page 10.)

[7] LEP Exotica Working Group, the ALEPH, DELPHI, L3 and OPAL Collaborations, CERN Note LEP Exotica WG 2004-03 (2004) (Cited on page 10.)

[8] CDF Collaboration, Phys. Rev. Lett. 101 (2008) 181602 (Cited on page 10.)

[9] ATLAS Collaboration, Phys. Lett. B 705 (2011) 294-312 (Cited on page 10.)

[10] CMS Collaboration, Phys. Rev. Lett. 107 (2011) 201804 (Cited on page 10.)

[11] S. Dimopolous, G. Landsberg, *"Black Holes at the LHC"*, Phys. Rev. Lett. Vol. 87 (2011) (Cited on pages 10, 12, 13 and 14.)

[12] The ATLAS Collaboration, ATLAS-CONF-2010-088, `http://cdsweb.cern.ch/record/1299103/` (2010). (Cited on page 15.)

[13] The CMS Collaboration, CMS-PAS-EXO-11-071, `http://cdsweb.cern.ch/record/1369209/` (2011). (Cited on page 15.)

[14] The ATLAS Collaboration, ATLAS-CONF-2011-068, http://cdsweb.cern.ch/record/1349309/ (2011). (Cited on page 15.)

[15] The ATLAS Collaboration, arXiv:1111.0080 (2011) [hep-ex], (Cited on page 15.)

[16] The ATLAS Collaboration, New J. Phys. 13 (2011) 053044. (Cited on page 15.)

[17] *"LHC White Book"*, CERN/AC/93-03 LHC Conceptual Design Report, CERN/AC-95-05 (Cited on page 17.)

[18] *"LHC Design Report"*, Vol. 1, "The LHC MAIN RING", pag. 21 CERN-2004-03, CERN LIBRARIES, GENEVA (Cited on page 18.)

[19] *"Construction and Performance Plans for the LEP Collider"*, W. Schnell 1981 Phys. Scr. 23 339 (Cited on page 17.)

[20] The ATLAS Technical Proposal, CERN/LHCC/94-93 (1994) (Cited on page 19.)

[21] *"ATLAS Detector and Physics Performance"* Technical Design Report, Volume 1, 25 May, 1999 ATLAS Collaboration (Cited on page 23.)

[22] ATLAS Collaboration, ATLAS-CONF-2011-116, http:/cdsweb.cern.ch/record/1376384/ (2011). (Cited on page 25.)

[23] ATLAS Collaboration. arXiv:1110.3174 (2011) [hep-ex], submitted to Eur. Phys. J.C. (Cited on page 25.)

[24] ATLAS Collaboration, ATLAS-CONF-2010-095 (2010), http://cdsweb.cern.ch/record/1299573/ (2010). (Cited on page 25.)

[25] *"Electron energy scale in-situ calibration and performance"* ATLAS NOTE,ATL-COM-PHYS-2011-263 (Cited on page 28.)

[26] *"ATLAS Muon Momentum Resolution in the First Pass Reconstruction of the 2010 p-p Collision Data at* $\sqrt{s}$*=7 TeV"* ATLAS NOTE, ATLAS-CONF-2011-046 (Cited on page 32.)

[27] ATLAS collaboration, Phys. Lett. B 705 (2011) 28-46. (Cited on page 35.)

[28] *"The anti-kt jet clustering algorithm"*, JHEP04 (2008) 063 (Cited on page 35.)

[29] *"Jet energy measurements with the ATLAS detector in proton-proton collisions at* $\sqrt{s}$*=7 TeV"*, Europ Phys. Journal (Cited on page 36.)

[30] *"Missing Et Performance in ATLAS"*, arXiv:0810.0181, ATLAS-PHYS-PROC-2008-023 (Cited on page 38.)

[31] T.Sjostrand, S.Mrenna, and P.Z. Skands, JHEP 05 (2006) 026. (Cited on page 41.)

[32] S.Frixione and B.R. Webber, JHEP 06 (2002) 029 (Cited on page 42.)

[33] M.L. Mangano, M. Moretti, F. Piccinini, R. Pittau, and A.D. Polosa, JHEP 07 (2003) 001. (Cited on page 41.)

[34] T. Gleisberg et al., JHEP 02 (2004) 056. (Cited on page 42.)

[35] G. Corsella et al., JHEP 0101 (2001) 010. (Cited on page 41.)

[36] J.Butterworth, J. Forshaw, and M. Seymour, Z.Phys. C72 (1996) 637-646 (Cited on page 41.)

[37] J.A. Frost et al., JHEP 10 (2009) 014. (Cited on page 43.)

[38] D.-C. Dai, G. Starkman, D. Stojkovic, C. Issever, E. Rivzi, and J. Tseng, Phys. Rev. D 77 (2008) 076007 (Cited on page 44.)

[39] Yu.A. Golfand, E.P. Likhtmanm, JETP Lett. 13 (1971) 323 (Cited on page 89.)

[40] ATLAS Collaboration, "Searches for supersymmetry with the ATLAS detector using final states with two leptons and missing transverse momentum in $\sqrt{s} = 7$ TeV proton-proton collisions", PLB 709 (2012) 137-157 (Cited on pages 92 and 106.)

[41] C. Amsler et al. (Particle Data Group), Physics Letters B667, 1 (2008) and 2009 partial update for the 2010 edition (Cited on page 133.)